UNIVERSITY OF CALIFORNIA
RIVERSIDE

Design and Synthesis of RNA Nanostructures

A Dissertation submitted in partial satisfaction
of the requirements for the degree of

Doctor of Philosophy

in

Bioengineering

by

Jaimie Marie Stewart

June 2018

Dissertation Committee:

Dr. Elisa Franco, Chairperson
Dr. B. Hyle Park
Dr. Valentine I. Vullev

The Dissertation of Jaimie Marie Stewart is approved:

Committee Chairperson

University of California, Riverside

Acknowledgments

The culmination of the work presented in this thesis would not have been possible without the support of many people.

Foremost, I would like to thank my advisor and thesis chairperson, Professor Elisa Franco. I am immensely grateful for her invaluable expertise and guidance over my Ph.D. study. Under her guidance and mentorship I have learned so much and have become a refined scientist and engineer. She has allowed me the freedom to explore different research areas and has provided me with countless opportunities to collaborate on research projects and present my research both nationally and internationally. Professor Franco has been a phenomenal advisor and mentor. Besides my advisor, I would also like to thank the rest of my thesis committee: Professor Valentine I. Vullev and Professor B. Hyle Park for their encouragement and insightful comments to help me think critically about my research pursuits.

Special thanks to Professor Kirill A. Afonin for our collaborative work as well as Professor Ebbe Sloth Andersen and Dr. Guido Grossi for hosting me as a visiting researcher at Aarhus University.

Thanks to all the members of the Dynamic Nucleic Acid Systems laboratory. I am very grateful and thankful to Dr. Hari Subramanian for teaching me many of the research techniques I used for the completion of this thesis, for his encouragement, and inspiring discussions. I would also like to thank Dr. Leopold Green, Jr. and Dr. Christian Cuba for stimulating conversations on various research endeavors and entrepreneurial pursuits. Additionally, I would like to thank Claire Tran, Siddharth Aggarwal, and Melissa Klocke

for support.

Thank you to Toi Thibodeaux and Megan Rush for the immense support and encouragement.

Last, but not least, I am deeply thankful to my family, in particular my mother Sheila Brown and Adam Muransky for their encouragement, love, and support.

In loving memory of my grandmother, Marjorie Marie Holliman.

ABSTRACT OF THE DISSERTATION

Design and Synthesis of RNA Nanostructures

by

Jaimie Marie Stewart

Doctor of Philosophy, Graduate Program in Bioengineering
University of California, Riverside, June 2018
Dr. Elisa Franco, Chairperson

Nucleic acid nanotechnology proposes many approaches to construct self-assembled structures using RNA and DNA. These structures have several applications such as scaffolding, sensing, and drug delivery. Although RNA and DNA are similar molecules, they also have unique chemical and structural properties that must be considered when using these molecules to assembly structures. RNA is a natural multifunctional polymer, and has an essential role in complex pathways and structures within the cellular environment. Due to its rich and diverse biological functions, synthetic self-assembling RNA nanostructures are emerging as a powerful tool with potential applications in drug delivery and intracellular control.

Here we demonstrate the formation of RNA nanostructures of varying size, complexity, and biological functionality using methods adapted from DNA nanotechnology. To achieve this goal we imported established approaches in the field of DNA nanostructure and DNA circuit design and optimized assembly protocols to ensure high yield of assembly. We employed design principles and experimental methods to obtain synthetic programmable

RNA structures with biological functionality through two primary objectives: (1) Design and characterization of RNA tiles that assemble into RNA nanostructures with predictable features and (2) The usefulness of our RNA assemblies in a biomedical application, in particular functionalization with RNA molecules such as small interfering RNA (siRNA) for targeted RNA interference to inhibit gene expression. Our results show that scalable RNA self-assembled structures can be obtained using purely with Watson-Crick interactions, without relying on conserved tertiary structure motifs typically used to build RNA structures. Lastly, results show that functionalization does not prevent nanostructure assembly and these structures are capable of silencing genes.

Contribution

Chapter 1: Adapted from Stewart and Franco [114]. Jaimie Marie Stewart performed the literature search and writing. Elisa Franco advised in terms of literature to include and organization.

Chapter 2: Adapted from Stewart et al. [115]. Elisa Franco developed the initial project idea and advised on experiments and results. Jaimie Marie Stewart designed tiles, performed RNA extractions, gel electrophoresis, AFM imaging, and data analysis. Hari K.K. Subramanian discussed the results and advised on experiments.

Chapter 3: Adapted from Stewart et al. [116]. Kirill A. Afonin developed the initial project idea and advised on experiments. Jaimie Marie Stewart designed tiles, performed RNA extractions, gel electrophoresis experiments, AFM imaging, and tile and lattice purification. Elisa Franco advised on experiments and results. Hari K.K. Subramanian discussed the results and advised on experiments. Brandon K. Roark performed dynamic light scattering experiments, UV-melting experiments, and human blood serum stability assays. Mathias Viard performed transfection experiments, flow cytometery, confocal microcopy, gene silencing experiments, and viability assays.

Chapter 4: Jaimie Marie Stewart designed tiles, performed RNA extractions, gel electrophoresis experiments, AFM imaging, and data analysis. Elisa Franco advised on experiments and results.

Support

My graduate studies at the University of Califoronia, Riverside was supported by the Dean's Distinguished Fellowship, U.S. National Science Foundation through CAREER grant BMAT 1450747, and the Ernest Propes Endowed Graduate Fellowship.

Contents

List of Figures

List of Tables

Chapter 1

Introduction

1.1 Nanotechnology and nanostructured materials

Nanotechnology incorporates engineering materials on the atomic and molecular scale. The precise definition of nanotechnology describes structures that are 1-100 nm in size [57], however modern interpretation includes structures that are several hundred nanometers in size. The concept of nanotechnology began with the talk "There is Plenty of Room at the Bottom" by Richard Feynman. In his talk Feynman explained methods that may be used by scientists to direct and regulate single atoms and molecules.

Nanotechnology is an interdisciplinary field spanning across physics, chemistry, biology, material science, and engineering. The primary goal of nanotechnology in the area of materials science is to be able to observe and manipulate matter at the nanometer scale to specify and exploit its properties for desired applications.

Nanomaterials can organize into structures by either self-assembly or externally directed assembly. Self-assembly is the disarranged materials assembly into a target organized

structure by way of particular, in-system interactions among the constituents themselves, without external guidance. Externally directed self-assembly is driven by an external factor instead of by in-system interactions.

1.2 Nucleic Acid Nanotechnology

The field of nucleic acid nanotechnology has produced a wealth of self-assembly methods to build nano and micron-sized structures [139, 42]. These biomolecular structures are useful in various applications, in particular they can be used as scaffolds or templates for growth of other materials, and as drug delivery vectors. Both RNA and DNA have been successfully used to build scaffolds with rationally programmable features. RNA structures up to a few hundreds of nanometers large have been demonstrated to assemble *in vitro* as well as *in vivo* [42, 23]. DNA has however been the polymer of choice to demonstrate 2D and 3D self-assembled structures with size ranging from 20 nm to several microns, due to its stability and the predictability of Watson-Crick base pair interactions [127, 98, 27].

Although RNA and DNA share many general features, they also present many unique chemical and structural properties; Fig. 1.1 summarizes some of the structural characteristics of DNA and RNA. These differences have prompted the development of distinct approaches to programmed self-assembly. Specifically, *in silico* sequence design to satisfy domain complementarity requirements combined with Holliday junction motifs dominates the field of DNA self-assembly [139]. In contrast, the exploitation of conserved, naturally evolved motifs with predictable tertiary structure (such as kissing loops) dominates RNA self-assembly methods [6].

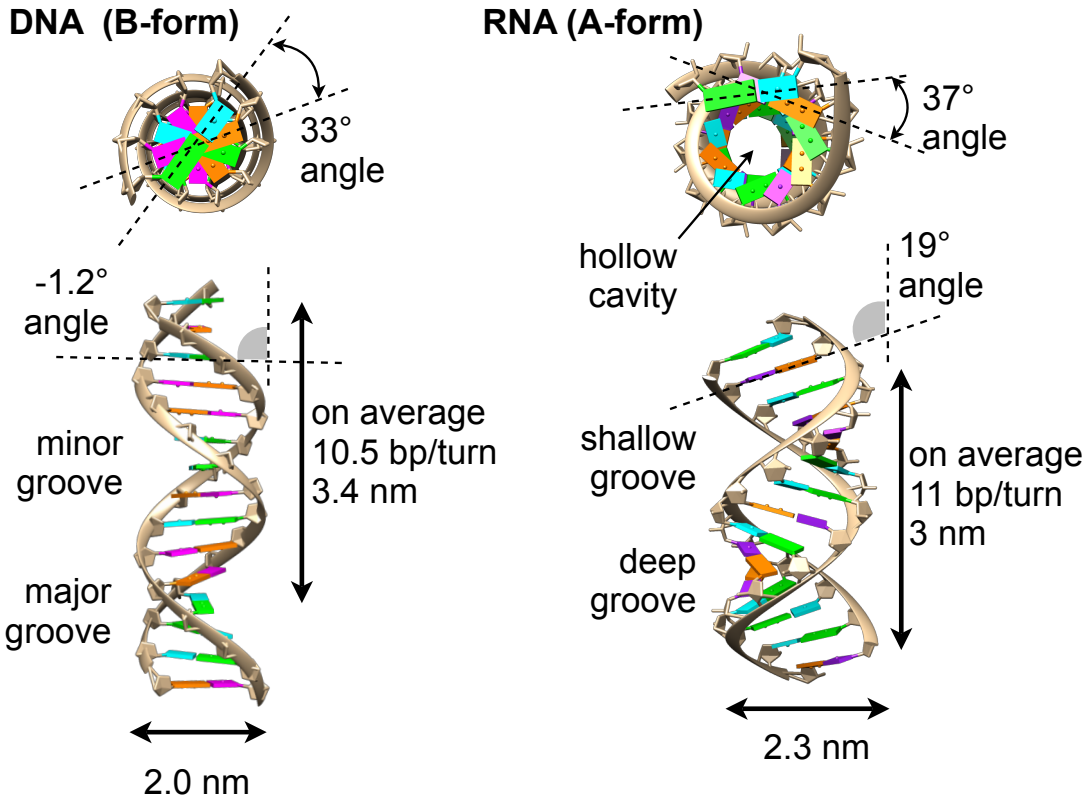

Figure 1.1: **Comparison between DNA and RNA double helices.** Image generated using Chimera [93].

This brief review provides a comparison of existing approaches to the design of large, multi-component RNA and DNA nanostructures. For the reader convenience, an abridged list of design methods and protocols is reported in Tables 1.1 and 1.2. We focus in particular on the problem of building large, multi-stranded RNA scaffolds with the potential of being stable or assembling *in vivo*. The construction of large RNA nanostructures presents significant challenges relative to small RNA nanoparticles [42], because of the higher likelihood of RNA strands to become trapped into undesired secondary structures. We suggest that methods developed for DNA tile systems may be viable to build large RNA assemblies which could be expressed and assemble *in vivo*; we highlight advantages, limitations, and challenges of this strategy.

1.3 DNA nanotechnology relies on *in silico* design of strands with minimal secondary structure

The early objective of DNA nanotechnology aimed to form robust three-dimensional crystals to address the "crystallization problem" [104]. Since then, several other breakthroughs have been accomplished such as the assembly of large lattices [127, 103], 2D and 3D structures [99, 98, 28], and nanomachines [112, 79, 34]. It is important to note that the scope of DNA nanotechnology goes beyond materials science and biomedical applications. Adleman's Hamiltonian Path experiment [1] demonstrated that DNA, a biological programmable molecule, could be used as a tool to solve a computational problem; Winfree's DNA tiles were designed to build algorithmic assemblies [127, 100, 13].

The design of DNA self-assembling systems generally starts with the identification of complementary domains that form double helices connected via Holliday-type junctions and achieve the desired spatial features when the participating strands bind. After domain-level interactions are specified, sequences of bases can be optimized to maximize the probability of forming the target complexes by free energy and energy strain minimization [25]. The thermodynamic parameters of Watson-Crick base pairing are well characterized [102]; the structure of the DNA double helix is also very well understood (Fig. 1.1) as well as the Holliday junction motif widely used in DNA nanotechnology [106]. Thus, sequence-specific energetics and geometry of a target DNA assembly can be easily modeled for the purpose of sequence optimization, which can be done with a variety of software toolboxes [134, 81, 105]. This two-stage design relies on the fact that virtually arbitrary sequences can be used to satisfy desired domain-level interaction constraints.

There are two main approaches to design DNA nanostructures: the tiling method and the origami method. Table 1.1 summarizes the features of these two approaches. Ned Seeman originally studied DNA tiles [37] as a model for double-strand breaks in DNA recombination processes. The primary element in the DNA tile is the crossover junction, which can be defined geometrically by determining the positions where the phosphodiester linkage crosses over from helix to helix [106]. Tile monomers consist of multiple short DNA strands (20–60 bases) assembling into two double helices rigidly connected by two junctions, which create a double crossover (DX). Various types of DX tiles were later modified to include single-stranded "sticky end" domains, and operate as monomers whose binding affinity could be specified by sticky end complementarity [127] (Fig. 8.2 A, B, C). Sticky

ends must not over or under twist the DNA double helix or negatively affect the stability of the target structure. DX tiles have been used to build two-dimensional lattices and three-dimensional tubular structures that can grow to micron-scale size. Several different tile designs have been demonstrated and characterized, ensuing in different characteristics such as rigidity, bend, and stability of tiles, and affecting the tile assembly shape [99, 31, 85]. In general, DX tile-based DNA systems function as a programmable "jigsaw" puzzle that grows in a scalable manner and can implement algorithmic assemblies; however with a finite number of tiles only simple, repeated patterns and structures (such as nanotubes, ribbons, and lattices) can be generated.

The DNA origami method addresses the limited pattern complexity that can be obtained with tiling systems. This method uses a long single-stranded DNA which folds into a target pattern with short DNA strands that, each creating a junction, act as "staples" to stabilize the structure (Fig. 8.2 D). The original method of designing DNA origami consisted of creating a structural outline and then producing staple sequences with programs that would upload the M13 bacteriophage sequence. Different software packages to automate origami design have been developed, such as Tiamat [126], SARSE [11], and caDNAno [29]. This method of assembly offers a higher degree of spatial control over self-assembly in comparison to tile-based assembly [12, 28, 24, 46] (Fig. 8.2 E, F); however, the complexity of an individual origami limits the scalability of its size relative to tile-based systems, which can grow to several microns in length.

Recent work has tried to address this limitation with the development of origami tiling or connector systems. Individual origami tiles or blocks can be interfaced in two

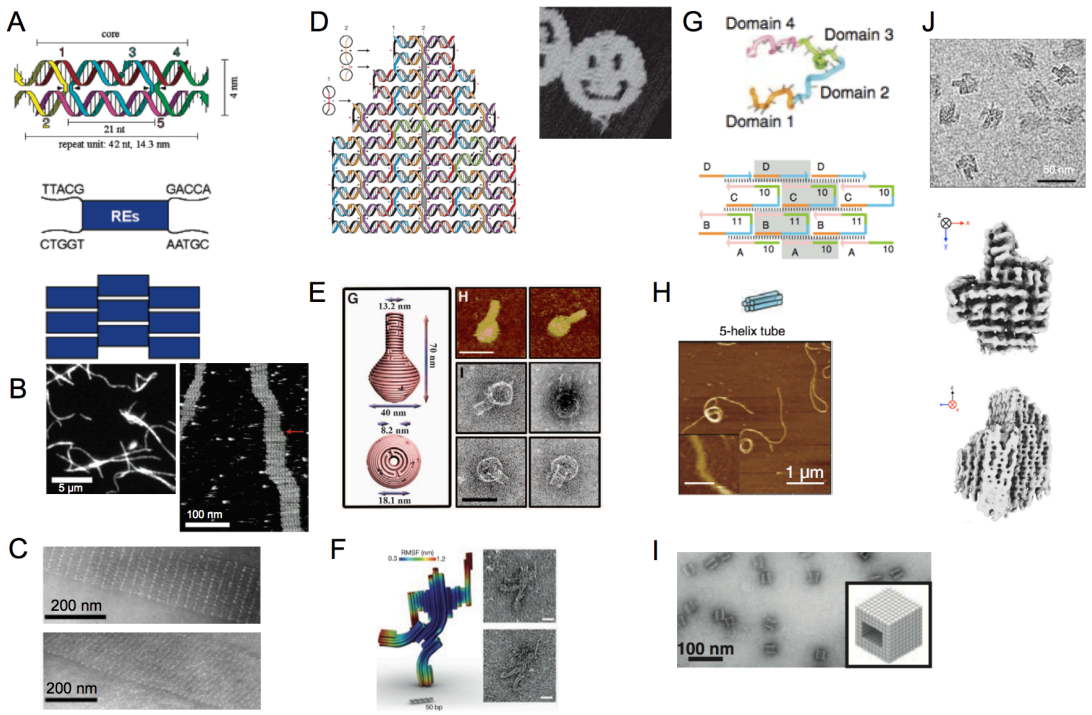

Figure 1.2: **Examples of DNA nanostructures** A: DNA DAE-E tile and lattice assembly [99]. B: AFM images of DNA nanotubes assembled from tiles shown in A [99]. C: TEM images of chiral DNA nanotubes assembled from DAE-O tiles [85]. D: Schematic of DNA origami folding and AFM image of DNA origami smiley face [98]. E: Schematic of DNA origami nanoflask and, AFM and TEM images of nanoflask [46]. F: Schematic of multilayered DNA origami and TEM image of multilayered DNA origami [20]. G: Four domain SST motif that assembles into DNA lattices [130]. H: AFM image of SST DNA nanotubes assembled [130]. I: TEM of DNA crystals assembled from single-stranded DNA bricks [60]

ways: the first approach is the use of sticky ends [77, 140, 53], where binding patterns are assigned by Watson-Crick base pairing. The main disadvantages of this approach are the high yield of imperfect structures and the required long annealing process; the method is also sensitive to the annealing parameters (high temperatures yield defective tiles that cannot interact, and low temperatures result in formation of crystal nuclei and aggregation). The second approach is to use stacking interactions between blunt ends at the edges of individual origami [128]. Stacking interactions have been particularly useful to generate dynamically reconfigurable bonds in 3D origami [40] (Fig. 8.2 F). The main challenge of this approach is that poor models make it difficult to energetically distinguish correct and incorrect bonds [128].

The complexity achievable by DNA tile systems has been recently expanded by single-stranded tiles (SST) [130]. Each SST interacts with other tiles via four distinct domains generating a single crossover junction (Fig. 8.2 H). This motif can be used to build large, programmable, and scalable ribbons and lattices [130] (Fig. 8.2 J), but also 2D and 3D shapes [125, 59, 60] with complexity comparable to that of DNA origami (Fig. 8.2K). Here, short unique strands each having a role akin to that of a pixel or a voxel, yield objects with sizes ranging in the order of few hundreds of nanometers. This approach does not require a long DNA scaffold, which can present a significant design constraint and pose re-design challenges. However, the size versus complexity tradeoff is not yet solved: complex shapes require thousands of individually designed SSTs with uniquely interacting domains, a requirement that can limit their scalability.

Complex structures have been recently built using wireframe approaches: grids of double helical domains are connected via multi-arm junctions to generate 3D structures. Relative to DNA origami, these structures are less tightly packed and, as a consequence, have the potential to be more stable in physiological conditions [78, 47, 137, 15]. Systematic topological design of these structures is challenging and can represent an obstacle to their size scalability. Finally, the largest existing DNA nanostructures have been built using a "tensegrity triangle" motif [92, 141], which generates three dimensional crystals that can grow scalably up to hundreds of micrometers in size. These structures rely on sticky end domains to connect the four-armed junctions of the tensegrity triangles; they can be useful as rigid scaffolds for other ligands, or as biocatalysis vehicles [39].

1.4 RNA nanostructure design largely relies on single-stranded building blocks with stable tertiary structures

RNA is an ideal self-assembling molecule for biomedical applications: it is a polymer dynamically produced by cells; it is more stable than DNA at low pH; finally, many RNA nanoparticles (such as ribozymes, aptamers, and siRNA) are functional molecules [61, 87]. By combining functional domains and domains programmed for assembly, RNA nanostructures can control the spatial arrangement of functional molecules [42, 45]. RNA nanotechnology is an emerging field with recent demonstrations of structural assembly of large RNA arrays [21], large tiles [38], and small 3D structures such as cubes and rings [2]; functionalized structures were utilized successfully as vectors for cancer and HIV therapies [3, 5] (Fig. 1.3).

The self-assembly pathways of RNA include Watson-Crick base pairing and non-canonical base pairing (for instance, G-U wobble pairs); stacking interactions are also stronger than in DNA. Noncanonical base pairing characterizes many evolutionarily conserved tertiary structure motifs, which are not found in DNA. Established methods for RNA nanostructure design heavily rely on this variety of natural RNA motifs to produce complex and functional nanostructures [14]. These motifs have non-arbitrary sequences and generally rely on folding of relatively short, single-stranded elements. HIV kissing loops are the most heavily used motif to build large RNA assemblies.

Single-stranded RNA molecules with specific tertiary structure are building blocks, or tecto-RNAs, in "RNA architectonics", one of the most established methods for RNA nanostructure design [54]. Tecto-RNA elements with desired 3D geometric interactions are identified with NMR or X-ray crystallography. Then, 3D structures are mapped into secondary structures and into a finite number of single-stranded RNA sequences that yield the desired RNA motif. The direction, spacing and angle at which tecto-RNA elements interact can be determined from the known crystal structure of the sequences [123]. Tecto elements can be identified starting from published structures or databases; RNAJunction, for instance, provides a list of junctions, kissing loops, internal loops and bulges selected from PDB coordinate files [19]. Softwares such as NanoTiler [18] can be used to compose motifs to fulfill topological specifications and build larger structures. Examples of RNA architectonics include filaments [89] (Fig. 1.3 A), polyhedra [108] (Fig. 1.3 B) and jigsaw puzzle pieces or tectosquares [21] (Fig. 1.3 D, E). Like DNA tiling systems, RNA architectonics relies on interactions among relatively short polymers (30-60 bases); however, the salient feature

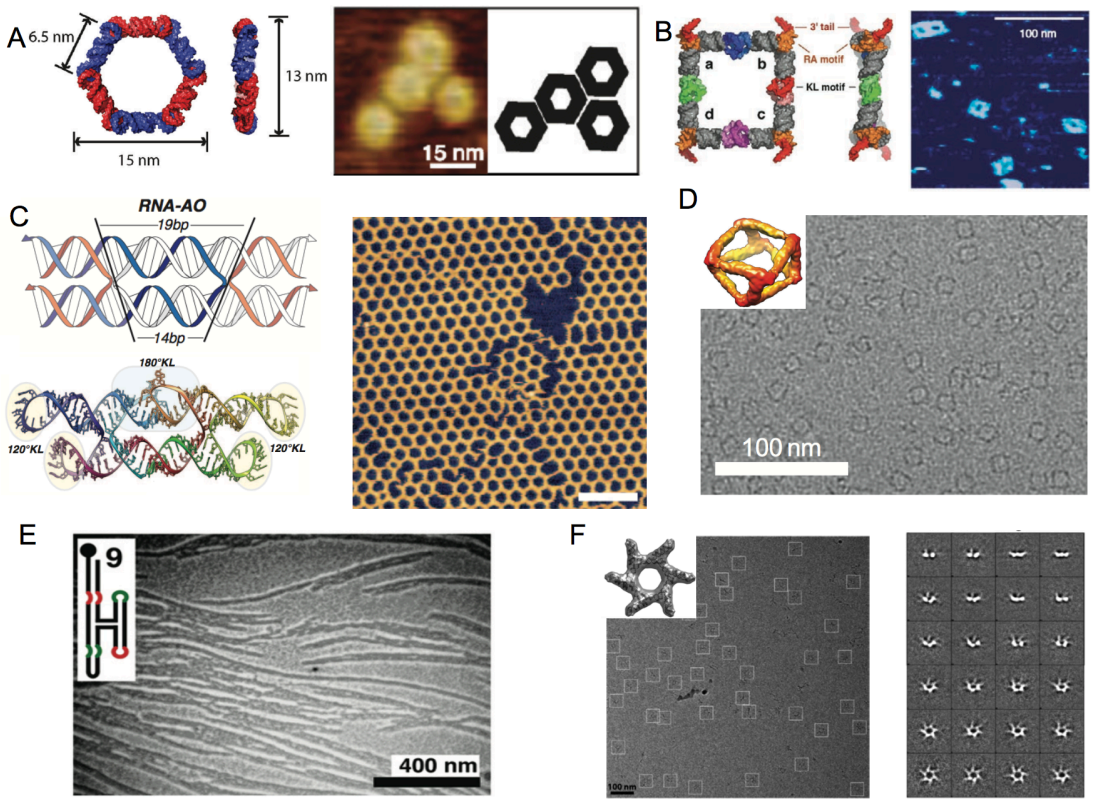

Figure 1.3: **Examples of RNA nanostructures built using traditional RNA nanotechnology design principles** A: Schematic and TEM of RNA filaments assembled from tecto RNA molecules [89]. B: Schematic of RNA anti-prism and cryo-EM of anti-prism particles [108]. C: Single-stranded RNA tile based on DNA DAO tile and AFM image of hexagonal lattice assembly [38]. D: Schematic of tecto-square and AFM image of tecto-squares [21]. E: Schematic of hexagonal RNA nanoring based on kissing loops and AFM images of clustered nanorings [43]. F: Schematic of RNA nanoring functionalized with dsRNA, cryo-EM image of nanorings functionalized with dsRNA, and class averages of of nanorings observed by cryo-EM [8].

of individual tecto-RNAs is their well defined secondary structure, while DNA tile strands are typically designed to present no secondary structure (as isolated strands) and exploit inter-strand Watson-Crick bonds.

The inclusion of long RNA strands in nanostructures poses one major challenge: RNA sequences are more likely to present a large number of local folding traps, which can hinder the formation of the desired assembly. This issue has been recently addressed in a single-stranded RNA origami tile approach [38], which actively exploits local folding of long strands; tiles of variable size (from 2 helix DX tiles to 6 helix tiles) were demonstrated and successfully assembled in larger structures (Fig. 1.3 C). These single-stranded tiles were designed from the DNA-AO and DNA-AE tile geometries, where domain lengths were adapted to A-form helices (Fig. 1.1). Sticky ends are substituted with kissing loop domains and crossover domains are replaced with kissing loop interactions at a 180 angle. In terms of assembly size, RNA origami tiles have the potential to grow in a scalable manner like DNA tile-based systems; the largest lattice size reported in [38] measures roughly 500 nm. These structures are transcribed and folded in a one-pot reaction, and their assembly is mica-assisted. These structures have the potential to be successfully expressed *in vivo*.

Because RNA can be encoded into genes and transcribed inside cells, isothermally assembling RNA nanostructures could be produced *in vivo* and function as programmable scaffolds. Tecto-RNA based structures may be difficult to produce *in vivo*: protocols used for their assembly require several annealing and purification steps (Table 1.2). Tertiary structures may not fold as predicted without annealing and in the absence of appropriate ionic conditions; their misfolding may lead to low yield and unwanted interactions between

the RNA nanostructure and cellular components. It may be possible to circumvent these limitations by using *de novo* design methods akin to those used in DNA nanotechnology.

1.5 *De novo* design methods from DNA nanotechnology can be adapted to RNA

As outlined in the previous sections, established RNA nanostructure design approaches vastly rely on conserved, single-stranded sequences folding into known secondary and tertiary structures that yield inter-molecular interactions of predictable geometry. In contrast, DNA nanostructure design methods are largely based on *de novo* design and *in silico* optimization of an ensemble of sequences, where individual strands are generally required to have minimal secondary structure; multi-stranded double helical domains are connected via suitable junctions and sticky ends. In principle, this approach could be ported to RNA nanostructure design and yield RNA nanostructures with complexity comparable to that of DNA nanostructures [139]. Additionally, double helical binding domains, in contrast to kissing-loop motifs, may be immediately interfaced with a variety of nucleic acid dynamic circuits based on strand displacement reactions [136, 135].

Afonin and coauthors demonstrated *de novo* designed 3D RNA scaffolds [2], where target structures were designed using NanoTiler [18] and Accelrys Discovery Studio [117] to produce 3D computer models; sequences were identified using Monte Carlo optimization algorithms. These structures were demonstrated to assemble co-transcriptionally, showing their potential for *in vivo* expression (Fig. 6.5 A). Recently, the assembly of a rationally

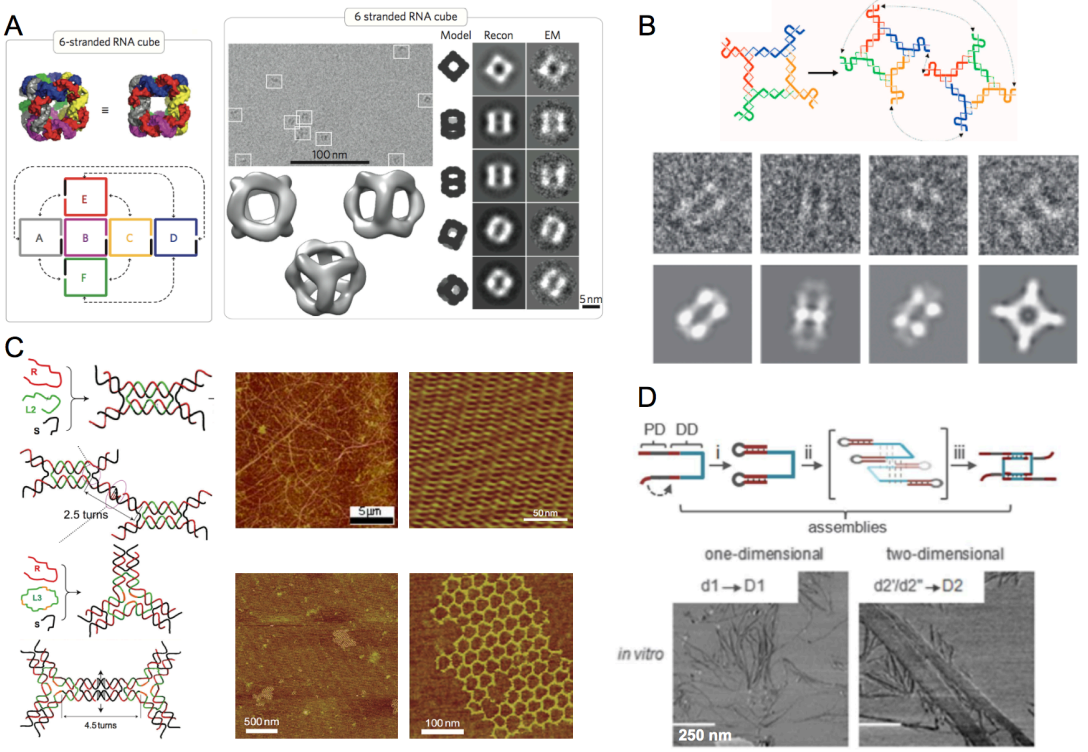

Figure 1.4: **Examples of RNA nanostructures built using traditional DNA nanotechnology design principles** A: Schematic of multi-stranded RNA cube and TEM images and reconstruction of RNA cubes [2]. B: Schematic of tetramer tile, Cryo-EM and reconstructured images of RNA nanoprism [132]. C: Schematic of multi-stranded DNA/RNA hybrid tiles that assemble into lattices and AFM images of hybrid DNA/RNA tubular and lattice structures [65]. D: Schematic of RNA tile formation and AFM images of filaments and lattices assembled *in vitro* and used for *in vivo* scaffolding [23].

designed *de novo* RNA nanoprism was achieved using the DNA T-junction motif [132]. The nanoprism formed from "S-shaped" double stranded monomers that include two T-junction motifs. One T-junction motifs causes the monomers to form a tetramer and the other causes tetramers to dimerize and form a prism (Fig. 6.5 B). T-junction motifs rely on binding of sticky ends to a single-stranded loop. These structures are capable of co-transcriptional

assembly as Afonin's nanocubes; however, in both cases abortive transcripts are prevalent and results in a lower target structural yield and unwanted assemblies.

RNA nanostructures were built using directly the DNA origami approach in [32]. A helix bundled tile and helix bundled tube were designed with a long RNA scaffold strand and small RNA staple strands to aid in folding into the desired structure. Assemblies were also obtained with chemically modified RNA scaffolds. This RNA origami has a limited size of approximately 40 nm, which may be difficult to scale up due to possible kinetic traps in the scaffold strand. As noted earlier, the origami method appears to be less scalable than tile-based assemblies that produce nanometer to micron-sized structures.

A hybrid DNA/RNA DX tile system, where sequences are optimized *in silico* using Sequin [105] was demonstrated in [65]. These tiles assemble in tubular or ribbon-like structures that can grow up to several microns in length (Fig. 6.5 C). Because DNA/RNA helices fold in A-form as RNA-RNA helices (Fig. 1.1), it is reasonable to expect that the same DX tiles could be built using solely RNA strands. These RNA tiles could generate large, scalable semi-rigid assemblies and demonstrate that tiling methods for DNA nanostructure design can be ported to RNA.

A single crossover tile with the potential to assemble into 1D and 2D scaffolds in vivo was proposed in [23]. Tiles were designed from sequence symmetric RNA monomers, which bind to form dimers; polymerization of dimers can occur through sticky ends (Fig. 6.5 D). Polymerization and dimerization domains were designed to generate a reaction funnel, so that dimerization occurs first, followed by polymerization: sticky ends are protected by hairpins and become exposed only after dimerization. Self-assembly is achieved via

	DNA		RNA	
Method	**Tiles**	**Origami**	**Tecto-RNA**	**De novo design**
Components	MS or SS Short strands (20-60 bases) In silico design Arbitrary sequence design space	MS Scaffold (kilobases) and staple strands (20-60 bases) Design constrained by scaffold	MS and SS Short strands (20-60 bases) SS tertiary structure Conserved sequences	MS and SS Short strands (20-60 bases) In silico design
Structural features	Holliday junctions SS/DS domains Sticky ends	Holliday junctions SS/DS domains Sticky ends/stacking bonds	Holliday junctions Tertiary structures; SS/DS domains Loop-loop interactions	Arbitrary sequence design space Holliday junctions SS/DS domains Sticky ends T junctions
Examples & references	Lattices and ribbons [127, 37, 100, 91, 69] Tubes [99, 85] 2D patterns [130, 125, 49, 50, 70] 3D patterns [59, 60, 76]	2D patterns [98] 3D patterns [28, 24, 40]	Filaments, lattices [38, 89, 68] Rings, cubes, prisms, tubes [21, 108, 131]	Lattices [65] Rings, cubes [132]
Applications	Algorithmic assembly [127, 100, 80] Functionalization with ligands [85, 111]	Scaffolding [122, 71] Biomimetic assays [48]	Drug delivery [45, 3, 5]	Spatial organization of proteins [23, 101]

Table 1.1: Summary of the most common design approaches to build DNA and RNA nanostructures. List of abbreviations: MS, multi-stranded; SS, single-stranded; DS, double stranded; SST, single-stranded tile.

formation of double helical domains and Watson-Crick base pairing, other than kissing loop interactions, in contrast to RNA tecto elements. These structures incorporate hairpin loops to localize cellular components, and were used to increase the yield of a hydrogen producing pathway in bacteria. The simplicity and hierarchical assembly of these tiles suggests that this design is well conceived for co-transcriptional isothermal assembly. AFM images provided in [23] indicate the assembly of structures with sizes in the range of 200–300 nm, however the structure of individual tiles or the yield of correct assemblies is unclear (Fig. 6.5 D). Recently, an RNA DAO-O tile motif [99] was used to successfully co-localize enzymes *in vivo* [101], but features and yield of the assemblies are yet to be identified.

	DNA			RNA
Method	**Tiles**	**Origami**	**Tecto-RNA**	**De novo design**
Buffer conditions	TAE; Mg^{2+} [99] or $Ni^{2+} or Na^{+}$	TAE or TE; Mg^{2+} or Na^{+} [98, 46, 20, 64]	TB; $Mg^{2+} and K^{+}$ and/or Na^{+} [21, 43]	TB; Mg^{2+}, K^{+} [2]; TMS; and/or Na^{+} [113]
Thermal treatment	From > 90°C to RT [99, 31]	95°C to 20°C [98], 95°C to 4°C [46]	Snap cooling, 95°C to 4°C, to pre-fold tectos; then incubation at 30°C prior to gel extraction. For tectosquares assembly cool 50°C to 4°C [21, 43]	Snap cooling, 95°C to 45°C, then incubation at 30C [2, 38]. Slow cooling from 80°C to 4°C [113]
Assembly time	Individual tiles: 5 minutes to 2 hours [64] ; for entire structure 16-24 hours [64] [64]	For single layered objects: > 2 hours [98, 46]; for multi layered objects: several days [28]	Snap cooling >1 hr; slow cooling 16 hours, mica-assisted [21, 43]	>1 hr [2]; slow cooling [113]

Table 1.2: Summary of protocols used to produce DNA and RNA nanostructures (abridged). List of abbreviations: TA, Tris Acetate; TE, Tris EDTA; TAE, Tris Acetate EDTA; TB, Tris Borate; TBE, Tris Borate EDTA; TMS, Tris Magnesium Saline; RT, room temperature.

1.6 Challenges and outlook

An exciting research direction in the field of RNA nanotechnology is the development of *in vivo* large assemblies. These artificial cellular scaffolds could serve functional purposes and localize molecular components, as recently suggested [23, 101]; it may be even possible to use cells as factories to produce and expel RNA scaffolds for other applications. *In vivo* assembled structures should form isothermally without a compromise in yield, and should not be toxic to cells or tissues, as well as having a functional role. We identify two critical research areas that present several challenges: 1) Predictive design software is needed to identify feasible and simple structural designs with high likelihood of yielding correct assemblies. Because tectonic elements may be difficult to fold, a possible route could follow the DNA nanotechnology approach: multi- or single-stranded RNA structures could be designed by minimizing the secondary structure of individual strands, while maximizing the binding probability of double stranded domains, relying on Holliday junction structural rules. 2) Assembly methods should be a one-pot, isothermal process with a focus on co-

transcriptional assembly in biocompatible conditions; in contrast, the majority of existing RNA structures require specific annealing protocols (Table 1.2). Co-transcriptional methods should primarily produce the correct product with minimum abortive and elongated transcripts.

There are several nucleic acid software packages that support nucleic acid nanostructure design; the majority focus on DNA [134, 105, 29, 10]; very few of these programs can be used for both DNA and RNA, and even fewer programs are geared directly for RNA [109, 56]. The most used programs for RNA nanostructure design are NanoTiler [18] and RNA2D3D [83]. NanoTiler is used to optimize motif arrangements and helical spacers, given a target topology; motifs can be identified from the RNAJunction database [19]. NanoTiler is also capable of sequence optimization. NanoFolder is an online utility for sequence design and secondary structure prediction of multi-stranded RNA systems, which can handle pseudoknots [16]. As NanoFolder, NUPACK can optimize RNA sequences needed to produce simple multi-stranded target secondary structures, with single or multi-state targets, and with concentration specifications; however, NUPACK does not handle pseudoknots [134] and it is mostly targeted to reaction pathway design. Both NanoTiler and NUPACK do not offer 3D visualization of structures. Based on primary and secondary structure information, RNA2D3D generates a 3D model. The model and/or the user-defined sections can undergo energy minimization and short molecular dynamics; however this software is not intended as a tool for 3D visualization of *de novo* designs. It is worth remarking that, to our knowledge, none these softwares can handle ionic conditions that deviate from standard scenarios. The availability of integrated toolboxes, with features comparable to DNA toolboxes (such

as Tiamat [126], SARSE [11], or caDNAno [29]), will enable the automated construction of capable of large scale RNA structures and vastly expand the range of achievable RNA structures.

Co-transcriptional assembly eliminates the time-consuming laborious steps involved with the extraction and purification of RNA. Furthermore, it is the first step toward expressing the desired RNA nanostructures *in vivo*. However, undesired transcriptional behaviors commonly encountered *in vitro* suggest that it will be challenging to obtain *in vivo* self-assembly with high yield and low error rates. Two most undesirable phenomena are the production of a) large amounts of abortive transcripts and b) elongated (run-off) products; these phenomena are frequently observed in bacteriophage polymerase-based *in vitro* transcription. Abortive transcripts are the result of the relative instability of the transcription complex in the initial stages of transcription [82, 52, 121]; these transcripts can be 2–13 bases long and may form stable complexes competing with the desired assemblies; abortive transcription has recently been measured *in vivo* as well [41]. Abortive transcription is sequence dependent, and can be mitigated usign G-rich transcription initiation sequences [82]. Elongated or "run-off" transcription is a well known phenomenon when using linear templates for transcription [120]: incorrect products with up to twice as long as the desired transcript can reach 70% of the total synthesized RNA. This phenomenon appears to be a self-coded process, and it can be reduced by enforcing strong secondary structure at the 3' end of the transcript [120, 63]. Unfortunately, the imposition of specific sequence content or secondary structure to ensure correct yield of products can limit the nanostructure sequence design space.

Despite several technical challenges are yet to be solved, the field of structural RNA nanotechnology has demonstrated a variety of large assemblies. We suggest that one future research direction for the field is the construction of responsive, dynamic RNA structures. Dynamic control of RNA assembly would yield spatial and temporal control over self-organizing RNA molecules. Applications would include, for instance, more efficient RNA-mediated drug delivery methods, where functional RNAs may be designed as a "passenger" on a large structure that can only be released upon recognition of a temporal signal and reconfiguration of the structure itself. Another fundamental goal would be that of producing dynamically controllable *in vivo* assemblies to localize cellular components both spatially and temporally, mimicking the function of cytoskeletal scaffolds. RNA structures *in vivo* could respond to transcription factors that control their production or to physical stimuli via aptamers.

We believe that *de novo* nanostructures built with a single or multi-stranded tile system would serve as an ideal candidate for dynamic reconfiguration in comparison to origami assembly. DNA tile topologies would be easily adaptable to RNA with suitable adjustments that account for their different geometries (Figure 1.1). DNA single-stranded tiles (SST), for instance, could serve as a starting point to build RNA SSTs assembling into tubes or sheets with scalable dimension. DNA SSTs can assemble isothermally in biocompatible conditions [88], which suggests that their RNA analog could have similar properties. While reconfiguration of origami structures is possible, it is limited by the large number of specific, semi-rigid interactions between the staple and scaffold strands dynamic [138]. In contrast, tile systems assemble scalably and thus they can disassociate

and reconfigure easily. Assembly, disassembly, and reconfiguration of structures may be controllable via toehold mediated branch migration [133, 136, 35]. This approach has been used, for instance, to switch the conformation of a 2D DNA lattice [33]; assembly of DNA nanotubes has been triggered with a complex catalyst DNA circuit [135], demonstrating that two different classes of nucleic acid devices (dynamic circuits and nanostructures) can operate synergistically. It is unclear whether strand displacement networks could be easily interfaced with RNA nanostructures built from tectonic motifs, such as the large RNA origami tiles demonstrated in [38]; to our knowledge, displacement or strand invasion of tertiary structures such as kissing loops has not been investigated.

Herein this thesis we demonstrate the assembly of RNA nanostructures using design principles used in DNA nanotechnology to assemble single and multi-stranded tile systems. Individual strands are designed to present no individual secondary structure and interact through Watson-Crick base pairing for individual tile assembly and through stick-end hybridization to form larger structures on the nano and micro scales. We not only present the ability of assembly, but also reconfiguration through toeholded branch migration, as well as functionalizing individual tiles and larger RNA structures with functional RNAs for gene silencing. This work demonstrates that design methods borrowed from DNA nanotechnology have the potential to expand further the complexity of achievable RNA nanostructures. Further applications include using these structures as delivery vectors for multiple RNA nanoparticles, as well as the possibility of large *in vivo* RNA structures to serve as programmable scaffolds to spatially control or compartmentalize other cellular components.

Chapter 2

Self-assembly of multi-stranded RNA motifs into lattices and tubular structures

2.1 Introduction

Self-assembled nucleic acid nanostructures are becoming increasingly important in therapeutic applications and synthetic biology because they serve as programmable, versatile scaffolds to organize an ever expanding variety of ligands [139, 42]. RNA scaffolds present several advantages relative to DNA: they can be transcribed in large amounts [2, 38], can naturally include functional domains that are exclusive to RNA [5], and present better immune compatibility relative to DNA [119] for transfection and delivery of molecular cargo.

Here we demonstrate that multi-stranded RNA double crossover (DX) tiles assem-

ble into large arrays and tubular structures, which can exceed one micron in size. RNA structure assembly is characterized by gel electrophoresis, atomic force microscopy (AFM), and transmission electron microscopy (TEM). We find that assembly correctness and yield are affected not only by tile sequence content, but also by nick position on the tile helices. We find that some of the tubular structures are chiral, and can be interpreted as left-handed (none of the tubes can be unambiguously interpreted as right-handed). Assemblies are obtained with two distinct protocols; one where RNA strands are annealed after individual gel extraction, and one where RNA components are simultaneously transcribed, and subsequently annealed without gel extraction

2.2 Results

2.2.1 Design of RNA tiles

RNA tiles were designed according to one of the double crossover motifs proposed by Ko et al. [65] to build DNA-RNA hybrid tiles, because DNA-RNA duplexes are expected to have A-form geometry as RNA-RNA duplexes. Some of the DNA-RNA hybrid motifs used by Ko et al. resulted in tubular structures, so we reasoned that by importing the same motifs we could build RNA nanotubes.

As shown in Fig. 2.1 A, three unique RNA strands (Sa, Sb, Sc) are designed to have WC complementary domains that interact forming five-stranded tiles, where two helices are held together by two four-way antiparallel Holliday junctions, or crossovers (hence the DX nomenclature); the intra-tile crossover distance is 22 base pairs (bp) or two full RNA

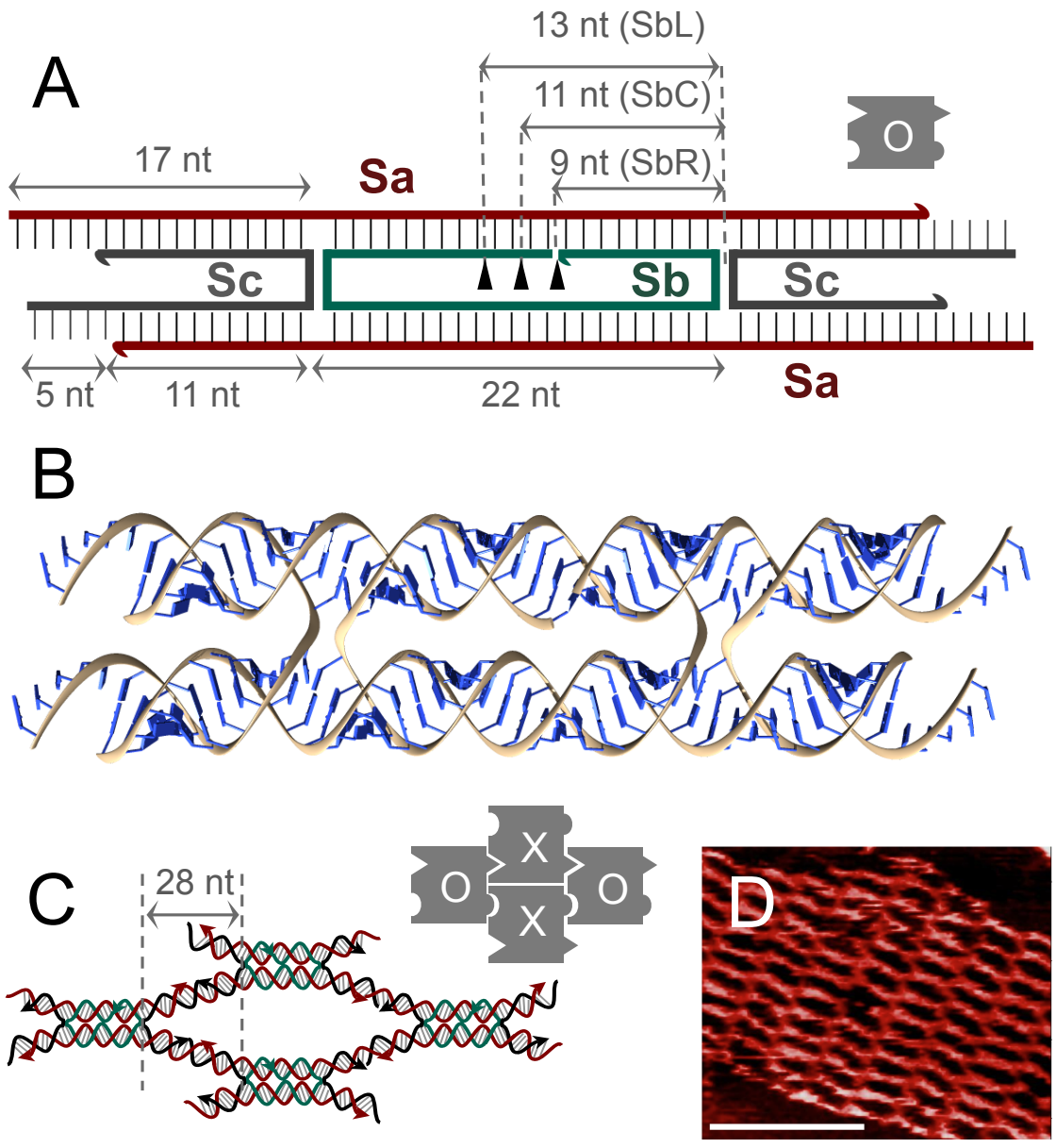

Figure 2.1: **Design of DX RNA tiles** A: Schematic of DX RNA tile [65] and tile abstraction (gray). We tested tiles where the nick in strand Sb can be centered (SbC) or shifted two bases to the right (SbR) or to the left (SbL) of the midpoint between crossovers. B: Three dimensional rendering of the DX RNA tile motif. C: Expected lattice geometry, where tiles assemble in an alternate facing up (O-marked tile) and facing down (X-marked tile) pattern. D: Example AFM image of lattices obtained with tiles presenting a right-shifted nick (design D1R described in the text). Scalebar is 50 nm.

helical turns (in comparison, 21 bases result in two full DNA helical turns). These DX tiles are therefore similar to the DAE-E DNA tile motif [37, 99]. Taking as a reference the tile schematic in Fig. 2.1 A, the position of the nick in strand Sb was chosen to be centered (SbC), two base pairs to the right (SbR) or two bases to the left (SbL) of the crossover midpoint. Tiles interact via 5 nucleotides (nt) long overhangs or sticky-ends, whose complementarity is depicted in the gray tile abstraction in Fig. 2.1 A. A Chimera [93] rendering of this tile motif with right-positioned nick is in Fig. 2.1 B. The inter-tile crossover distance is 28 nt (Fig. 2.1 C). Because this distance is close to 2.5 turns (29 nt), adjacent tiles are expected to assemble in a face-up (O-marked tile in Fig. 2.1 C), face-down pattern (X-marked tile) which should yield flat lattices. Yet in (right-positioned nick) hybrid DNA-RNA tiles [65] an inter-tile crossover distance slightly deviating from exactly 2.5 turns appears to promote formation of tubular structures. An example AFM image of assembled RNA tiles is shown in Fig. 2.1 D.

Because sequence content can affect the yield and stability of nucleic acid assemblies, we tested two different sets of sequences for the same tile motif in Fig. 2.1 A. The first set of sequences, indicated as D1, was chosen by converting to RNA the sequences in Ko et al. [65], which were originally identified using Sequin [105]. Design D1 includes variants D1R, D1C, and D1L where the nick position in strand Sb is changed according to Fig. 2.1 A (while strands Sa1 and Sc1 are unchanged). A second set of sequences, D2, was chosen using the DNA Design Toolbox [30, 26] (built on the Vienna RNA package [51]), by writing a computer script that requires the minimization of unwanted secondary structures at 37°C. The absence of secondary structure in each strand of D2 at 37°C was confirmed

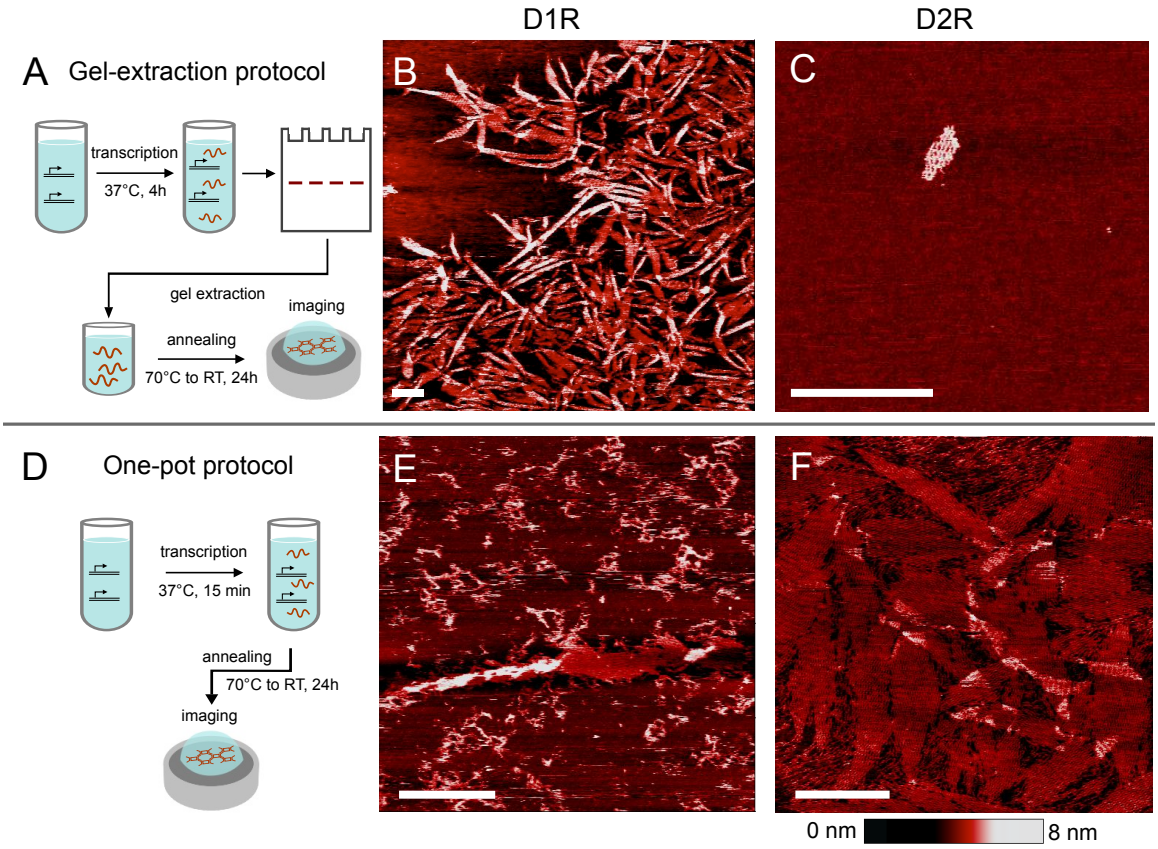

Figure 2.2: **Assembly methods and results** A: Gel extraction and anneal protocol, showing templates with T7 promoter (black lines with bent arrows), RNA transcripts (red lines), and tile assembly. B: Example AFM image of assemblies obtained from tile D1R. C: Representative image of small lattices obtained from tile D2R. D: One-pot transcription and anneal protocol. E: Example AFM image of tubular structure produced from one-pot assembly of tiles D1R. F: Lattices formed by one-pot assembly of tiles D2R. Scale bar: 250 nm.

using NUPACK [134]. Design D2 includes variants D2R, D2C, and D2L, where only the nick position in strand Sb is varied.

RNA molecules were transcribed from linear templates under control of the T7 bacteriophage promoter. Because transcription yield is significantly reduced in the absence of at least two G nucleobases after the +1 promoter position, we incorporated this constraint when designing sequences for tile D2R.

2.2.2 Assembly methods

RNA nanostructures are typically assembled using post-transcription procedures that include gel extraction and thermal annealing treatments [22, 132] to eliminate transcripts of incorrect length and misfolded strands. Thus, in our first set of experiments individual strands of tiles D1R and D2R were transcribed, gel-extracted, mixed at appropriate stoichiometry in TAE and 12.5 mM $MgCl_2$ buffer, heated to 70° C and cooled to room temperature over 24 hours [65] (Fig. 2.2 A).

In Fig. 2.2 B and C we show AFM images of this gel-extraction self-assembly protocol for tiles D1R and D2R; images are representative of the typical structures observed in each sample of triplicate experiments. Tile D1R yields many high aspect ratio lattices and curled ribbons which are consistent with the presence of tubular assemblies that open up as they land on mica. (A phenomenon commonly observed in DNA tubular assemblies [99].) The formation of tubular assemblies is consistent with our expectations based on earlier results by Ko and coworkers [65]. AFM imaging compresses these soft samples and the height difference between open (single-layer) and closed (double-layer) structures is 2.049 nm ± 0.269, in agreement with the expected diameter of double helical RNA

(2.3 nm).

We asked if aggregation of nanostructures in our images is promoted by the presence of Magnesium cations in solution; we found that aggregation appears to decrease at lower $MgCl_2$ concentration, however the yield of assembly decreases as well. We then asked if tile concentration could have an effect on aggregation: at a 12.5 mM $MgCl_2$ concentration, we varied the annealed tile concentration between 50 nM and 0.5 μM, and we found that aggregation persists even at low annealing concentrations. Aggregation makes it difficult to measure length and width of ribbons and tubular structures, which often overlap and appear to branch. We selected AFM images of 10 isolated, partially closed, tubular structures from each of three separate assembly experiments, and we measured an average length of 489 $\pm$ 140 nm and an average width of 46 $\pm$ 5 nm. The longest isolated nanotube assembled from D1R tiles measured 1.03 μm, but several tubular assemblies exceeding one micron in length can be identified among overlapping structures (Fig. 2.2 B).

We further tested a one-pot protocol in which all strands are simultaneously transcribed in the appropriate buffer for 15 minutes, immediately heated to 70° C, and cooled over 24 hours (Fig. 2.2 D). This protocol has the advantage of avoiding laborious gel extractions that can cause loss and degradation of significant amounts of transcript. Abortive and elongated RNA molecules produced during the transcription reaction, and not eliminated by gel extraction contribute to generating a "noisy" assembly environment, where strands with incorrect length can promote formation of spurious assemblies. Despite the presence of these unwanted products, the one-pot protocol yields assemblies for both tile designs D1R (tubular assemblies) and D2R (flat lattices), as shown in Fig. 2.2 E and F. The size of D2R

lattices largely exceeds that of the corresponding samples obtained with the gel-extraction protocol. Assembly of variant D1RE, which includes a single stranded overhang in strand S1a, was rapidly tested using the one-pot protocol.

As can be seen in (Fig. 2.2 B), the yield of lattices is vary a lot depending on the tile design. It is not possible to arrive at a rigorous quantitative assessment of lattice yield based on AFM or TEM images. But we could get a qualitative idea about the yields based on the ease with which we could locate lattices under AFM for various samples. The yield of lattices depends not only on the sequence of strands and annealing protocol, but also on subtle features of tile design such as the nick position. We have discussed the qualitative picture of yield for all the variant designs in the later section dealing with relevance of nick position for the assembly.

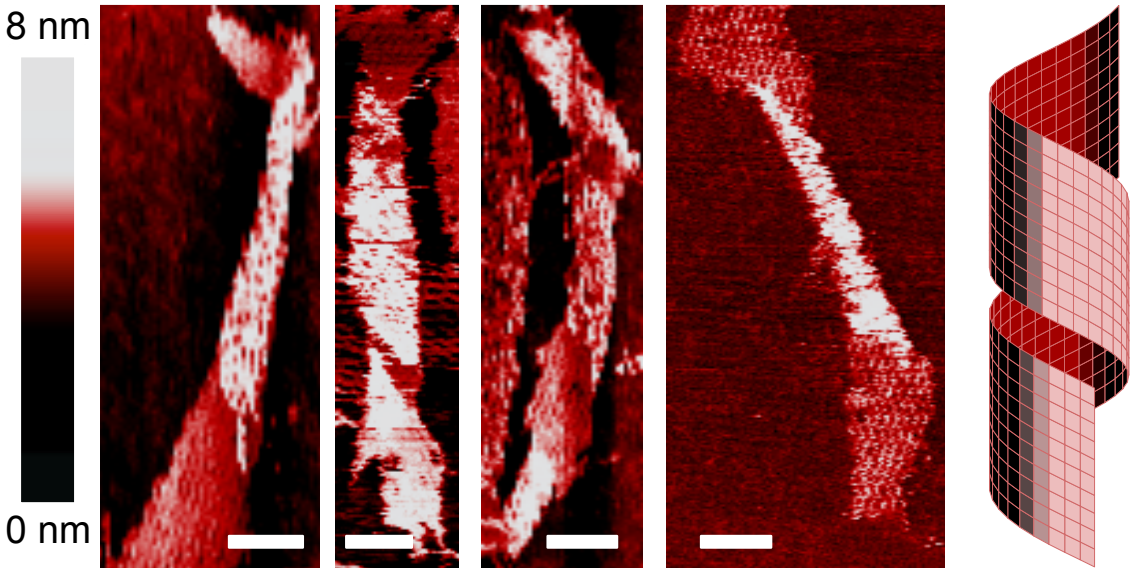

Figure 2.3: **Example AFM images of chiral tubular structures formed by D1R tiles** The chirality feature is presumably promoted by a combination of sequence content and tile geometry. Scale bar is 50 nm. Right: rendering of a left-handed chiral sheet as a guide to the eye.

2.2.3 Assembly morphology is sequence dependent

AFM images of structures produced from tile D1R reveal that many assemblies are tubular and chiral, as shown in the examples selected in Fig. 2.3. The chirality can be interpreted in all cases as left-handed. Formation of tubular structures is unexpected given the face-up, face-down tile assembly pattern, which should yield flat lattices (Fig. 2.1 C), but consistent with the behavior of the hybrid DNA-RNA version of this motif [65]. It is important to note that similar DNA DX tiles assemble into nanotubes due to the binding angle between adjacent tiles [99], and the tube axis is usually parallel to the helical axis. Rather, these RNA tubes form by coiling, where an array folds back to itself orthogonal to the helical axis. We observed formation of tubular assemblies exclusively in variants D1R

and D1RE. We hypothesize that tile sequence content influences self-assembly morphology, and may or may not promote chirality: comparison of AFM images of D1R and D2R tile assemblies, which only differ in tile sequence content, suggests that our hypothesis is valid, because tile D1R consistently yields tubular assemblies (with both assembly protocols), while tile D2R exclusively forms lattices (with both assembly protocols).

2.2.4 Nick position is critical for assembly

We further asked if chirality may also be related to the asymmetry of the nick position in strand Sb. In DNA duplexes, the presence of a nick leads to enhanced flexibility at the location of the nick [94]. The position of the nick in the tile might affect how the stresses during self-assembly bend the tile double helical domains, which in turn would influence the curvature of lattices. To test this hypothesis, we modified strand Sb obtaining tiles with a central nick position (tiles D1C, D2C) or a left-shifted nick position (tiles D1L, D2L). (The different nick positions are shown in Fig. 2.1 A.) Tiles were then assembled according to the gel-extraction and one-pot protocols described earlier.

Only tile design D1R consistently yields chiral tubular structures, using either assembly protocol. Tile D2R only yields lattices, and so do tiles D1L and D2L, which assemble into structures qualitatively similar to D2R. In case of D1R (extracted and one-pot protocols), D2R (one-pot protocol), D2L (extracted protocol) and D2L (one-pot protocol), we could readily observe many structures on mica during AFM imaging. In case of D2R (extracted), D2L (extracted) and D1L (one-pot), we could only identify few lattices upon scanning many locations on mica under the AFM. No large structures assemble from tiles

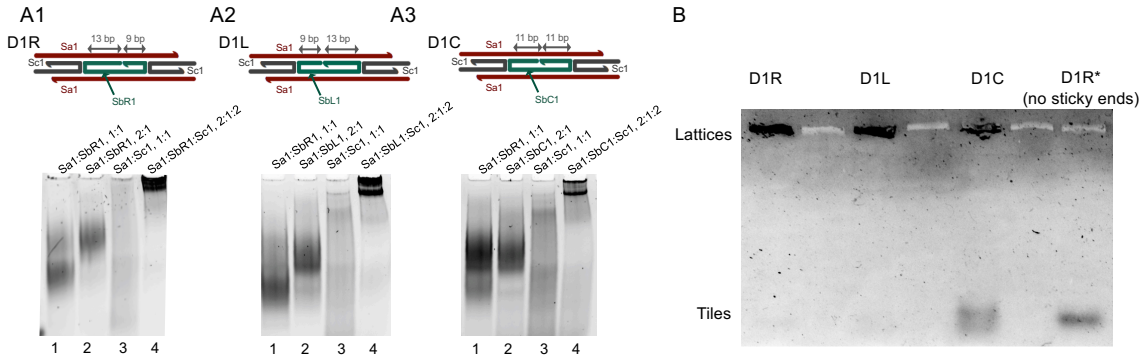

Figure 2.4: **Gel analysis of assembling structures** Strands were gel extracted and annealed prior to loading them into the gel. Panels A1, A2, and A3: non-denaturing PAGE gels comparing complexes that form as part of tile variants D1R, D1L, and D1C. Each lane was loaded with annealed strands as annotated on top of the gel. Ratio 1:1 indicates that both strands were annealed at a 1 μM concentration; ratio 2:1 indicates concentrations 1 μM : 500 nM; ratio 2:1:2 indicates concentrations 1 μM : 500nM : 1 μM. Bands forming in lanes 1 and 2 provide information on the formation of the core of the tile; Sa and Sb in stoichiometric amounts are expected to form smaller complexes relative to the case where Sa and Sb are in the 2:1 ratio required for tile formation. In variant D1C, the two cases are indistinguishable, which suggests improper formation of the tile core during annealing. B: Agarose gel of annealed tile variants D1R, D1L and D1C, compared to non-multimerized annealed tile variant D1R*. A significant fraction of annealed tile D1C runs roughly as the D1R* control complex, indicating that D1C assemblies are not as robust as in the other variants.

D1C and D2C, where the nick is in a central position in the core strand. We do observe small, loose filaments in the AFM images of the D1C sample. Using TEM, which gives much lower resolution, we were able to locate nanotubes for only the D1R (extracted) sample, as shown in the appendix chapter 6. Clear TEM images could not be obtained for the one-pot annealed samples, due to the significant background noise.

Non-denaturing polyacrylamide gel electrophoresis analysis (PAGE) in Fig. 2.4 A1-A3 highlights differences between the complexes formed by the tile with a symmetric nick (D1C) and the ones with an asymmetric nick (D1R and D1L). Gel lanes 1 and 2 test the interactions between Sa and Sb strands. The Sa:Sb strands at 1:1 ratio are expected to run at a lower position (lane 1) compared to strands at 2:1 ratio (lane 2): this is because at 2:1 ratio two Sa strands should bind to one Sb strand. This expected result is verified for tiles D1R and D1L. But for tile D1C, the bands in both lane 4 and lane 5 run at the same position. This could be because the 2:1 ratio complex does not form well in the D1C design. A similar analysis was conducted on design D2 variants, however significant RNA degradation during annealing does not allow us to make conclusive observations on the results. We also examined tile variants D1R*, D1C* and D1L*, from which we removed the sticky end domains (this tiles cannot multimerize). Non-denaturing PAGE of annealed tiles D1R* and D1L* yields single bands; in contrast, D1C* samples yield two distinct bands, that suggest the formation of incompletely or incorrectly formed tiles. The lower band in lane 6 for D1C* sample corresponds in length to the Sa1 and SbC1 complex in lanes 4 and 5, which suggests that during the anneal this complex does not further self-assemble with Sc1 strand properly to form a tile.

In addition, agarose gel electrophoresis was used to compare multimerizing D1R, D1L and D1C tiles. Fig. 2.4 B shows that a significant fraction of annealed tile D1C runs closer to the band of the annealed control tile (D1C*) without sticky-ends. This confirms that D1C monomers have the capacity to form some higher order complexes, which however do not appear to be as structured as those formed by tiles D1R and D1L.

These results overall indicate that nick position is an important parameter in the design of DX RNA tiles. Tiles with asymmetric nick positions (relative to the midpoint between the intra-tile crossovers) consistently form lattices, while the tiles with symmetric nicks do not form lattices. This is true for both D1 or D2 sequence design variants. To our knowledge, similar phenomena have not been observed in DNA tiles: for example, DAE-E tiles consistently form nanotubes even when the nick position in the central strand is varied, as long as the inter-tile distance is appropriately chosen [99, 111, 85]. It is unclear why the centrally nicked designs fail to form lattices. The non-denaturing gels show that the there is a problem misformation of the monomer tile with a central nick. This is likely to be the reason why they do not form lattices. Further studies are needed to elucidate why exactly the centrally nicked tile designs result in misformed tiles. The change of nick position also results in change in morphology of the tiles formed, with only D1R resulting in tubular structures and the rest resulting in flat lattices. But further study and computational modeling is needed to check if the tile flexibility induced by the position of the nick can create different lattice morphologies.

2.2.5 Role of thermal annealing.

In both assembly protocols, a heating temperature of at least 70°C is required for lattice formation. Isothermal one-pot production of D1R and D2R tiles only results in tangled filaments. This outcome is not surprising, as thermal annealing is required for assembly of DNA DX tile motifs as well. One possibility is that secondary structure in individual strands creates a barrier to isothermal tile assembly (however, tile D2R strands were specifically designed to have no secondary structure at 37°C). Our results indicate that thermal annealing is essential for multi-stranded RNA tiles to form and bind. This limitation may be overcome by designing hierarchical assembly steps for tile components [23].

It is known that RNA degradation rates increase at high temperature and in the presence of Magnesium cations [74], which make the phosphodiester bonds more reactive: denaturing gels indicate that significant degradation occurs in all variants of design D2 upon annealing, but not in D1 variants. We hypothesize that this difference may be due to different sequence content and secondary structure of individual strands, as both factors affect phosphodiester bond cleavage rates [58]. We also note that one-pot produced D2R tiles, which are annealed in transcription mix, form very large lattices (Fig. 2.2 E), which indicates that degradation may also be influenced by the composition of the buffer.

2.3 Discussion and conclusion

We demonstrated that large RNA nanostructures can be built from multi-stranded DX tiles, a classical motif in DNA nanotechnology [104, 65]. In contrast with most methods to build large RNA assembled structures, which rely on conserved tertiary interactions

such as kissing loops [54, 22, 89, 108], these tiles assemble exclusively via double helical complementary domains whose sequence can be rationally determined within an ample design space.

Multi-stranded DX tiles qualitatively similar to our design were produced *in vivo* for colocalization of split fluorescent reporters and of metabolic pathway components [23, 101], whose output was used as indirect evidence of co-transcriptional structure formation. These RNA tiles were originally designed by Delebecque et al. [23], and resemble a DAO double crossover tile [37]. However, unlike the well characterized standard DNA DAO tile, this design includes unmatched bases and wobble base pairs. The presence of unmatched bases can make it difficult to control the angle between two interacting tiles because they become connected through unmatched, floppy domains. As a result, it is difficult to enforce the formation of rigid lattices. In addition, Geary et al. [38] later demonstrated that a proper RNA DAO tile requires the two intra-tile crossover domains to have different length, due to the tilt of bases in (A-form) RNA. The design by Delebecque et al. does not take into account this requirement, therefore it is unlikely to yield a correct DAO tile (however, unmatched bases and wobble pairs may relax the spatial constraints posed by the incorrect length of intra-tile crossover domains). Unfortunately, the low resolution of AFM images provided in [23] makes it difficult to unequivocally determine whether the tessellated lattices or tubular structures are formed as desired.

Our multi-stranded structures were obtained with a protocol based on gel extraction as well as with a one-pot method where all strands are simultaneously transcribed and subsequently annealed. Previous studies [2, 132, 124] reported successful one-pot assembly

of smaller multi-stranded RNA or RNA-DNA structures (up to 100 nm large and about 1000 bp). The one-pot method is less laborious, and often produces structures of equal or larger size than those obtained with the gel-extraction method, despite the presence of well known phenomena of abortive and elongated (run-off) bacteriophage transcription [120, 52, 41]. These processes generate undesired RNA strands presenting incorrect length and unknown folding. Abortive transcription is sequence dependent, and can be mitigated using G-rich transcription initiation sequences [82]. Elongated or "run-off" transcription occurs in linear templates for transcription, and incorrect products with up to twice as long as the desired transcript can reach up to 70% of the total synthesized RNA [120]. This phenomenon can be reduced by enforcing strong secondary structure at the 3' end of the transcript [120, 63]. Another challenge in the one-pot protocol is posed by uneven transcription rates, which can cause stoichiometric imbalances among strands and reduce assembly yield. This issue can be straightforwardly mitigated by including promoter-appropriate transcription initiation sequences and balancing the template concentrations. The imposition of specific sequence content or secondary structure to ensure correct yield of products can unfortunately limit the nanostructure sequence design space. Feedback mechanisms that automatically increase or decrease the production of molecules depending on the downstream demand could also help balancing the transcription rates and the stoichiometry of components [36].

Thermal annealing is required for assembly of our structures. Isothermal assembly of multi-stranded RNA nanocubes was demonstrated using an assembly-activated light-up aptamer [2]. However, our results indicate that co-transcriptional isothermal assembly for multi-stranded RNA DX tiles remains challenging. While multi-stranded, short compo-

nents have the advantage of being less prone to local folding traps, a more successful route to isothermal assembly is given by long single-stranded tiles explicitly designed to take advantage of local folding [38]. Another feasible approach to isothermal assembly is the design of strands that can exclusively assemble with an ordered sequence of reactions [23].

We find that the morphology of our assemblies is affected by sequence content. While the D1R tile sequence produced many chiral nanotube structures, the D2R tile sequences produced only lattices (with both assembly protocols). The sequence could directly affect the geometry of the tile and hence change the morphology of the assembly. Additionally, the degradation of RNA after annealing, seen in design D2 could also lead to changes in geometry of some of the tiles which in turn affects the morphology. Further, assembly is also affected by the position of the nick on the nicked helix of the tile, a design parameter that is not known to pose similar challenges in DNA self-assembly. Our gel assays suggest that the lack of lattices with centrally nicked tile designs could be due to misformation of tiles with a central nick.

It would be useful to predict the influence of sequence and nicks on RNA assembly using advanced computational modeling tools. Computational characterization of RNA nanostructure assembly, validated by experiments, has been successfully demonstrated [4]. However, existing RNA sequence design toolboxes are not fully equipped for *de novo*, rational construction of large assemblies based on Holliday junction motifs, because they are either tailored to tecto-RNA elements (conserved sequences and tertiary interactions) [19, 83] or to design reaction pathways [134] rather than nanostructures. Advances in rational design of RNA scaffolds will highly benefit from integrated software toolboxes akin to those

available for DNA nanostructures [126, 11, 29]. It is likely that coarse-grained simulations to predict the primary vibration modes of tile monomers [95] will help explaining emergent assembly patterns such as the chiral tubes we observed.

Large RNA lattices may be functionalized with protein-binding domains or small RNA molecules with therapeutic properties (siRNA, microRNA, or antisense RNA) [7, 110]. While our lattices are not suited for *in vivo* isothermal assembly, they can be produced *in vitro* and transfected as scaffolding elements or drug delivery vectors, as we recently demonstrated [116]. The spontaneous chirality of some of our assemblies makes them potentially useful as scaffolds for synthesis of optically active biomaterials [71], although additional investigation is required to quantitatively elucidate this feature.

Chapter 3

Programmable RNA microstructures for coordinated delivery of siRNAs

3.1 Introduction

Previously we demonstrated that multi-stranded RNA double crossover (DX) tiles can assemble into large arrays and tubular structures via design principles employed in DNA nanotechnology. Next, we investigated the potential for these structures to be functionalized with dicer substrate RNAs for the intracellular release of siRNA for gene silencing. RNA is a key biological regulator with a remarkable natural capacity to form stable, complex assemblies in vivo (the human ribosome, for instance, is a structure containing over 7 thousand nucleotides). Thus, large artificial RNA constructs should be compatible with the cellular

environment, providing a programmable platform for delivery and organization of molecular loads. Yet, structural nucleic acid nanotechnology has focused primarily on DNA due to the stability and predictability of its Watson-Crick base-pair interactions [127, 98, 27]. Currently, only few methods are available in the emerging field of RNA nanotechnology [44] that allow programmable multistrand assembly of RNA constructs with size exceeding a few hundreds of nanometers [38, 21, 73, 68, 23]. We demonstrate that designing principles developed for large-scale DNA self-assembly may be successfully adapted to RNA and support the development of large RNA scaffolds.

Multi-stranded RNA structures, rationally designed to assemble exclusively via double helical domains, have been demonstrated in vitro [2, 5, 132, 16]. However, their size is limited to the nanometer-scale as well. Despite of all potential benefits, the thorough characterization of functional RNA tile motifs with the capacity for large-scale, modular assembly is still lacking. The first attempts to build RNA tiles based on the crossover motif were performed to develop a metabolic engineering platform in E. coli, where enzymes could be localized by 0D, 1D or 2D RNA assemblies [23, 101]. Individual tiles were functionalized with aptamer domains that, upon tile assembly, co-localize split fluorescent reporters or catalysts. Although the functional behavior of these assemblies met the expectations, confirming the tile interactions, structural features and robustness of assembly are yet to be elucidated. Furthermore, these tiles are not suitable for construction of precisely engineered lattices due to base-pairing mismatches within the tiles, which result in formation of less rigid structures.

Here we describe and characterize a functional DX RNA tile motif designed de

novo, that forms lattices with the capacity to reach the micron-scale, analogously to existing DNA DX tiles. This design is based on a DX tile motif originally designed for synergistic assembly of tiles with hybrid components of both DNA and RNA [65]. We decorate the DX RNA tile with siRNA domains, we generate assemblies in vitro, and we demonstrate: 1) the formation of regular lattices that are robust upon the addition of functional domains (as verified via AFM imaging and gel electrophoresis), and in some cases exceed one micron in size; 2) the uptake and viability of functional tiles and lattices in human breast cancer cells; 3) the capacity of functional tiles and lattices to silence target genes in transfected cells, with multivalent siRNA domains. Our results demonstrate that rational design of large, functional RNA nanostructures has the potential to match the complexity and size of scaffolds built with DNA, with improved bio-compatibility for delivery and scaffolding.

3.2 Results

3.2.1 Design of functional tiles

We designed DX RNA tiles adapting the motif proposed by Ko et al. [65], originally developed to build hybrid DNA-RNA tiles. This motif, qualitatively similar to a DAE DNA tile [37], is designed according to the parameters of A-form helical geometry (expected in RNA double helices). The tile consists of five RNA strands, of which only three have a unique sequence and are denoted as Sa, Sb, Sc; these RNA strands interact to generate two helical domains connected by two crossovers (Fig. 3.1 A, left). Tiles bind when their sticky-end domains (5 nucleotides long) hybridize, forming a double helix, and upon binding they form an alternating lattice pattern of tiles facing up and down. The intra-tile crossover

distance is two full RNA helical turns (22 bp) and the inter-tile crossover distance is about two and a half helical turns (28 bp), as described in previous work [115]. To functionalize the tile, strand Sc was extended to include antisense silencing RNA (siRNA) sequences. As a proof of concept, we tested two siRNA sequences that target against 1) green fluorescent protein (GFP), incorporated in Sc strand variant Sc-AG, and 2) polo-like kinase 1 (PLK1), incorporated in strand Sc-AP (Fig. 3.1 A, right). To provide the Dicer-assisted intracellular release of the siRNAs, we used Dicer Substrate RNAs [97] (DS RNAs) that were tested in our previous works [17, 9]. We assembled tiles that include exclusively one (Sc-AG or Sc-AP), both types (Sc-AG and Sc-AP) of DSRNA molecules, or none (as a control). Assemblies including both siRNA domains (50% Sc-AG and 50% Sc-AP) incorporate the domains at random locations in the structure, with an expected uniform distribution. Sense DS RNA strands targeted against GFP was labeled with Alexa 488, and the sense DS DNA strand targeted against PLK1 was labeled with Alexa 546. In the case of PLK1, whose downregulation causes an induction of apoptosis34, fluorescently labeled DNA was used to prevent the dicing and the siRNA release that may cause the undesirable cell death during the uptake experiments.

3.2.2 Tile and lattice assembly

All constructs were obtained by slowly annealing RNA strands mixed in the appropriate stoichiometry; each RNA strand was separately transcribed and gel extracted (Fig. 3.1 B). Lattices were assembled from RNA strands including sticky ends, which are required for polymerization; individual tiles were assembled by removing the sticky end

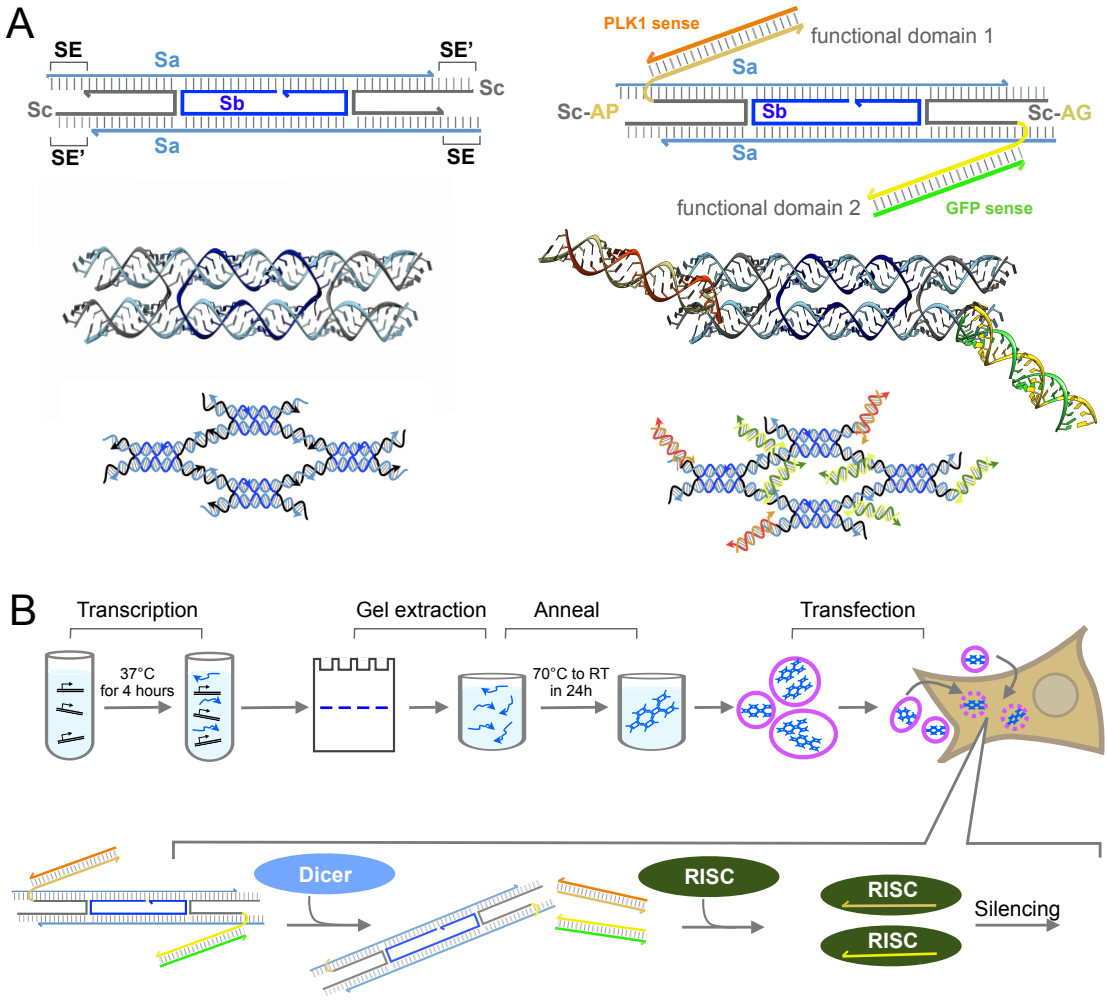

Figure 3.1: **RNA constructs for delivery of siRNA molecules are prepared in vitro and transfected into cells** (A) Left: (top) expected secondary structure of DX RNA tile (Ko et al.),29 emphasizing the complementarity pattern of sticky end (SE) domains; (middle) Chimera46 rendering of the RNA DX tile; (bottom) expected lattice assembly. Right: (top) expected secondary structure of the functionalized DX RNA tile, where antisense DS RNA domains are incorporated on strand Sc; to demonstrate functionality we choose to target GFP and PLK1; (middle) Chimera46 rendering of the functional tile; (bottom) expected lattice assembly. (B) Top: Steps of our construct preparation protocol, starting from in vitro transcription to transfection of the constructs in human breast cancer cells; Bottom: summary of the siRNA release pathway.

domains. Assembly of tiles and structures in vitro was characterized via AFM imaging and non-denaturing PAGE. AFM images in (Fig. 3.2 A) show that lattices assemble in all variants of our functional tiles (either a single type of siRNA domain, or two distinct siRNA domains). The DS RNA domains sticking out of the lattices are not visible because they are connected to the lattice by a loose linker (UU). Tiles yield lattices with similar nano-scale features, but different morphologies (flat lattices and tubes). In some cases assemblies appear to have a fixed width, which suggests that tubular structures may form in solution and open upon landing on the mica. Some of the lattices reach the micron size. The presence of siRNA domains in the lattices was verified via gel fluorescence analysis, by using fluorescently labeled sense RNA strands. As shown in (Fig. 3.3 B), fluorescent bands co-localized with bands corresponding to lattices and tiles indicate successful incorporation of siRNA domains.

3.2.3 Transfection of tiles and lattices

Assembled functional tiles and lattices were transfected in human cells, and we assessed their capacity for gene silencing of GFP or PKL1, or both (Fig. 3.3). All functional constructs were gel purified prior to transfection, as detailed in the Methods section. Control experiments indicate that lipofectamine encapsulation does not cause disassembly of individual tiles. In all experiments, equivalent concentrations of free DS RNAs were used as control. To assess the relative uptake efficiencies, human breast cancer cells were transfected with fluorescently labeled functional tiles and lattices (Fig. 3.3 A-B). The results demonstrate dose dependent response with relatively higher transfection efficiencies for tiles

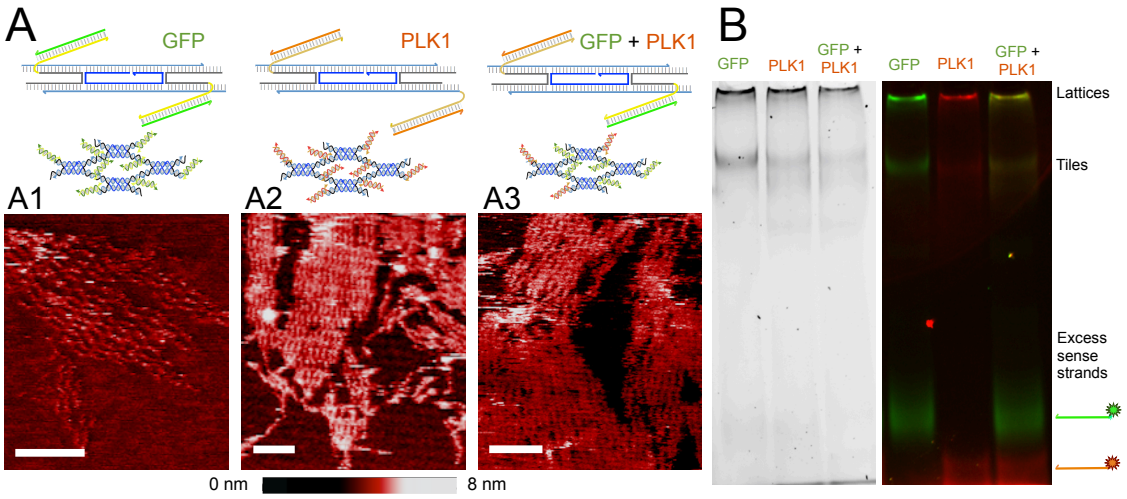

Figure 3.2: **Functional DX RNA tiles assemble into lattices** (A) Construct schematics and AFM images of lattices assembling from tiles functionalized with GFP DS RNA domains (A1), PLK1 DS RNA domains (A2) and both GFP and PLK1 domains (A3). Scale bar: 50 nm. (B) Gel electrophoresis of con- structs including fluorescently labeled sense RNA molecules. Fluorescent bands indicate that DS RNA sense strands are incorporated in complexes that do not enter the gel (presumed to be lattices/polymerized tiles) and in individual tiles without sticky ends; the same pattern is observed in mono- and multi-valent tiles (with both PLK1 and GFP domains).

(blunt-ended), which are the smallest tested constructs. Interestingly, the uptake efficiencies at lower concentrations (5 nM or lower) are very comparable between the constructs and free DS RNAs, while at 20 nM 3-fold increase in relative uptake is observed to free DS RNAs compared to functionalized assemblies. This difference can be explained by the saturation of the transfection agent (Lipofectamine 2000) with RNA in the case of larger assemblies. The viability of cells was not affected by transfections with different assemblies (Fig. 3.3 C). To confirm that the assemblies stay intact in cells after the transfection, fluorescence co-localization experiments were carried out (Fig. 3.3 D-E). In these experiments, tiles and lattices carrying in their composition both fluorescently labeled strands (Alexa 488 and Alexa 546) were visualized after the transfection. While we observe some separation of the dyes from the constructs (e.g. upon degradation), multiple co-localized signals were still measured in both transfected tiles and lattices. These results suggest that transfected constructs are structurally intact.

3.2.4 Functional tiles and lattices successfully silence target genes

To validate the intracellular release of functional siRNAs, we carried out specific gene silencing experiments. First, as a proof of concept, GFP expressing breast cancer cells (MDA-MB-231/GFP) were transfected with constructs carrying anti-GFP siRNAs (Fig. 3.2 A1) and free DS RNAs. The results in (Fig. 3.4 B-C) show concentration dependent GFP silencing with comparable efficiencies (of 90%) for assemblies and DS RNA at nanomolar concentrations. However, at lower picomolar range of concentrations, DS RNA was shown to be the most efficient silencer followed by tiles with the lattices being the least

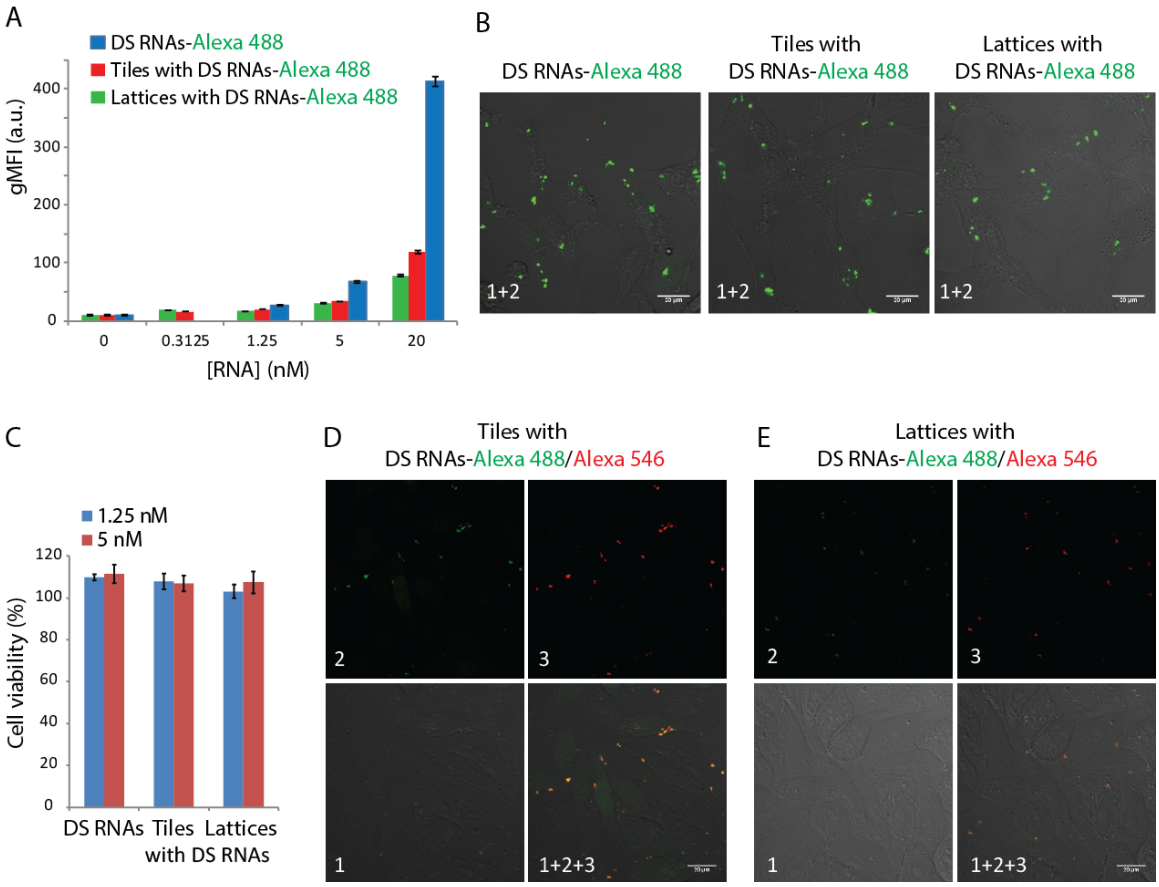

Figure 3.3: **Functional DX RNA tiles assemble into lattices** (A) Construct schematics and AFM images of lattices assembling from tiles functionalized with GFP DS RNA domains (A1), PLK1 DS RNA domains (A2) and both GFP and PLK1 domains (A3). Scale bar: 50 nm. (B) Gel electrophoresis of con- structs including fluorescently labeled sense RNA molecules. Fluorescent bands indicate that DS RNA sense strands are incorporated in complexes that do not enter the gel (presumed to be lattices/polymerized tiles) and in individual tiles without sticky ends; the same pattern is observed in mono- and multi-valent tiles (with both PLK1 and GFP domains).

efficient (Fig. 3.4 C). To attribute the silencing of GFP to the presence of functionalized RNA constructs, non-functionalized tiles and lattices were tested as negative controls and showed no silencing (Fig. 3.4 B). The GFP silencing was observed for 10 days with a quicker fluorescence recovery for cells treated with functionalized lattices. To show the generality of the approach and the therapeutic potential of RNA nanoassemblies, human prostate cancer cell line (PC3) was transfected with constructs functionalized with anti-PLK1 DS RNAs (Fig. 3.2 A2). PLK1 is a well-validated molecular target [96], whose down-regulation causes an induction of apoptosis and impairment of mitosis machinery in human prostate cancer cells; thus, PLK1 silencing studies have implications for the treatment of prostate cancer. Cell viability experiments (Fig. 3.4 D) clearly demonstrated dose-response with the results consistent with what observed in GFP silencing at higher concentrations, constructs and DS RNAs cause comparable extent of cell deaths while at lower concentrations, tiles outperform lattices.

3.3 Discussion and conclusions

We demonstrated that the DX tile motif, well known in DNA nanotechnology, can be used to build functional RNA tiles assembling into large lattices. Tiles were functionalized by incorporating two distinct siRNA domains for GFP and PLK1, which can be release intracellularly via dicing. Lattices and tiles were transfected into human breast cancer cells, where they were stable, viable, and performed the desired inhibition of gene expression.

Constructs robustly assembled in the presence of the DS RNA double stranded domains. However, we observed that lattice growth is affected by the presence of the DS

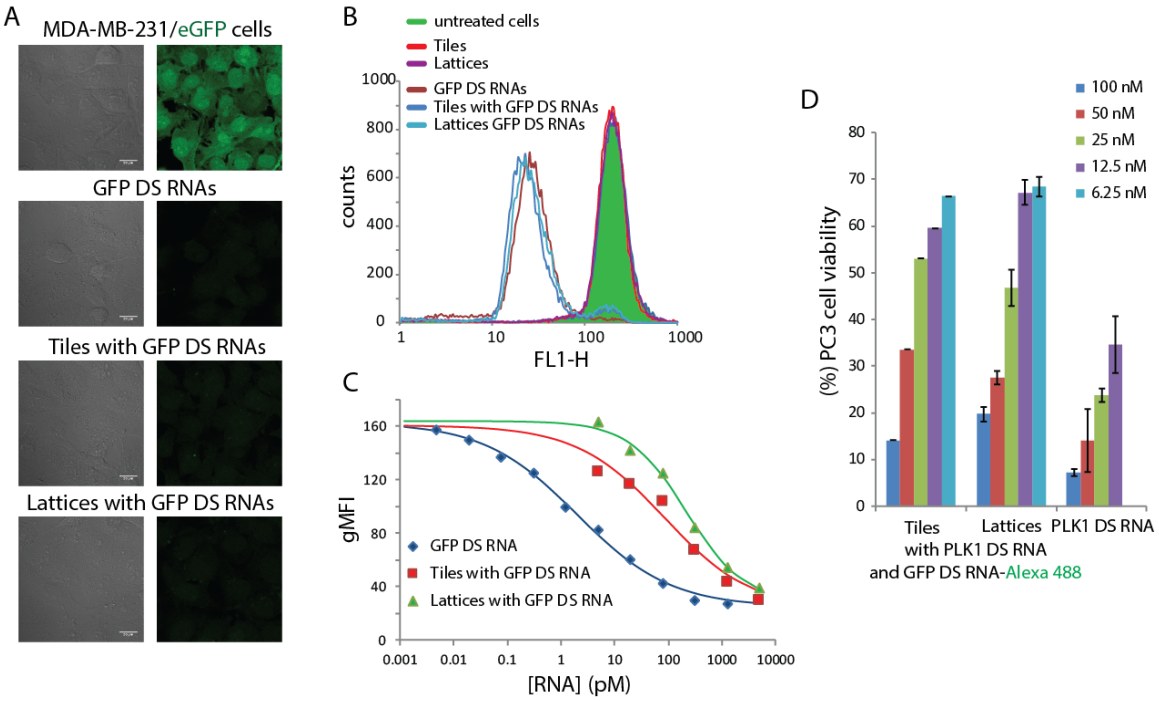

Figure 3.4: **Specific gene silencing triggered by functionalized RNA tiles and lattices** Down regulation of GFP expressed by human breast cancer cells was assessed by A: fluorescent microscopy and B: flow cytometry. C: Different concentration of constructs tested for relative silencing efficiencies. D: As an alternative, PLK1 silencing in human prostate cancer cells was assessed through cell viability assays. Cell viabilities are normalized to the non-treated cells and error bars denote SD, N = 3.

RNAs. In particular we found that, depending on the sequence of the siRNA domain, constructs may either form lattices or tubular assemblies. When no functional domains are present, we observe tubular structures that typically have a left-handed chirality (the source of chirality is yet to be elucidated [114]. Tubular structures also formed when both siRNAs domains are targeted against GFP. However, lattices were observed when both DS RNAs attached are targeted against either solely PLK1 or against both GFP and PLK1 simultaneously. We speculate that, upon further investigation, this feature may be rationally exploited to obtain structures with switchable 3D organization which may be enzymatically controlled (for instance, by dicing siRNA domains).

DNA and RNA nanostructures have been successfully used to deliver several nanoparticles, especially in targeting the stimulation of cellular immune response [62] or for gene silencing [90]. For instance, DNA structures were used to deliver gold nanoparticles or antibodies [27], CpG [118] and doxorubicin [55]; 10 nm-sized DNA tetrahedra were also used to deliver siRNA molecules [72]. Yet, nm-sized DNA nanotubes of functionalized with siRNA [67] were not stable in cells, and no siRNA activity was observed. Delivery of siRNA has been demonstrated with several RNA nano-scale structures such as pRNA-based assemblies [113], nanocubes [7] and kissing loop motifs used to build the RNA nanorings [43, 8]. To the best of our knowledge, our RNA lattices are the largest RNA constructs successfully used for siRNA purposes.

Thermal annealing is required to form regular lattices with our DX tiles; our results are in contrast with previous reports [101], but largely in agreement with the literature on DNA DX nanostructures [99]. Attempts to fold lattices isothermally only yielded formation

of loose filaments [115]. Thus, the current design of tiles is not suited for in vivo expression and co-transcriptional assembly. Addition of hairpins to hierarchically expose sticky-ends only upon formation of tile crossovers appears to have enabled isothermal assembly in an RNA DX variant expressed in vivo [23].

In conclusion, we presented the DX tile motif that self-assembles and yields RNA lattices of unprecedented size, which are viable in human cells. These constructs are potentially useful for in vivo delivery applications and for stoichiometric co-localization of a large number of components on a planar or tubular surface. This feature might be important in biocatalysis or metabolic pathway engineering. One disadvantage of the presented approach is the inability to precisely control size of the lattices. However, this limitation can be mitigated because the architecture we presented is modular: in principle it is possible to engineer several sequence-distinct tile-types with programmable and even algorithmic interactions [129, 111, 100], which could result in assemblies with controllable size. The most notable advantage of the tiles we presented is their relative designing simplicity and robustness to addition of functional domains; we expect that, in addition to siRNA functions, it will be possible to decorate tiles with aptamers for localization of a variety of ligands.

Chapter 4

A more robust RNA tile design for nanotube assembly

4.1 Introduction

Previously we have demonstrated RNA tile designs that assemble through double crossover motifs and Watson-Crick base pairing that yield large structures [115]. The previous designs mentioned in chapters 2 and 3 had issues in regards to tile design and experimental protocols. In regards to the tile design, the previous tile type consisted of repeated sets of sequences, which may cause undesired interactions [115]. Further, tiles assemble in an alternating up and down pattern, which is not consistent with designs that yield nanotubes in DNA nanotechnology. These issues of the tile design causes issues with experimental protocols such as poor yield, aggregation, and scarcely controllable diameter of the filaments if they form. Thus, we explored alternative designs to reliably obtain RNA

nanotubes with high yield and consistent diameter. Herein, we present a new tile design that yields a more robust assembly and longer tubes that do not aggregate, and can be imaged via fluorescent microscopy.

Here, we demonstrate the assembly of micron sized RNA nanotubes from DX tile motifs. Nanotubes are a common assembly in DNA nanotechnology because of the many possible applications. These structures mimic biological structures such as filamentous proteins found in the cytoskeleton of eukaryotic cells, and can be used as a scaffold and transport cargo [66, 107, 75]. The synthesis of nanotubes built from RNA, a multifunctional polymer presents the opportunity to create smart biomaterials with endless opportunities for drug delivery and facilitating intracellular control and regulation of biological components.

Our assembiles result from canonical base-pairing of few short RNA strands, in contrast with most of the existing RNA structures, which heavily exploit secondary and tertiary structural motifs such as hairpins, loops, and bulges [21, 113, 8, 38]. Relying on secondary and tertiary motifs may present local folding traps making it more difficult to assemble large RNA structures using these design methods. Using multiple short RNA strands can reduce the secondary structures. Additionally, due to the large number of specific interactions using these motifs makes it more difficult for dynamic reconfiguration and making the structure more biologically relevant for applications. Lastly, multiple short strands provide a simple design method to avoid secondary structures

4.2 Results and discussion

4.2.1 Design of double-crossover tiles

To identify the tile design parameters that yield the angle between interacting tiles to produce assemblies, it is useful to compare RNA tiles with their DNA counterpart [99]. The DNA tile is composed of five strands that form two double helical domains via Watson-Crick interactions that form two crossover points. This particular DNA tile has a minor groove face that displays minor grooves at the crossovers and a major groove face that displays major grooves at the crossover. Tiles interact through participant phosphate backbones, meaning that the backbones exchange at the crossovers contrasting with non-participant backbones, which do not exchange. The nonparticipant backbones are present on the minor groove face, at an angle from the plane of the tile of the minor groove, which for typical B-form DNA is 150° 10°. It is important to note that the nonparticipant backbone in one tile will become a participant backbone in the adjacent tile crossovers and defines the plane in the tile where it is a participant backbone. Thus, the angle between two tiles is the minor groove angle which was previously noted to be 150° 10° [99].

We can follow the same ideas used to design DNA tiles however there are differences that should be taken into account. The natural geometry of B-form DNA drastically differs from the geometry of A-form RNA. RNA has a base tilt of 19° compared to a negligible DNA base tilt of 1°. This tilt in RNA makes inter-tile distance difficult to predict and in turn will cause steric hindrance between tiles. The tile-tile angle distribution will not be uniform, as some tiles will have to bend more than others in order to form a tubular structure. Further, it is likely this base tilt contributes to chiral tubular assembles.

RNA tiles were designed using the DNA DAE-E tile type [99], which was adapted to accommodate the geometry of the A-form RNA helix and to ensure high transcription yield. As shown in (Fig. 4.1 A), five RNA strands (S1, S2, S3, S4, and S5) are designed with unique sequences with Watson-Crick complementary domains, where two helices are held together by two four-way anti-parallel crossover points. The intra-tile crossover distance was varied from 21 bp to 22 bp to accommodate for two helical turns of RNA (Fig. 4.1). Our RNA tiles are designed to form defined periodic assemblies over aggregates. To obtain flat lattice formation, interacting tiles should be co-planar. To obtain curved lattices that favor the formation of tubular structures, there is a certain symmetry of tile interaction that must be compatible with a curved geometry, and tiles must interact on different planes. However, given the tilt of RNA base-pairs, it is difficult to predict the ideal distance of neighboring tiles to obtain tubular assemblies (Fig. 4.1B and C) .

In theory, when annealing structures, the length of the sticky ends should not affect assembly (as long as they are greater than 4-5 bases). Yet, the nick position does seem to affect assembly for RNA nanostructures [115]. Therefore, for simplicity we only varied the length of the sticky ends which varied the length of the inter-tile crossover distance without altering the position of the sticky ends. We named the tile variants by the inter-tile and sticky end lengths, for example in (Fig. 4.1A) the inter-tile crossover distance is 24 and the sticky end length is 8 bases, so the nomenclature for this tile variant is 24-8. Hence the core of the tile consisting of S1, S3, and S5 remain the same for all tile variants (with the exception of the 5 base sticky end variant where we extended the length of both S1 and S5), the sticky end strands differ among the tile variants. Further, to investigate the modularity

of this system we designed a two-tile system. This two-tile system is based off the 23-7 tile variant, where each tile type has distinct sticky ends and both tile types are required for assembly.

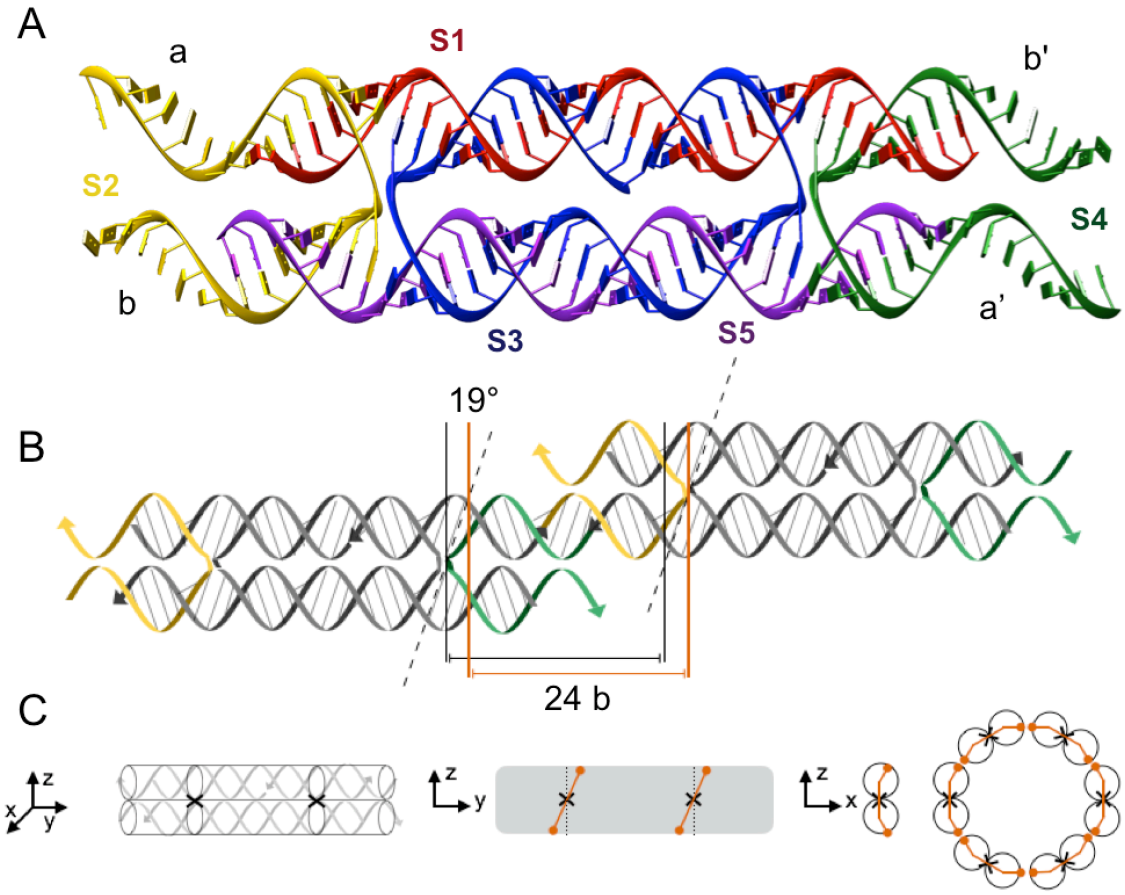

Figure 4.1: **Schematic of tile design and tile-tile hybridization** A. 3D rendering of RNA double crossover tile B. 2D representation of tile C. Two RNA tiles interacting through sticky ends

4.2.2 Characterization of assembly

All structures were obtained by slowly annealing gel-extracted and purified RNA strands mixed in the appropriate stoichiometry. Assembly of structures in vitro were char-

acterized via atomic force microscopy, fluorescence microscopy (Fig. 4.2A, C, and D), and non-denaturing polyacrylamide gel electrophoresis (PAGE). To observe nanoassemblies of tiles in lattices we used AFM (Fig. 4.2A). For the 22-5 tile variant we observed small patches of lattices. The 23-7 and 24-8 tile variants yielded micron-sized tubular structures that also showed lattice formations in open-closed tube structures. The 25-9 and 26-10 tile variants yielded neither lattices nor tubular structures, instead filaments only visible at 1-micron squared areas. To observe large structure formation we incorporated a small amount of a custom synthesized S3 strand with Cy3 labeled located on the 5' end into the tile design (Fig. 4.2B) to visualize the formation of larger structures with fluorescence microscopy (Fig. 4.2C and D).

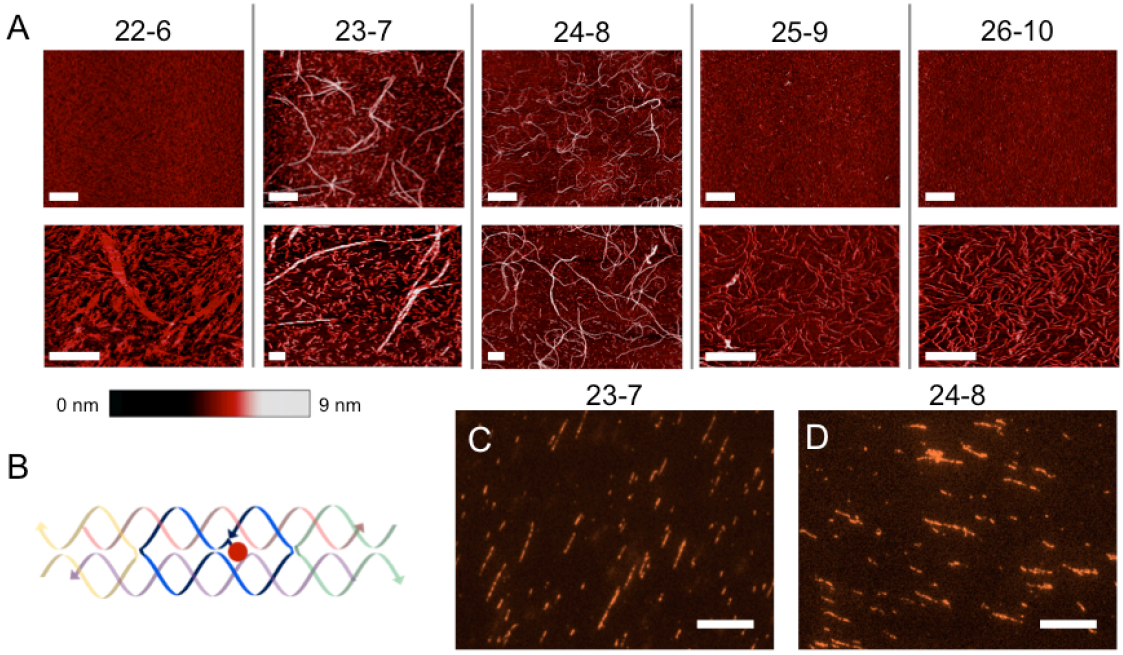

Figure 4.2: **Characterization of tile variants** A. AFM of all tile variants, scale bar top row 1 μm bottom row 250 nm B. 2D scheme of tile, the red dot represents the Cy3 fluorophore C,D. fluorescence microscopy of 23-7 and 24-8 tile variants, scale bar 10 μm

Appropriate inter-tile crossover length for assembly formation (Fig. 4.2) was found to be 2 inter-tile crossover turns + 0, 1, or 2 bases. For formation of tubes only designs with 2 inter-tile crossover turns + 1, or 2 bases. For our RNA tubes we believe the unstrained geometry for tiles is 2 helical turns + 1 base or 2 bases, if this distance is deviated from we observe that tubes no longer be able to assemble.

So, our RNA tile with 22 bp or 2 helical turns inter-tile crossover distance yields only small patches of lattices, we assume interacting tiles are co-planar. For the 23 and 24 inter-tile crossover distances we believe tiles interact on different planes. In the instance of one extra bp between the 22-6 and 23-7 tile variant the extra base may provide the necessary rotation necessary to provide the necessary curvature to form tubes. The addition of one or two extra base pairs to the 24-8 to form 25-9 and 26-10 tiles variants we believe that the additional base either causes high strains prohibiting the formation of large structures.

We measured the diameter of the 23-7 and 24-8 tile variants using AFM images. We chose 100 tubes that did not overlap with other tubes and measured them at the extremes and midpoint (Fig. 4.3). The 24-8 tile measured a smaller diameter with a mean diameter measurement of ≈30 nm with a standard deviation of ≈10 nm in comparison to the 23-7 tile diameter with a mean diameter of ≈75 nm with a standard deviation of ≈33 nm. The addition of a base pair hints at the possibility of inter-tile crossover distance not only determining tube formation as with DNA DX tiles, but also determine diameter unlike DNA DX tiles.

Using fluorescence microscopy images we measured the lengths of the structures. We measured tubes in 10 images, omitting tubes that overlapped with other tubes and any

measurement under 0.3 μm to accommodate the resolution of the microscope. Variations in tube density affected the number of counts per sample. Tube lengths had a mean measurement of $\approx$2 μm, but we also measured tube lengths up to 10 μm in length. The average contour length of DNA DAE-E tile based nanotubes were measured at a mean length of $\approx$7 μm [99]. This difference in mean lengths may be attributed to the DNA system being more energetically favorable to yield larger structures.

4.2.3 Isothermal growth of nanotubes does not occur

We were also interested if these tubes grew over time. We annealed tubes at 1 μM tile concentrations for the 23-7 and 24-8 tile variants and allowed the sample to incubate at room temperature and measured the lengths of the tubes as observed via fluorescence microscopy over 30 hours (Fig. 4.3B and D). For both tile variants it appears that these tubes do not grow at room temperature. The lack of growth indicates a barrier to nanotube nucleation. Without the addition of a known nucleation site the requirement to overcome the energy barrier for assembly is significant [86]. Misfolded tiles may also play a role by binding to the nanotube and prohibiting the binding of other tiles. Additionally, the rate of tubes growing may be equal or smaller to the breakage rate, producing the observation of steady tube lengths over time.

4.2.4 Tiles can be modified to create a modular system

We modified the 23-7 tile variant by changing the sticky end sequences to design a two tile system, where two different sets of tiles are required to assembly a larger structure

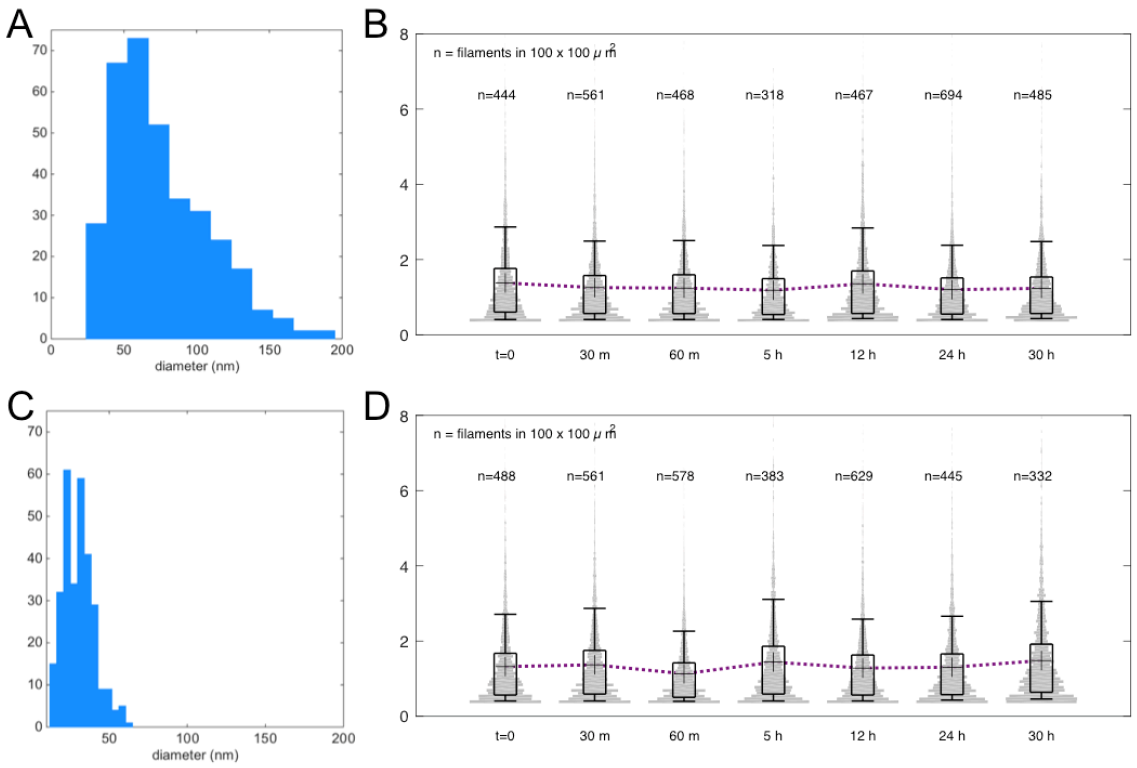

Figure 4.3: **Quantitative characterization of nanostructures** A. Histogram of tube lengths for 23-7 and 24-8 tile variants B. Violin plots of tube length over time for 23-7 and 24-8 tile variants

(Fig. 4.4A). This system forms tubes as the single 23-7 tile system, however, we observed that these tubes are much shorter in length (<2 μm), as well as the yield is qualitatively lower compared to the single tile system, and cannot be observed via fluorescent microscopy. This reduction in yield and tube length may be caused by the sequence content of the sticky end, as in previous studies we have found that this affects assembly [115]. Additionally, we modified the 23-7 tile variant, where we extended the 5' end of the S4 strand (Fig. 4.4B), to create a 5 nucleotide long toehold. Elongating the sticky end does not seem to affect assembly, as nanotubes form, as well as length and yield do not appear to be affected.

4.3 Conclusions

We have demonstrated design methods used to assemble DNA DAE tiles into tubes and lattices by importing these methods to pure RNA structures. These RNA tiles yield a far more robust assembly in comparison to previous works, are modular, and are large enough to be visualized via fluorescence microscopy.

Previously we have demonstrated instances of solely using canonical base pairing to form RNA multi-stranded tiles that interact and form tubular structures via a slow anneal [115, 116]. These structures measured up to 1 micron in length and were capable of being functionalized with dicer substrate RNAs (DSRNAs) for gene silencing. Here, we demonstrate and characterize the formation of RNA lattices and tubular assemblies via slow anneal of double crossover (DX) multi-stranded tiles. These structures are to our knowledge the largest RNA structures with periodic nanoscale features capable of being observed via AFM and fluorescence microscopy.

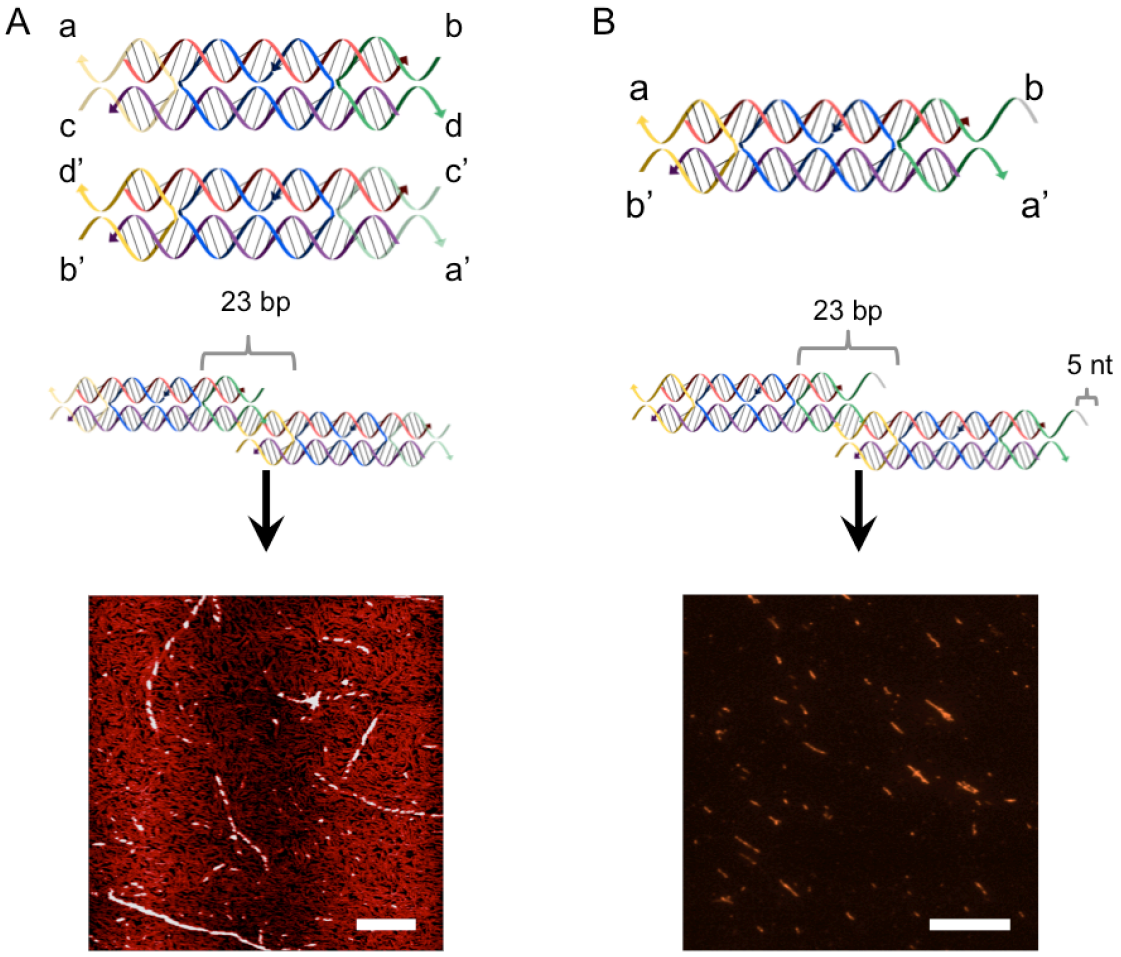

Figure 4.4: **Modified 23-7 tile variant for two tile system and toeholded tile** A. Top: Two tile system designed using the 23-7 tile variant, Middle: Scheme of how two tile system interacts, Bottom: AFM image of tubes assembled from two tile system scale bar 0.5 μm B. Top: Toeholded tile designed using the 23-7 tile variant, Middle: Scheme of how toeholded tile interacts, Bottom: fluorescence microscopy image of tubes assembled from toeholded tile scale bar 10 μm

To verify assemblies and characterize structures we used non-denaturing PAGE, AFM, and fluorescence microscopy. We believe that these large RNA assemblies can be beneficial in in scaffolding large molecules that traditionally would not be able to be scaffolded using RNA nanoparticles, furthermore, these tiles are multivalent allowing for the delivery of different ligands with spatial and temporal control.

Chapter 5

Conclusions

Herein this thesis we demonstrated the assembly of RNA nanostructures using design principles used in DNA nanotechnology to assemble structures from single and multi tile systems. We have demonstrated the importation of design principles used into DNA nanostructure assembly to build double-crossover RNA tiles. These RNA tiles are composed of multiple RNA strands with minimal secondary structure and interact through Watson-Crick base pairing and form larger structures on the nano and micro scales.

We not only present the ability of assembly, but also the modification of individual tiles and larger RNA structures with functional RNAs for gene silencing. This work demonstrates that design methods borrowed from DNA nanotechnology have the potential to expand further the complexity of achievable RNA nanostructures. Further applications include using these structures as delivery vectors for multiple RNA nanoparticles, as well as the possibility of large *in vivo* RNA structures to serve as programmable scaffolds to spatially control or compartmentalize other cellular components.

This work has developed design and experimental methods to obtain synthetic programmable RNA structures that are capable gene silencing abilities. We have completed the two primary objectives: 1) Design and characterize RNA tiles that assemble into RNA nanostructures and 2) Functionalize RNA tiles for RNAi to inhibit gene expression. We believe this work has laid the foundation towards assembling large RNA nanostructures using the design principles used in DNA nanotechnology.

RNA is a programmable nanomaterial that can generate large biologically functional structures. Design methods borrowed from DNA nanotechnology have the potential to expand further the complexity of achievable RNA nanostructures. In particular, tile systems akin to those typically used in DNA nanotechnology can yield very large RNA nanostructures, which could find application as delivery vectors for multiple RNA nanoparticles. Large *in vivo* RNA structures could serve as programmable scaffolds to spatially control or compartmentalize other cellular components. As a continuation of this work for *in vivo* applications it is imperative that these structures are capable of dynamic behavior. Implementing dynamics in large RNA structures remains challenging as the initial difficulty is designing a system that can assemble isothermally. Therefore careful consideration must be taken when selecting sequence content and buffer conditions. Dynamic control of these large structures would provide a further programmable layer of control for cellular processes.

Bibliography

[1] Leonard M. Adleman. Molecular computation of solutions to combinatorial problems. *Science*, 266:1021–1024, 1994.

[2] Kirill A Afonin, Eckart Bindewald, Alan J Yaghoubian, Neil Voss, Erica Jacovetty, Bruce A Shapiro, and Luc Jaeger. In vitro assembly of cubic RNA-based scaffolds designed in silico. *Nature nanotechnology*, 5(9):676–682, 2010.

[3] Kirill A Afonin, Wade W Grabow, Faye M Walker, Eckart Bindewald, Marina A Dobrovolskaia, Bruce A Shapiro, and Luc Jaeger. Design and self-assembly of siRNA-functionalized RNA nanoparticles for use in automated nanomedicine. *Nature protocols*, 6(12):2022–2034, 2011.

[4] Kirill A Afonin, Wojciech Kasprzak, Eckart Bindewald, Praneet S Puppala, Alex R Diehl, Kenneth T Hall, Tae Jin Kim, Michael T Zimmermann, Robert L Jernigan, Luc Jaeger, et al. Computational and experimental characterization of rna cubic nanoscaffolds. *Methods*, 67(2):256–265, 2014.

[5] Kirill A Afonin, Maria Kireeva, Wade W Grabow, Mikhail Kashlev, Luc Jaeger, and Bruce A Shapiro. Co-transcriptional assembly of chemically modified RNA nanoparticles functionalized with siRNAs. *Nano letters*, 12(10):5192–5195, 2012.

[6] Kirill A Afonin, Brian Lindsay, and Bruce A Shapiro. Engineered RNA nanodesigns for applications in RNA nanotechnology. *DNA and RNA Nanotechnology*, 1:1–15, 2013.

[7] Kirill A Afonin, Mathias Viard, Ioannis Kagiampakis, Christopher L Case, Marina A Dobrovolskaia, Jen Hofmann, Ashlee Vrzak, Maria Kireeva, Wojciech K Kasprzak, Vineet N KewalRamani, et al. Triggering of rna interference with rna–rna, rna–dna, and dna–rna nanoparticles. *ACS nano*, 9(1):251–259, 2014.

[8] Kirill A Afonin, Mathias Viard, Alexey Y Koyfman, Angelica N Martins, Wojciech K Kasprzak, Martin Panigaj, Ravi Desai, Arti Santhanam, Wade W Grabow, Luc Jaeger, et al. Multifunctional rna nanoparticles. *Nano letters*, 14(10):5662–5671, 2014.

[9] Kirill A Afonin, Mathias Viard, Philip Tedbury, Eckart Bindewald, Lorena Parlea, Marshall Howington, Melissa Valdman, Alizah Johns-Boehme, Cara Brainerd, Eric O Freed, et al. The use of minimal rna toeholds to trigger the activation of multiple functionalities. *Nano letters*, 16(3):1746–1753, 2016.

[10] Ebbe Andersen and Morten Nielsen. DNA origami design of 3D nanostructures. *Protocol Exchange*, 05 2009.

[11] Ebbe S Andersen, Mingdong Dong, Morten M Nielsen, Kasper Jahn, Allan Lind-Thomsen, Wael Mamdouh, Kurt V Gothelf, Flemming Besenbacher, and Jørgen Kjems. DNA origami design of dolphin-shaped structures with flexible tails. *ACS nano*, 2(6):1213–1218, 2008.

[12] Ebbe S. Andersen, Mingdong Dong, Morten M. Nielsen, Kasper Jahn, Ramesh Subramani, Wael Mamdouh, Monika M. Golas, Bjoern Sander, Holger Stark, Cristiano L. P. Oliveira, Jan Skov Pedersen, Victoria Birkedal, Flemming Besenbacher, Kurt V. Gothelf, and J{orgen Kjems. Self-assembly of a nanoscale DNA box with a controllable lid. *Nature*, 459(7243):73–76, 05 2009.

[13] Robert D Barish, Rebecca Schulman, Paul WK Rothemund, and Erik Winfree. An information-bearing seed for nucleating algorithmic self-assembly. *Proceedings of the National Academy of Sciences*, 106(15):6054–6059, 2009.

[14] Robert T Batey, Robert P Rambo, Jennifer A Doudna, et al. Tertiary motifs in RNA structure and folding. *Angewandte Chemie International Edition*, 38(16):2326–2343, 1999.

[15] Erik Benson, Abdulmelik Mohammed, Johan Gardell, Sergej Masich, Eugen Czeizler, Pekka Orponen, and Bjorn Hogberg. DNA rendering of polyhedral meshes at the nanoscale. *Nature*, 523(7561):441–444, 07 2015.

[16] Eckart Bindewald, Kirill Afonin, Luc Jaeger, and Bruce A Shapiro. Multistrand RNA secondary structure prediction and nanostructure design including pseudoknots. *ACS nano*, 5(12):9542–9551, 2011.

[17] Eckart Bindewald, Kirill A Afonin, Mathias Viard, Paul Zakrevsky, Taejin Kim, and Bruce A Shapiro. Multistrand structure prediction of nucleic acid assemblies and design of rna switches. *Nano letters*, 16(3):1726–1735, 2016.

[18] Eckart Bindewald, Calvin Grunewald, Brett Boyle, Mary O'Connor, and Bruce A Shapiro. Computational strategies for the automated design of RNA nanoscale structures from building blocks using NanoTiler. *Journal of Molecular Graphics and Modelling*, 27(3):299–308, 2008.

[19] Eckart Bindewald, Robert Hayes, Yaroslava G Yingling, Wojciech Kasprzak, and Bruce A Shapiro. RNAJunction: a database of RNA junctions and kissing loops for three-dimensional structural analysis and nanodesign. *Nucleic acids research*, 36(suppl 1):D392–D397, 2008.

[20] Carlos Ernesto Castro, Fabian Kilchherr, Do-Nyun Kim, Enrique Lin Shiao, Tobias Wauer, Philipp Wortmann, Mark Bathe, and Hendrik Dietz. A primer to scaffolded DNA origami. *Nature methods*, 8(3):221–229, 2011.

[21] Arkadiusz Chworos, Isil Severcan, Alexey Y Koyfman, Patrick Weinkam, Emin Oroudjev, Helen G Hansma, and Luc Jaeger. Building programmable jigsaw puzzles with RNA. *Science*, 306(5704):2068–2072, 2004.

[22] Arkadiusz Chworos, Isil Severcan, Alexey Y Koyfman, Patrick Weinkam, Emin Oroudjev, Helen G Hansma, and Luc Jaeger. Building programmable jigsaw puzzles with RNA. *Science*, 306(5704):2068–2072, 2004.

[23] Camille J Delebecque, Ariel B Lindner, Pamela A Silver, and Faisal A Aldaye. Organization of intracellular reactions with rationally designed RNA assemblies. *Science*, 333(6041):470–474, 2011.

[24] Hendrik Dietz, Shawn M Douglas, and William M Shih. Folding DNA into twisted and curved nanoscale shapes. *Science*, 325(5941):725–730, 2009.

[25] R. M. Dirks, M. Lin, E. Winfree, and N. A. Pierce. Paradigms for computational nucleic acid design. *Nucleic Acids Research*, 32:1392–1403, 2004.

[26] Robert M Dirks, Milo Lin, Erik Winfree, and Niles A Pierce. Paradigms for computational nucleic acid design. *Nucleic Acids Research*, 32(4):1392–1403, 2004.

[27] Shawn M. Douglas, Ido Bachelet, and George M. Church. A logic-gated nanorobot for targeted transport of molecular payloads. *Science*, 335(6070):831–834, 2012.

[28] Shawn M. Douglas, Hendrik Dietz, Tim Liedl, Bjorn Hogberg, Franziska Graf, and William M. Shih. Self-assembly of DNA into nanoscale three-dimensional shapes. *Nature*, 459(7245):414–418, 05 2009.

[29] Shawn M Douglas, Adam H Marblestone, Surat Teerapittayanon, Alejandro Vazquez, George M Church, and William M Shih. Rapid prototyping of 3D DNA-origami shapes with caDNAno. *Nucleic acids research*, 37(15):5001–5006, 2009.

[30] E. Winfree. DNA design toolbox: http://www.dna.caltech.edu/dnadesign, 2004.

[31] Axel Ekani-Nkodo, Ashish Kumar, and Deborah Kuchnir Fygenson. Joining and scission in the self-assembly of nanotubes from DNA tiles. *Physical Review Letters*, 93:268301, 2004.

[32] Masayuki Endo, Yosuke Takeuchi, Tomoko Emura, Kumi Hidaka, and Hiroshi Sugiyama. Preparation of chemically modified RNA origami nanostructures. *Chemistry-A European Journal*, 20(47):15330–15333, 2014.

[33] Liping Feng, Sung Ha Park, John H Reif, and Hao Yan. A Two-State DNA Lattice Switched by DNA Nanoactuator. *Angewandte Chemie*, 115(36):4478–4482, 2003.

[34] Elisa Franco, Eike Friedrichs, Jongmin Kim, Ralf Jungmann, Richard Murray, Erik Winfree, and Friedrich C. Simmel. Timing molecular motion and production with a synthetic transcriptional clock. *Proceedings of the National Academy of Sciences*, 108(40):E784–E793, 2011.

[35] Elisa Franco, Giulia Giordano, Per-Ola Forsberg, and Richard M. Murray. Negative autoregulation matches production and demand in synthetic transcriptional networks. *ACS Synthetic Biology*, 2014.

[36] Elisa Franco, Giulia Giordano, Per-Ola Forsberg, and Richard M Murray. Negative autoregulation matches production and demand in synthetic transcriptional networks. *ACS Synthetic Biology*, 3(8):589–599, 2014.

[37] Tsu Fu and Nadrian Seeman. DNA double-crossover molecules. *Biochemistry*, 32(13):3211–3220, 1993.

[38] Cody Geary, Paul WK Rothemund, and Ebbe S Andersen. A single-stranded architecture for cotranscriptional folding of RNA nanostructures. *Science*, 345(6198):799–804, 2014.

[39] Chun Geng and Paul J Paukstelis. DNA crystals as vehicles for biocatalysis. *Journal of the American Chemical Society*, 136(22):7817–7820, 2014.

[40] Thomas Gerling, Klaus F Wagenbauer, Andrea M Neuner, and Hendrik Dietz. Dynamic DNA devices and assemblies formed by shape-complementary, non–base pairing 3D components. *Science*, 347(6229):1446–1452, 2015.

[41] Seth R. Goldman, Richard H. Ebright, and Bryce E. Nickels. Direct Detection of Abortive RNA Transcripts in Vivo. *Science*, 324(5929):927–928, 2009.

[42] Wade W Grabow and Luc Jaeger. RNA self-assembly and RNA nanotechnology. *Accounts of chemical research*, 47(6):1871–1880, 2014.

[43] Wade W Grabow, Paul Zakrevsky, Kirill A Afonin, Arkadiusz Chworos, Bruce A Shapiro, and Luc Jaeger. Self-assembling RNA nanorings based on RNAI/II inverse kissing complexes. *Nano letters*, 11(2):878–887, 2011.

[44] Peixuan Guo. The emerging field of RNA nanotechnology. *Nature nanotechnology*, 5(12):833–842, 2010.

[45] Peixuan Guo, Farzin Haque, Brent Hallahan, Randall Reif, and Hui Li. Uniqueness, advantages, challenges, solutions, and perspectives in therapeutics applying RNA nanotechnology. *Nucleic acid therapeutics*, 22(4):226–245, 2012.

[46] Dongran Han, Suchetan Pal, Jeanette Nangreave, Zhengtao Deng, Yan Liu, and Hao Yan. DNA origami with complex curvatures in three-dimensional space. *Science*, 332(6027):342–346, 2011.

[47] Dongran Han, Suchetan Pal, Yang Yang, Shuoxing Jiang, Jeanette Nangreave, Yan Liu, and Hao Yan. DNA gridiron nanostructures based on four-arm junctions. *Science*, 339(6126):1412–1415, 2013.

[48] Rizal F Hariadi, Mario Cale, and Sivaraj Sivaramakrishnan. Myosin lever arm directs collective motion on cellular actin network. *Proceedings of the National Academy of Sciences*, 111(11):4091–4096, 2014.

[49] Yu He, Yi Chen, Haipeng Liu, Alexander E Ribbe, and Chengde Mao. Self-assembly of hexagonal dna two-dimensional (2d) arrays. *Journal of the American Chemical Society*, 127(35):12202–12203, 2005.

[50] Yu He, Ye Tian, Yi Chen, Zhaoxiang Deng, Alexander E Ribbe, and Chengde Mao. Sequence symmetry as a tool for designing dna nanostructures. *Angewandte Chemie*, 117(41):6852–6854, 2005.

[51] Ivo L Hofacker. Vienna RNA secondary structure server. *Nucleic Acids Research*, 31(13):3429–3431, 2003.

[52] Lilian M Hsu, Nam V Vo, Caroline M Kane, and Michael J Chamberlin. In vitro studies of transcript initiation by Escherichia coli RNA polymerase. 1. RNA chain initiation, abortive initiation, and promoter escape at three bacteriophage promoters. *Biochemistry*, 42(13):3777–3786, 2003.

[53] Ryosuke Iinuma, Yonggang Ke, Ralf Jungmann, Thomas Schlichthaerle, Johannes B Woehrstein, and Peng Yin. Polyhedra self-assembled from DNA tripods and characterized with 3D DNA-PAINT. *science*, 344(6179):65–69, 2014.

[54] Luc Jaeger, Eric Westhof, and Neocles B Leontis. TectoRNA: modular assembly units for the construction of RNA nano-objects. *Nucleic acids research*, 29(2):455–463, 2001.

[55] Qiao Jiang, Chen Song, Jeanette Nangreave, Xiaowei Liu, Lin Lin, Dengli Qiu, Zhen-Gang Wang, Guozhang Zou, Xingjie Liang, Hao Yan, et al. Dna origami as a carrier for circumvention of drug resistance. *Journal of the American Chemical Society*, 134(32):13396–13403, 2012.

[56] Fabrice Jossinet, Thomas E Ludwig, and Eric Westhof. Assemble: an interactive graphical tool to analyze and build RNA architectures at the 2D and 3D levels. *Bioinformatics*, 26(16):2057–2059, 2010.

[57] DL Kaiser, S Standridge, L Friedersdorf, CL Geraci, F Kronz, MA Meador, and DM Stepp. National nanotechnology initiative strategic plan. *National science and technology council, Washington DC*, 2014.

[58] Ulla Kaukinen, Sari Lyytikäinen, Satu Mikkola, and Harri Lönnberg. The reactivity of phosphodiester bonds within linear single-stranded oligoribonucleotides is strongly dependent on the base sequence. *Nucleic Acids Research*, 30(2):468–474, 2002.

[59] Yonggang Ke, Luvena L Ong, William M Shih, and Peng Yin. Three-dimensional structures self-assembled from DNA bricks. *Science*, 338(6111):1177–1183, 2012.

[60] Yonggang Ke, Luvena L. Ong, Wei Sun, Jie Song, Mingdong Dong, William M. Shih, and Peng Yin. DNA brick crystals with prescribed depths. *Nature Chemistry*, 6(11):994–1002, 11 2014.

[61] Anthony D Keefe, Supriya Pai, and Andrew Ellington. Aptamers as therapeutics. *Nature Reviews Drug Discovery*, 9(7):537–550, 2010.

[62] Emil F Khisamutdinov, Hui Li, Daniel L Jasinski, Jiao Chen, Jian Fu, and Peixuan Guo. Enhancing immunomodulation on innate immunity by shape transition among rna triangle, square and pentagon nanovehicles. *Nucleic acids research*, 42(15):9996–10004, 2014.

[63] J. Kim, K. S. White, and E. Winfree. Construction of an *in vitro* bistable circuit from synthetic transcriptional switches. *Molecular Systems Biology*, 1:68, 2006.

[64] Jørgen Kjems, Elena Ferapontova, and Kurt V Gothelf. *Nucleic Acid Nanotechnology*. Springer, 2014.

[65] Seung Hyeon Ko, Min Su, Chuan Zhang, Alexander E Ribbe, Wen Jiang, and Chengde Mao. Synergistic self-assembly of RNA and DNA molecules. *Nature chemistry*, 2(12):1050–1055, 2010.

[66] SeungHyeon Ko, Haipeng Liu, Yi Chen, and Chengde Mao. Dna nanotubes as combinatorial vehicles for cellular delivery. *Biomacromolecules*, 9(11):3039–3043, 2008.

[67] Samet Kocabey, Hanna Meinl, Iain S MacPherson, Valentina Cassinelli, Antonio Manetto, Simon Rothenfusser, Tim Liedl, and Felix S Lichtenegger. Cellular uptake of tile-assembled dna nanotubes. *Nanomaterials*, 5(1):47–60, 2014.

[68] Alexey Y Koyfman, Gary Braun, Sergei Magonov, Arkadiusz Chworos, Norbert O Reich, and Luc Jaeger. Controlled spacing of cationic gold nanoparticles by nanocrown rna. *Journal of the American Chemical Society*, 127(34):11886–11887, 2005.

[69] Alexey Y Koyfman, Gary B Braun, and Norbert O Reich. Cell-targeted self-assembled dna nanostructures. *Journal of the American Chemical Society*, 131(40):14237–14239, 2009.

[70] Alexey Y Koyfman, Sergei N Magonov, and Norbert O Reich. Self-assembly of dna arrays into multilayer stacks. *Langmuir*, 25(2):1091–1096, 2008.

[71] A. Kuzyk, R. Schreiber, Z. Fan, G. Pardatscher, E. M. Roller, A. Hogele, F. C. Simmel, A. O. Govorov, and T. Liedl. DNA-based self-assembly of chiral plasmonic nanostructures with tailored optical response. *Nature*, 483:311–314, 2012.

[72] Hyukjin Lee, Abigail KR Lytton-Jean, Yi Chen, Kevin T Love, Angela I Park, Emmanouil D Karagiannis, Alfica Sehgal, William Querbes, Christopher S Zurenko,

Muthusamy Jayaraman, et al. Molecularly self-assembled nucleic acid nanoparticles for targeted in vivo sirna delivery. *Nature nanotechnology*, 7(6):389, 2012.

[73] Jong Bum Lee, Jinkee Hong, Daniel K Bonner, Zhiyong Poon, and Paula T Hammond. Self-assembled rna interference microsponges for efficient sirna delivery. *Nature materials*, 11(4):316, 2012.

[74] Yingfu Li and Ronald R Breaker. Kinetics of RNA degradation by specific base catalysis of transesterification involving the 2'-hydroxyl group. *Journal of the American Chemical Society*, 121(23):5364–5372, 1999.

[75] Lijun Liang, Jia-Wei Shen, and Qi Wang. Molecular dynamics study on dna nanotubes as drug delivery vehicle for anticancer drugs. *Colloids and Surfaces B: Biointerfaces*, 153:168–173, 2017.

[76] Haipeng Liu, Yi Chen, Yu He, Alexander E Ribbe, and Chengde Mao. Approaching the limit: can one dna oligonucleotide assemble into large nanostructures? *Angewandte Chemie International Edition*, 45(12):1942–1945, 2006.

[77] Wenyan Liu, Hong Zhong, Risheng Wang, and Nadrian C Seeman. Crystalline two-dimensional DNA-origami arrays. *Angewandte Chemie*, 123(1):278–281, 2011.

[78] Pik Kwan Lo, Pierre Karam, Faisal A. Aldaye, Christopher K. McLaughlin, Graham D. Hamblin, Gonzalo Cosa, and Hanadi F. Sleiman. Loading and selective release of cargo in DNA nanotubes with longitudinal variation. *Nature Chemistry*, 2:319–328, 2010.

[79] Kyle Lund, Anthony J. Manzo, Nadine Dabby, Nicole Michelotti, Alexander Johnson-Buck, Jeanette Nangreave, Steven Taylor, Renjun Pei, Milan N. Stojanovic, Nils G. Walter, Erik Winfree, and Hao Yan. Molecular robots guided by prescriptive landscapes. *Nature*, 465(7295):206–210, 2010.

[80] Chengde Mao, Thomas H LaBean, John H Reif, and Nadrian C Seeman. Logical computation using algorithmic self-assembly of DNA triple-crossover molecules. *Nature*, 407(6803):493–496, 2000.

[81] N. R. Markham and M. Zuker. UNAFold software for nucleic acid folding and hybridization. *Methods in Molecular Biology*, 453(1):3–31, 2008.

[82] Craig T Martin, Daniel K Muller, and Joseph E Coleman. Processivity in early stages of transcription by T7 RNA polymerase. *Biochemistry*, 27(11):3966–3974, 1988.

[83] Hugo M Martinez, Jacob V Maizel Jr, and Bruce A Shapiro. RNA2D3D: a program for generating, viewing, and comparing 3-dimensional models of RNA. *Journal of Biomolecular Structure and Dynamics*, 25(6):669–683, 2008.

[84] J F Milligan, D R Groebe, G W Witherell, and O C Uhlenbeck. Oligoribonucleotide synthesis using T7 RNA polymerase and synthetic DNA templates. *Nucleic Acids Research*, 15(21):87838798, 1987.

[85] James C Mitchell, J Robin Harris, Jonathan Malo, Jonathan Bath, and Andrew J Turberfield. Self-assembly of chiral DNA nanotubes. *Journal of the American Chemical Society*, 126(50):16342–16343, 2004.

[86] Abdul M Mohammed and Rebecca Schulman. Directing self-assembly of DNA nanotubes using programmable seeds. *Nano letters*, 13(9):4006–4013, 2013.

[87] Rebecca K Montange and Robert T Batey. Riboswitches: emerging themes in RNA structure and function. *Annu. Rev. Biophys.*, 37:117–133, 2008.

[88] Cameron Myhrvold, Mingjie Dai, Pamela A Silver, and Peng Yin. Isothermal self-assembly of complex DNA structures under diverse and biocompatible conditions. *Nano letters*, 13(9):4242–4248, 2013.

[89] Lorena Nasalean, Stéphanie Baudrey, Neocles B Leontis, and Luc Jaeger. Controlling RNA self-assembly to form filaments. *Nucleic acids research*, 34(5):1381–1392, 2006.

[90] Anders Hauge Okholm, David Schaffert, and Jørgen Kjems. Towards defined dna and rna delivery vehicles using nucleic acid nanotechnology. In *Chemical Biology of Nucleic Acids*, pages 325–345. Springer, 2014.

[91] Sung Ha Park, Robert Barish, Hanying Li, John H Reif, Gleb Finkelstein, Hao Yan, and Thomas H LaBean. Three-helix bundle DNA tiles self-assemble into 2D lattice or 1D templates for silver nanowires. *Nano letters*, 5(4):693–696, 2005.

[92] Paul J Paukstelis, Jacek Nowakowski, Jens J Birktoft, and Nadrian C Seeman. Crystal structure of a continuous three-dimensional DNA lattice. *Chemistry & biology*, 11(8):1119–1126, 2004.

[93] Eric F Pettersen, Thomas D Goddard, Conrad C Huang, Gregory S Couch, Daniel M Greenblatt, Elaine C Meng, and Thomas E Ferrin. UCSF Chimeraa visualization system for exploratory research and analysis. *Journal of computational chemistry*, 25(13):1605–1612, 2004.

[94] Ekaterina Protozanova, Peter Yakovchuk, and Maxim D Frank-Kamenetskii. Stacked–unstacked equilibrium at the nick site of DNA. *Journal of molecular biology*, 342(3):775–785, 2004.

[95] PengFei Qian, Sangjae Seo, Junghoon Kim, Seungjae Kim, Byeong Soo Lim, Wing Kam Liu, Bum Joon Kim, Thomas Henry LaBean, Sung Ha Park, and Moon Ki Kim. DNA nanotube formation based on normal mode analysis. *Nanotechnology*, 23(10):105704, 2012.

[96] Shannon Reagan-Shaw and Nihal Ahmad. Silencing of polo-like kinase (plk) 1 via sirna causes induction of apoptosis and impairment of mitosis machinery in human prostate cancer cells: implications for the treatment of prostate cancer. *The FASEB journal*, 19(6):611–613, 2005.

[97] Scott D Rose, Dong-Ho Kim, Mohammed Amarzguioui, Jeremy D Heidel, Michael A Collingwood, Mark E Davis, John J Rossi, and Mark A Behlke. Functional polarity is introduced by dicer processing of short substrate rnas. *Nucleic acids research*, 33(13):4140–4156, 2005.

[98] P. W. K. Rothemund. Folding DNA to create nanoscale shapes and patterns. *Nature*, 440:297–302, 2006.

[99] Paul W. K. Rothemund, Axel Ekani-Nkodo, Nick Papadakis, Ashish Kumar, Deborah Kuchnir Fygenson, and Erik Winfree. Design and characterization of programmable DNA nanotubes. *Journal of the American Chemical Society*, 126(50):16344–16352, 2004.

[100] Paul WK Rothemund, Nick Papadakis, and Erik Winfree. Algorithmic self-assembly of DNA Sierpinski triangles. *PLoS biology*, 2(12):e424, 2004.

[101] Gairik Sachdeva, Abhishek Garg, David Godding, Jeffrey C Way, and Pamela A Silver. In vivo co-localization of enzymes on RNA scaffolds increases metabolic production in a geometrically dependent manner. *Nucleic acids research*, 42(14):9493–9503, 2014.

[102] J. SantaLucia. A unified view of polymer, dumbbell, and oligonucleotide DNA nearest-neighbor thermodynamics. *Proceedings of the National Academy of Sciences*, 95(4):1460–1465, 1998.

[103] Rebecca Schulman and Erik Winfree. Synthesis of crystals with a programmable kinetic barrier to nucleation. *Proceedings of the National Academy of Sciences*, 104(39):15236–15241, 2007.

[104] Nadrian C Seeman. Nucleic acid junctions and lattices. *Journal of theoretical biology*, 99(2):237–247, 1982.

[105] Nadrian C Seeman. De novo design of sequences for nucleic acid structural engineering. *Journal of biomolecular structure and dynamics*, 8(3):573–581, 1990.

[106] Nadrian C Seeman. DNA nanotechnology: novel DNA constructions. *Annual review of biophysics and biomolecular structure*, 27(1):225–248, 1998.

[107] Sabine Sellner, Samet Kocabey, Katharina Nekolla, Fritz Krombach, Tim Liedl, and Markus Rehberg. Dna nanotubes as intracellular delivery vehicles in vivo. *Biomaterials*, 53:453–463, 2015.

[108] Isil Severcan, Cody Geary, Arkadiusz Chworos, Neil Voss, Erica Jacovetty, and Luc Jaeger. A polyhedron made of tRNAs. *Nature chemistry*, 2(9):772–779, 2010.

[109] Bruce A Shapiro, Yaroslava G Yingling, Wojciech Kasprzak, and Eckart Bindewald. Bridging the gap in RNA structure prediction. *Current opinion in structural biology*, 17(2):157–165, 2007.

[110] Ashwani Sharma, Farzin Haque, Fengmei Pi, Lyudmila S Shlyakhtenko, B Mark Evers, and Peixuan Guo. Controllable self-assembly of rna dendrimers. *Nanomedicine: Nanotechnology, Biology and Medicine*, 12(3):835–844, 2016.

[111] Jaswinder Sharma, Rahul Chhabra, Anchi Cheng, Jonathan Brownell, Yan Liu, and Hao Yan. Control of self-assembly of DNA tubules through integration of gold nanoparticles. *Science*, 323(5910):112–116, 2009.

[112] William B Sherman and Nadrian C Seeman. A precisely controlled DNA biped walking device. *Nano Letters*, 4(7):1203–1207, 2004.

[113] Dan Shu, Yi Shu, Farzin Haque, Sherine Abdelmawla, and Peixuan Guo. Thermodynamically stable RNA three-way junction for constructing multifunctional nanoparticles for delivery of therapeutics. *Nature nanotechnology*, 6(10):658–667, 2011.

[114] Jaimie Marie Stewart and Elisa Franco. Self-assembly of large rna structures: learning from dna nanotechnology. *DNA and RNA Nanotechnology*, 2(1):23–35, 2015.

[115] Jaimie Marie Stewart, Hari KK Subramanian, and Elisa Franco. Self-assembly of multi-stranded rna motifs into lattices and tubular structures. *Nucleic acids research*, 45(9):5449–5457, 2017.

[116] Jaimie Marie Stewart, Mathias Viard, Hari KK Subramanian, Brandon K Roark, Kirill A Afonin, and Elisa Franco. Programmable rna microstructures for coordinated delivery of sirnas. *Nanoscale*, 2016.

[117] Accelrys Discovery Studio. 1.7, accelrys software inc., san diego, ca, usa. 2006.

[118] C. Sturk, E. Franco, and R. M. Murray. Tuning a synthetic in vitro oscillator using control-theoretic tools. In *Proceedings of the IEEE Conference on Decision and Control*, 2010.

[119] Sunaina Surana, Avinash R Shenoy, and Yamuna Krishnan. Designing DNA nanodevices for compatibility with the immune system of higher organisms. *Nature nanotechnology*, 10(9):741–747, 2015.

[120] Francisco J Triana-Alonso, Marylena Dabrowski, Jörg Wadzack, and Knud H Nierhaus. Self-coded 3'-extension of run-off transcripts produces aberrant products during in vitro transcription with T7 RNA polymerase. *Journal of Biological Chemistry*, 270(11):6298–6307, 1995.

[121] Nam V Vo, Lilian M Hsu, Caroline M Kane, and Michael J Chamberlin. In vitro studies of transcript initiation by escherichia coli rna polymerase. 3. influences of individual dna elements within the promoter recognition region on abortive initiation and promoter escape. *Biochemistry*, 42(13):3798–3811, 2003.

[122] Niels V. Voigt, Thomas Torring, Alexandru Rotaru, Mikkel F. Jacobsen, Jens B. Ravnsbaek, Ramesh Subramani, Wael Mamdouh, Jorgen Kjems, Andriy Mokhir, Flemming Besenbacher, and Kurt Vesterager Gothelf. Single-molecule chemical reactions on DNA origami. *Nature Nanotechnology*, 5(3):200–203, 03 2010.

[123] Bin Wang. *RNA Nanotechnology*. CRC Press, 2014.

[124] Pengfei Wang, Seung Hyeon Ko, Cheng Tian, Chenhui Hao, and Chengde Mao. RNA–DNA hybrid origami: folding of a long RNA single strand into complex nanostructures using short DNA helper strands. *Chemical Communications*, 49(48):5462–5464, 2013.

[125] Bryan Wei, Mingjie Dai, and Peng Yin. Complex shapes self-assembled from single-stranded DNA tiles. *Nature*, 485(7400):623–626, 2012.

[126] Sean Williams, Kyle Lund, Chenxiang Lin, Peter Wonka, Stuart Lindsay, and Hao Yan. Tiamat: a three-dimensional editing tool for complex DNA structures. In *DNA Computing*, pages 90–101. Springer, 2009.

[127] Erik Winfree, Furong Liu, Lisa A Wenzler, and Nadrian C Seeman. Design and self-assembly of two-dimensional DNA crystals. *Nature*, 394(6693):539–544, 1998.

[128] Sungwook Woo and Paul W. K. Rothemund. Programmable molecular recognition based on the geometry of DNA nanostructures. *Nature Chemistry*, 3:620–627, 2011.

[129] Hao Yan, Sung Ha Park, Gleb Finkelstein, John H. Reif, and Thomas H. LaBean. DNA-templated self-assembly of protein arrays and highly conductive nanowires. *Science*, 301(5641):1882–1884, 2003.

[130] Peng Yin, Rizal F. Hariadi, Sudheer Sahu, Harry M. T. Choi, Sung Ha Park, Thomas H. LaBean, and John H. Reif. Programming DNA tube circumferences. *Science*, 321(5890):824–826, 2008.

[131] Yaroslava G Yingling and Bruce A Shapiro. Computational design of an rna hexagonal nanoring and an rna nanotube. *Nano letters*, 7(8):2328–2334, 2007.

[132] Jinwen Yu, Zhiyu Liu, Wen Jiang, Guansong Wang, and Chengde Mao. De novo design of an RNA tile that self-assembles into a homo-octameric nanoprism. *Nature communications*, 6, 2015.

[133] Bernard Yurke and Allen P. Mills. Using DNA to power nanostructures. *Genetic Programming and Evolvable Machines*, 4:111–122, 2003.

[134] J. N. Zadeh, C. D. Steenberg, J. S. Bois, B. R. Wolfe, M. B. Pierce, A. R. Khan, R. M. Dirks, and N. A. Pierce. NUPACK: analysis of nucleic acid systems. *Journal of Computational Chemistry*, 32:170–173, 2011.

[135] David Yu Zhang, Rizal F Hariadi, Harry MT Choi, and Erik Winfree. Integrating DNA strand-displacement circuitry with DNA tile self-assembly. *Nature communications*, 4, 2013.

[136] David Yu Zhang and Georg Seelig. Dynamic DNA nanotechnology using strand-displacement reactions. *Nature Chemistry*, 3(2):103–113, 2011.

[137] Fei Zhang, Shuoxing Jiang, Siyu Wu, Yulin Li, Chengde Mao, Yan Liu, and Hao Yan. Complex wireframe DNA origami nanostructures with multi-arm junction vertices. *Nat Nano*, pages –, 07 2015.

[138] Fei Zhang, Jeanette Nangreave, Yan Liu, and Hao Yan. Reconfigurable DNA origami to generate quasifractal patterns. *Nano letters*, 12(6):3290–3295, 2012.

[139] Fei Zhang, Jeanette Nangreave, Yan Liu, and Hao Yan. Structural DNA nanotechnology: State of the art and future perspective. *Journal of the American Chemical Society*, 136(32):11198–11211, 2014.

[140] Zhao Zhao, Yan Liu, and Hao Yan. Organizing DNA origami tiles into larger structures using preformed scaffold frames. *Nano letters*, 11(7):2997–3002, 2011.

[141] Jianping Zheng, Jens J Birktoft, Yi Chen, Tong Wang, Ruojie Sha, Pamela E Constantinou, Stephan L Ginell, Chengde Mao, and Nadrian C Seeman. From molecular to macroscopic via the rational design of a self-assembled 3D DNA crystal. *Nature*, 461(7260):74–77, 2009.

Chapter 6

Supplementary Information for Self-assembly of multi-stranded RNA motifs into lattices and tubular structures

6.1 Sequences

PAGE purified DNA sequences were ordered from IDT DNA (Coralville, IA, USA). Templates include 3 base "sealing" domains (5' end of non-template strand) to prevent breathing at the promoter site. All templates include the T7 promoter sequence. The +1 to +6 promoter region (transcription start site) was modified relative to the generally recommended sequence (GGGAGA) [84], to avoid altering or constraining the sequence

content of RNA tiles.

RNA sequences for tile D1R were identified by converting to RNA the (44+6) tile design from Ko et al. [65], Supplementary Information File; variants D1C and D1L were obtained by simply changing the nick position in strand Sb. RNA sequences for tile D2R were designed in-house using the DNA design toolbox [30, 26]; each strand was designed to start with GG on the 3' end, to ensure good transcription yield.

6.1.1 DNA templates

Tiles with sticky ends

DNA sequences for design 1 right nick position (D1R)

Sa1 5'- TTC TAA TAC GAC TCA CTA TAG GTG CGA CTA TGC AAC CTG CCT GGC AAG ACC TAC GAT GGA CAC GGT AAC G -3' / 5'- CGT TAC CGT GTC CAT CGT AGG TCT TGC CAG GCA GGT TGC ATA GTC GCA CCT ATA GTG AGT CGT ATT AGA A -3'

SbR1 5' - TTC TAA TAC GAC TCA CTA TAG TCT TGC CAG GCA CCA TCG TAG GTC TTG CCA GGC ACC ATC GTA G -3' / 5'- CTA CGA TGG TGC CTG GCA AGA CCT ACG ATG GTG CCT GGC AAG ACT ATA GTG AGT CGT ATT AGA A -3'

Sc1 5' -TTC TAA TAC GAC TCA CTA TAG CAC CCG TTA CCG TGT GGT TGC ATA GTC -3' / 5'- GAC TAT GCA ACC ACA CGG TAA CGG GTG CTA TAG TGA GTC GTA TTA GAA -3'

DNA sequences for design 1 right nick position (D1RE), Sa1E strand with 5' end 5 nt overhang

Sa1E 5' -TTC TAA TAC GAC TCA CTA TAG AAC UGG TGC GAC TAT GCA ACC

TGC CTG GCA AGA CCT ACG ATG GAC ACG GTA ACG -3' / 5'- CGT TAC CGT GTC CAT CGT AGG TCT TGC CAG GCA GGT TGC ATA GTC GCA CCA GTT CTA TAG TGA GTC GTA TTA GAA -3'

DNA sequences for design 1 center nick position (D1C)

Sa1 5'- TTC TAA TAC GAC TCA CTA TAG GTG CGA CTA TGC AAC CTG CCT GGC AAG ACC TAC GAT GGA CAC GGT AAC G -3' / 5'- CGT TAC CGT GTC CAT CGT AGG TCT TGC CAG GCA GGT TGC ATA GTC GCA CCT ATA GTG AGT CGT ATT AGA A -3'

SbC1 5' -TTC TAA TAC GAC TCA CTA TAC TTG CCA GGC ACC ATC GTA GGT CTT GCC AGG CAC CAT CGT AGG T -3' / 5'- ACC TAC GAT GGT GCC TGG CAA GAC CTA CGA TGG TGC CTG GCA AGT ATA GTG AGT CGT ATT AGA A -3'

Sc1 5' -TTC TAA TAC GAC TCA CTA TAG CAC CCG TTA CCG TGT GGT TGC ATA GTC -3' / 5'- GAC TAT GCA ACC ACA CGG TAA CGG GTG CTA TAG TGA GTC GTA TTA GAA -3'

DNA sequences for design 1 left nick position (D1L)

Sa1 5'- TTC TAA TAC GAC TCA CTA TAG GTG CGA CTA TGC AAC CTG CCT GGC AAG ACC TAC GAT GGA CAC GGT AAC G -3' / 5'- CGT TAC CGT GTC CAT CGT AGG TCT TGC CAG GCA GGT TGC ATA GTC GCA CCT ATA GTG AGT CGT ATT AGA A -3'

SbL1 5' -TTC TAA TAC GAC TCA CTA TAT GCC AGG CAC CAT CGT AGG TCT TGC CAG GCA CCA TCG TAG GTC T -3' / 5'- AGA CCT ACG ATG GTG CCT GGC AAG ACC TAC GAT GGT GCC TGG CAT ATA GTG AGT CGT ATT AGA -3'

Sc1 5’ -TTC TAA TAC GAC TCA CTA TAG CAC CCG TTA CCG TGT GGT TGC ATA GTC -3’ / 5’- GAC TAT GCA ACC ACA CGG TAA CGG GTG CTA TAG TGA GTC GTA TTA GAA -3’

DNA sequences for design 2 right nick position (D2R)

Sa2 5’- GTT GTA ATA CGA CTC ACT ATA GGT CCT ATA CTT CAA CTG TTA ATT TCT GCC GCT TCT TTA CAT TCT ATC TT -3’ / 5’- AAG ATA GAA TGT AAA GAA GCG GCA GAA ATT AAC AGT TGA AGT ATA GGA CCT ATA GTG AGT CGT ATT ACA AC -3’

SbR2 5’- GTT GTA ATA CGA CTC ACT ATA GGC AGA AAT TAA CTA AAG AAG CGG CAG AAA TTA ACT AAA GAA GC -3’ / 5’- GCT TCT TTA GTT AAT TTC TGC CGC TTC TTT AGT TAA TTT CTG CCT ATA GTG AGT CGT ATT ACA AC -3’

Sc2 5’- GTT GTA ATA CGA CTC ACT ATA GGA CCA AGA TAG AAT GAG TTG AAG TAT A -3’ / 5’- TAT ACT TCA ACT CAT TCT ATC TTG GTC CTA TAG TGA GTC GTA TTA CAA C -3’

DNA sequences for design 2 center nick position (D2C)

Sa2 5’- GTT GTA ATA CGA CTC ACT ATA GGT CCT ATA CTT CAA CTG TTA ATT TCT GCC GCT TCT TTA CAT TCT ATC TT -3’ / 5’- AAG ATA GAA TGT AAA GAA GCG GCA GAA ATT AAC AGT TGA AGT ATA GGA CCT ATA GTG AGT CGT ATT ACA AC -3’

SbC2 5’- GTT GTA ATA CGA CTC ACT ATA CAG AAA TTA ACT AAA GAA GCG GCA GAA ATT AAC TAA AGA AGC GG -3’ / 5’- CCG CTT CTT TAG TTA ATT

TCT GCC GCT TCT TTA GTT AAT TTC TGT ATA GTG AGT CGT ATT ACA AC -3'

Sc2 5'- GTT GTA ATA CGA CTC ACT ATA GGA CCA AGA TAG AAT GAG TTG AAG TAT A -3' / 5'- TAT ACT TCA ACT CAT TCT ATC TTG GTC CTA TAG TGA GTC GTA TTA CAA C -3'

DNA sequences for design 2 left nick position (D2L)

Sa2 5'- GTT GTA ATA CGA CTC ACT ATA GGT CCT ATA CTT CAA CTG TTA ATT TCT GCC GCT TCT TTA CAT TCT ATC TT -3' / 5'- AAG ATA GAA TGT AAA GAA GCG GCA GAA ATT AAC AGT TGA AGT ATA GGA CCT ATA GTG AGT CGT ATT ACA AC -3'

SbL2 5'- GTT GTA ATA CGA CTC ACT ATA GAA ATT AAC TAA AGA AGC GGC AGA AAT TAA CTA AAG AAG CGG CA -3' / 5'- TGC CGC TTC TTT AGT TAA TTT CTG CCG CTT CTT TAG TTA ATT TCT ATA GTG AGT CGT ATT ACA AC -3'

Sc2 5'- GTT GTA ATA CGA CTC ACT ATA GGA CCA AGA TAG AAT GAG TTG AAG TAT A -3' / 5'- TAT ACT TCA ACT CAT TCT ATC TTG GTC CTA TAG TGA GTC GTA TTA CAA C -3'

Tiles without sticky ends

DNA sequences for design 1 right nick position (D1R)

Sa1 5'- TTC TAA TAC GAC TCA CTA TAG ACT ATG CAA CCT GCC TGG CAA GAC CTA CGA TGG ACA CGG TAA CG -3' / 5'- CGT TAC CGT GTC CAT CGT AGG TCT TGC CAG GCA GGT TGC ATA GTC TAT AGT GAG TCG TAT TAG AA

-3’

SbR1 5’- TTC TAA TAC GAC TCA CTA TAG TCT TGC CAG GCA CCA TCG TAG GTC TTG CCA GGC ACC ATC GTA G -3’ / 5’- CTA CGA TGG TGC CTG GCA AGA CCT ACG ATG GTG CCT GGC AAG ACT ATA GTG AGT CGT ATT AGA A -3’

Sc1 5’- TTC TAA TAC GAC TCA CTA TAC GTT ACC GTG TGG TTG CAT AGT C -3’ / 5’- GAC TAT GCA ACC ACA CGG TAA CGT ATA GTG AGT CGT ATT AGA A -3’

DNA sequences for design 1 center nick position (D1C)

Sa1 5’- TTC TAA TAC GAC TCA CTA TAG ACT ATG CAA CCT GCC TGG CAA GAC CTA CGA TGG ACA CGG TAA CG -3’ / 5’- CGT TAC CGT GTC CAT CGT AGG TCT TGC CAG GCA GGT TGC ATA GTC TAT AGT GAG TCG TAT TAG AA -3’

SbC1 5’- TTC TAA TAC GAC TCA CTA TAC TTG CCA GGC ACC ATC GTA GGT CTT GCC AGG CAC CAT CGT AGG T -3’ / 5’- ACC TAC GAT GGT GCC TGG CAA GAC CTA CGA TGG TGC CTG GCA AGT ATA GTG AGT CGT ATT AGA A -3’

Sc1 5’- TTC TAA TAC GAC TCA CTA TAC GTT ACC GTG TGG TTG CAT AGT C -3’ / 5’- GAC TAT GCA ACC ACA CGG TAA CGT ATA GTG AGT CGT ATT AGA A -3’

DNA sequences for design 1 left nick position (D1L)

Sa1 5’- TTC TAA TAC GAC TCA CTA TAG ACT ATG CAA CCT GCC TGG CAA GAC CTA CGA TGG ACA CGG TAA CG -3’ / 5’- CGT TAC CGT GTC CAT CGT AGG TCT TGC CAG GCA GGT TGC ATA GTC TAT AGT GAG TCG TAT TAG AA

-3’

SbL1 5’- TTC TAA TAC GAC TCA CTA TAT GCC AGG CAC CAT CGT AGG TCT TGC CAG GCA CCA TCG TAG GTC T -3’ / 5’- AGA CCT ACG ATG GTG CCT GGC AAG ACC TAC GAT GGT GCC TGG CAT ATA GTG AGT CGT ATT AGA -3’

Sc1 5’- TTC TAA TAC GAC TCA CTA TAC GTT ACC GTG TGG TTG CAT AGT C -3’ / 5’- GAC TAT GCA ACC ACA CGG TAA CGT ATA GTG AGT CGT ATT AGA A -3’

DNA sequences for design 2 right nick position (D2R)

Sa2 5’- GTT GTA ATA CGA CTC ACT ATA TAT ACT TCA ACT GTT AAT TTC TGC CGC TTC TTT ACA TTC TAT CTT -3’ / 5’- AAG ATA GAA TGT AAA GAA GCG GCA GAA ATT AAC AGT TGA AGT ATA TAT AGT GAG TCG TAT TAC AAC -3’

SbR2 5’- GTT GTA ATA CGA CTC ACT ATA GGC AGA AAT TAA CTA AAG AAG CGG CAG AAA TTA ACT AAA GAA GC -3’ / 5’- GCT TCT TTA GTT AAT TTC TGC CGC TTC TTT AGT TAA TTT CTG CCT ATA GTG AGT CGT ATT ACA AC -3’

Sc2 5’- GTT GTA ATA CGA CTC ACT ATA AAG ATA GAA TGA GTT GAA GTA TA -3’ / 5’- TAT ACT TCA ACT CAT TCT ATC TTT ATA GTG AGT CGT ATT ACA AC -3’

DNA sequences for design 2 center nick position (D2C)

Sa2 5’- GTT GTA ATA CGA CTC ACT ATA TAT ACT TCA ACT GTT AAT TTC TGC CGC TTC TTT ACA TTC TAT CTT -3’ / 5’- AAG ATA GAA TGT AAA GAA

GCG GCA GAA ATT AAC AGT TGA AGT ATA TAT AGT GAG TCG TAT TAC AAC -3'

SbC2 5'- GTT GTA ATA CGA CTC ACT ATA CAG AAA TTA ACT AAA GAA GCG GCA GAA ATT AAC TAA AGA AGC GG -3' / 5'- CCG CTT CTT TAG TTA ATT TCT GCC GCT TCT TTA GTT AAT TTC TGT ATA GTG AGT CGT ATT ACA AC -3'

Sc2 5'- GTT GTA ATA CGA CTC ACT ATA AAG ATA GAA TGA GTT GAA GTA TA -3' / 5'- TAT ACT TCA ACT CAT TCT ATC TTT ATA GTG AGT CGT ATT ACA AC -3'

DNA sequences for design 2 left nick position (D2L)

Sa2 5'- GTT GTA ATA CGA CTC ACT ATA TAT ACT TCA ACT GTT AAT TTC TGC CGC TTC TTT ACA TTC TAT CTT -3' / 5'- AAG ATA GAA TGT AAA GAA GCG GCA GAA ATT AAC AGT TGA AGT ATA TAT AGT GAG TCG TAT TAC AAC -3'

SbL2 5'- GTT GTA ATA CGA CTC ACT ATA GAA ATT AAC TAA AGA AGC GGC AGA AAT TAA CTA AAG AAG CGG CA -3' / 5'- TGC CGC TTC TTT AGT TAA TTT CTG CCG CTT CTT TAG TTA ATT TCT ATA GTG AGT CGT ATT ACA AC -3'

Sc2 5'- GTT GTA ATA CGA CTC ACT ATA AAG ATA GAA TGA GTT GAA GTA TA -3' / 5'- TAT ACT TCA ACT CAT TCT ATC TTT ATA GTG AGT CGT ATT ACA AC -3'

6.1.2 RNA sequences

RNA sequences for design 1 right nick position (D1R)

Sa1 5'- GGU GCG ACU AUG CAA CCU GC CUG GCA AGA CCU ACG AUG GAC ACG GUA ACG -3'

SbR1 5'- GUC UUG CCA GGC ACC AUC GUA GGU CUU GCC AGG CAC CAU CGU AG -3'

Sc1 5'- GCA CCC GUU ACC GUG UGG UUG CAU AGU C -3'

RNA sequences for design 1, right nick position that includes 5 end, 5 nt overhang on Sa1 (D1RE)

Sa1E 5'- GAA CUG GTG CGA CTA TGC AAC CTG CCT GGC AAG ACC TAC GAT GGA CAC GGT AAC G -3'

SbR1 5'- GUC UUG CCA GGC ACC AUC GUA GGU CUU GCC AGG CAC CAU CGU AG -3'

Sc1 5'- GCA CCC GUU ACC GUG UGG UUG CAU AGU C -3'

RNA sequences for design 1 center nick position (D1C)

Sa1 5'- GGU GCG ACU AUG CAA CCU GC CUG GCA AGA CCU ACG AUG GAC ACG GUA ACG -3'

SbC1 5'- CUU GCC AGG CAC CAU CGU AGG UCU UGC CAG GCA CCA UCG UAG GU -3'

Sc1 5'- GCA CCC GUU ACC GUG UGG UUG CAU AGU C -3'

RNA sequences for design 1 left nick position (D1L)

Sa1 5'- GGU GCG ACU AUG CAA CCU GC CUG GCA AGA CCU ACG AUG GAC

ACG GUA ACG -3'

SbL1 5'- UGC CAG GCA CCA UCG UAG GUC UUG CCA GGC ACC AUC GUA GGU CU -3'

Sc1 5'- GCA CCC GUU ACC GUG UGG UUG CAU AGU C -3'

RNA sequences for design 2 right nick position (D2R)

Sa2 5'- GGU CCU AUA CUU CAA CUG UUA AUU UCU GCC GCU UCU UUA CAU UCU AUC UU -3'

SbR2 5'- GGC AGA AAU UAA CUA AAG AAG CGG CAG AAA UUA ACU AAA GAA GC -3'

Sc2 5'- GGA CCA AGA UAG AAU GAG UUG AAG UAU A -3'

RNA sequences for design 2 center nick position (D2C)

Sa2 5'- GGU CCU AUA CUU CAA CUG UUA AUU UCU GCC GCU UCU UUA CAU UCU AUC UU -3'

SbC2 5'- CAG AAA UUA ACU AAA GAA GCG GCA GAA AUU AAC UAA AGA AGC GG -3'

Sc2 5'- GGA CCA AGA UAG AAU GAG UUG AAG UAU A -3'

RNA sequences for design 2 left nick position (D2L)

Sa2 5'- GGU CCU AUA CUU CAA CUG UUA AUU UCU GCC GCU UCU UUA CAU UCU AUC UU -3'

SbL2 5'- GAA AUU AAC UAA AGA AGC GGC AGA AAU UAA CUA AAG AAG CGG CA -3'

Sc2 5'- GGA CCA AGA UAG AAU GAG UUG AAG UAU A -3'

6.2 RNA sequences for tiles with blunt ends

RNA sequences for design 1 right nick position (D1R)

Sa1 5'- G ACU AUG CAA CCU GC CUG GCA AGA CCU ACG AUG GAC ACG GUA ACG -3'

SbR1 5'- GUC UUG CCA GGC ACC AUC GUA GGU CUU GCC AGG CAC CAU CGU AG -3'

Sc1 5'- C GUU ACC GUG UGG UUG CAU AGU C -3'

RNA sequences for design 1 center nick position (D1C)

Sa1 5'- G ACU AUG CAA CCU GC CUG GCA AGA CCU ACG AUG GAC ACG GUA ACG -3'

SbC1 5'- CUU GCC AGG CAC CAU CGU AGG UCU UGC CAG GCA CCA UCG UAG GU -3'

Sc1 5'- C GUU ACC GUG UGG UUG CAU AGU C -3'

RNA sequences for design 1 center nick position (D1C)

Sa1 5'- G ACU AUG CAA CCU GC CUG GCA AGA CCU ACG AUG GAC ACG GUA ACG -3'

SbL1 5'- UGC CAG GCA CCA UCG UAG GUC UUG CCA GGC ACC AUC GUA GGU CU -3'

Sc1 5'- C GUU ACC GUG UGG UUG CAU AGU C -3'

RNA sequences for design 1 center nick position (D2R)

Sa2 5'- UAU ACU UCA ACU GUU AAU UUC UGC CGC UUC UUU ACA UUC UAU CUU -3'

SbR2 5'- GGC AGA AAU UAA CUA AAG AAG CGG CAG AAA UUA ACU AAA GAA GC -3'

Sc2 5'- A AGA UAG AAU GAG UUG AAG UAU A -3'

RNA sequences for design 1 center nick position (D2C)

Sa2 5'- UAU ACU UCA ACU GUU AAU UUC UGC CGC UUC UUU ACA UUC UAU CUU -3'

SbC2 5'- CAG AAA UUA ACU AAA GAA GCG GCA GAA AUU AAC UAA AGA AGC GG -3'

Sc2 5'- A AGA UAG AAU GAG UUG AAG UAU A -3'

RNA sequences for design 1 center nick position (D2L)

Sa2 5'- UAU ACU UCA ACU GUU AAU UUC UGC CGC UUC UUU ACA UUC UAU CUU -3'

SbL2 5'- GAA AUU AAC UAA AGA AGC GGC AGA AAU UAA CUA AAG AAG CGG CA -3'

Sc2 5'- A AGA UAG AAU GAG UUG AAG UAU A -3'

6.3 RNA tile schemes

Fig. 6.1 provides an overview of the expected secondary structure of each RNA tile design.

Figure 6.1: **Tile assembly for each design** D1R: design 1, right nick position. D1C: design 1, central nick position. D1L: design 1, left nick position. D2R: design 2, right nick position. D2C: design 2, central nick position. D2L: design 2, left nick position.

6.4 Methods

6.4.1 Sample preparation

We prepared RNA nanostructures with two distinct protocols: 1) slowly annealing extracted and purified RNA and 2) transcribing RNA and slowly annealing without purification, in a one-pot process. Samples for each protocol were prepared as follows:

1) For the extracted and purified anneal of RNA strands, all three RNA strands were transcribed, gel extracted and purified using the protocol described in Section 6.4.5. Strands were added in a 2:1:2 ratio (Sa:Sb:Sc) as shown in the tile scheme in section 6.3 to a solution of 1X Tris-acetate-EDTA (TAE) and 12.5 mM Magnesium Chloride. The solution was then annealed from 70°C to 22°C over 24 hours. The final tile concentration for this protocol is 500 nM (For D1R, Sa1 = 1 μM, SbR1 = 500 nM and Sc1 = 1 μM).

2) For the one pot assembly, the three templates transcribing tile RNA strands (see tile scheme in Section 6.3) were added in a 2:1:2 ratio (Sa:Sb:Sc) to a solution of 1X TAE, 22.5 mM Magnesium Chloride, 2.25 mM of each NTP, 10 mM DTT, and 1/6 volume dilution of AmpliScribe T7-Flash Enzyme Solution (Epicentre, # ASF3507). The quantity templates added to the one sample was 1:0.5:1 μg (Sa:Sb:Sc). The total reaction volume was 20 μl The solution was then allowed to incubate at 37°C for 15 minutes, then immediately annealed from 70°C to 22°C over 24 hours. The quantity of templates added can be tuned by changing it by $\pm 0.5\mu$g, while keeping the ratios the same.

6.4.2 Atomic force microscopy

AFM images were obtained in tapping mode using 1X TAE/12.5 mM Magnesium Chloride as imaging buffer with a Digital Instruments Multimode AFM, equipped with a Nanoscope III controller. Sharp Nitride Lever (SNL) tips from Bruker with a nominal spring constant of 0.24 N/m were used for imaging, with a drive frequency of 9-10 kHz. After annealing 5 μL of sample was taken directly from the test tube and was added to a freshly cleaved mica surface, it was allowed to adsorb for 30 seconds, then 25 μL of AFM buffer was added onto the sample on the mica surface and 25 μL of AFM buffer was added to the AFM tip.

6.4.3 Transmission electron microscopy

TEM images were obtained using the FEI Tecnai12 TEM consisting of twin objective lens, 0.34 nm point resolution, 0.20 line resolution. The electron source was set to 20 kV and a single tilt holder was used. Digital image processing was done with the Gatan US1000 digital CCD camera. TEM grids were glow discharged using Cressington Coating System. 5 μL of sample was placed on parafilm, the TEM grid was placed copper side down on sample for 5 minutes. Excess sample was carefully wicked away. The grid was then rinsed, by placing the grid copper side down on a droplet of DI water for 5 minutes; excess liquid was wicked away and the grid was rinsed once more using this method. Excess liquid was removed with Whatman paper. Grid was then placed copper side up, and 5 μL of 1% uranyl acetate was added and allowed to stain for 30 seconds.

6.4.4 Polyacrylamide gel electrophoresis (PAGE)

Denaturing PAGE

Pre-mix was prepared (for a final volume of 100 mL) by adding 42 g of urea to 25 ml of nanopure water, the mixture was then heated until the urea completely dissolved. This mixture was allowed to cool to room temperature, then acrylamide/bis-acrylamide 19:1, 40% solution was added. The pre-mix was added in appropriate ratios with TBE and nanopure water, ammonium persulfate (APS), and Tetramethylethylenediamine (TEMED) to cast the desired polyacrylamide percentage. Gels were cast in 10×10 cm, 1 mm thick disposable mini gel cassettes (Thermo Scientific, #NC2010) and allowed to polymerize for at least 2 hours before electrophoresis. Gels were run at room temperature at 100 V in 1X TBE unless otherwise noted. After electrophoresis the gels were stained in SYBR®Gold Nucleic Acid Gel Stain for 20-30 minutes. We purchased the 10bp DNA ladder used in denaturing gels from Thermofisher (Cat No: 10821015).

Non-denaturing PAGE

Acrylamide/bis-acrylamide 19:1, 40% solution, TAE, Magnesium Chloride 12.5 mM (final concentration), APS, and TEMED were added together at appropriate concentrations for the desired polyacrylamide percentage, then cast in 10×10 cm, 1 mm thick disposable mini gel cassettes (Thermo Scientific, #NC2010) and allowed to polymerize for at least 2 hours before electrophoresis. Gels were run at 4°C at 150 V in 1X TBE buffer. After electrophoresis gels were stained in SYBR®Gold Nucleic Acid Gel Stain for 20 minutes then imaged using the Biorad ChemiDoc MP system.

6.4.5 RNA extraction

Using the AmpliScribe-T7-Flash Transcription Kit the following components were mixed at room temperature: RNase-free water, 1-1.5 g template, AmpliScribe T7-Flash 1X Reaction Buffer (Epicentre, # ASF3507), 9 mM NTPs, 40 U/L RiboGuard RNase Inhibitor (Epicentre, # RG90925), and 2 L of AmpliScribe T7-Flash Enzyme Solution (Epicentre, # ASF3507). This mix was incubated at 37°C for 4 hours.

After incubation, 20 L of loading dye was added to the 20 L transcription solution, and 8 L of the transcription/dye mix was added to each of the middle 5 lanes of the gel. The gel was run at 100 V at room temperature in 1X TBE.

After electrophoresis the gel was stained in 80 mL 1X TBE and 1 L SYBR®Gold Nucleic Acid Gel Stain (Thermo Scientific, # S-11494) for 20-30 minutes. The gel was then placed on a TLC silica gel 60 W F254S aluminum sheet (EMD Millipore, # 1055590001) covered in plastic wrap. The gel was then illuminated with UV light and the desired RNA band was cut out and chopped up into equal amounts and placed into 0.5 mL DNA Lobind tubes (Eppendorf, # 022431005), then 200 L of 0.3 M sodium acetate at pH 5.3 was added to the tubes. The tubes were then incubated at 42°C for ˜20 hours.

After incubation, the sodium acetate was removed and placed into 1.7 mL Rnase/Dnase free tubes. The old tubes were rinsed with 100 L of 0.3 M sodium acetate pH 5.3, which was added to the new tubes. Then 1 mL of freezer cold 100% ETOH and 1 L of glycogen was added into each tube and the sample was incubated at -20°C for 20 hours.

Next, the samples were spun at 13500 rpm at 4°C for 15 minutes. The white precipitate pellet (RNA) at the bottom of the tube was located and the supernatant was

carefully pipetted out of the tubes to avoid removal of the pellet. Then, 500 L of 70% freezer cold ETOH was added to the tubes and spun at 13500 rpm at 4°C for 5 minutes. The supernatant was carefully decanted again with a pipette. This washing procedure was repeated a third time.

After the last wash, as much supernatant was removed as possible, then the tubes were opened and placed in the vacuum concentrator and allowed to spin at room temperature for 15 minutes.

The samples were then resuspended in 10-15 L of Ambion nuclease free water (Ambion, # AM9932).

6.4.6 Agarose gel eletrophoresis

A 0.5% high-melt agarose gel (made using Bio-Rad Certified Megabase Agarose, Cat No:1613108) was prepared in 1x TBE and 6 mM $MgCl_2$by heating 0.5 g of Agarose in 100 mL of the buffer. Once the agarose was fully dissolved, the mixture was allowed to cool, Ethidium Bromide was added at 0.5g/ml concentration and before the mixture solidified, it was poured in to the gel cast (Owl Easycast B1 gel system, 9 x 11 cm - Thermo Scientific). RNA nanotubes at 0.5 M tile concentration, and 8 l total volume were loaded in the wells of the agarose gel. The samples were loaded onto the gel with Bromophenol blue as a tracking dye. The gel wells were sealed using thin films of solid agarose affixed on top of the wells using molten agarose, to reduce the loss of nanotubes that stay in the wells till the end of the run. The running buffer also contained Ethidium Bromide at 0.5g/ml concentration. The gel was run at room temperature at 60 V for 2.5 hours. Gel images were taken using a BioRad ChemiDoc MP gel imaging system.

6.5 Analysis of lattices and tubular structures

We used AFM images to quantify:

1) The vertical distance between tiles in D1R lattices produced with both gel-extraction and one-pot protocol. Distance was measured at multiple sites on the lattice, and the mean is 7.017 nm $\pm$ 0.598. Example measurements are shown in Fig. 6.2.

2) Height of D1R tubular structures produced with the gel-extraction protocol. Results are shown in Fig. 6.3. We measured height difference between open (single-layer) and closed (double-layer) tube sections, because the variability often seen in mica surface heights at different locations of a scan area makes height measurements (relative to the mica background) unreliable.

3) Length and width of D1R tubular structures. We considered AFM images of assemblies produced with the gel extraction and anneal protocol. We used one AFM image from each of three separate assembly experiments, and identified isolated tubular structures that did not overlap with other structures nor branch. We picked 10 isolated, tubular structures per images and measured their length and width. Width was measured at the extrema and at the center of the tube, and tube overall width was computed as the average of these three measurements. Histograms of the measurements are shown in Fig. 6.4.

6.6 Abortive and elongated transcripts

We emphasize the presence of abortive and elongated transcription products in our one-pot assembly protocol. Without providing a quantitative analysis, we show exam-

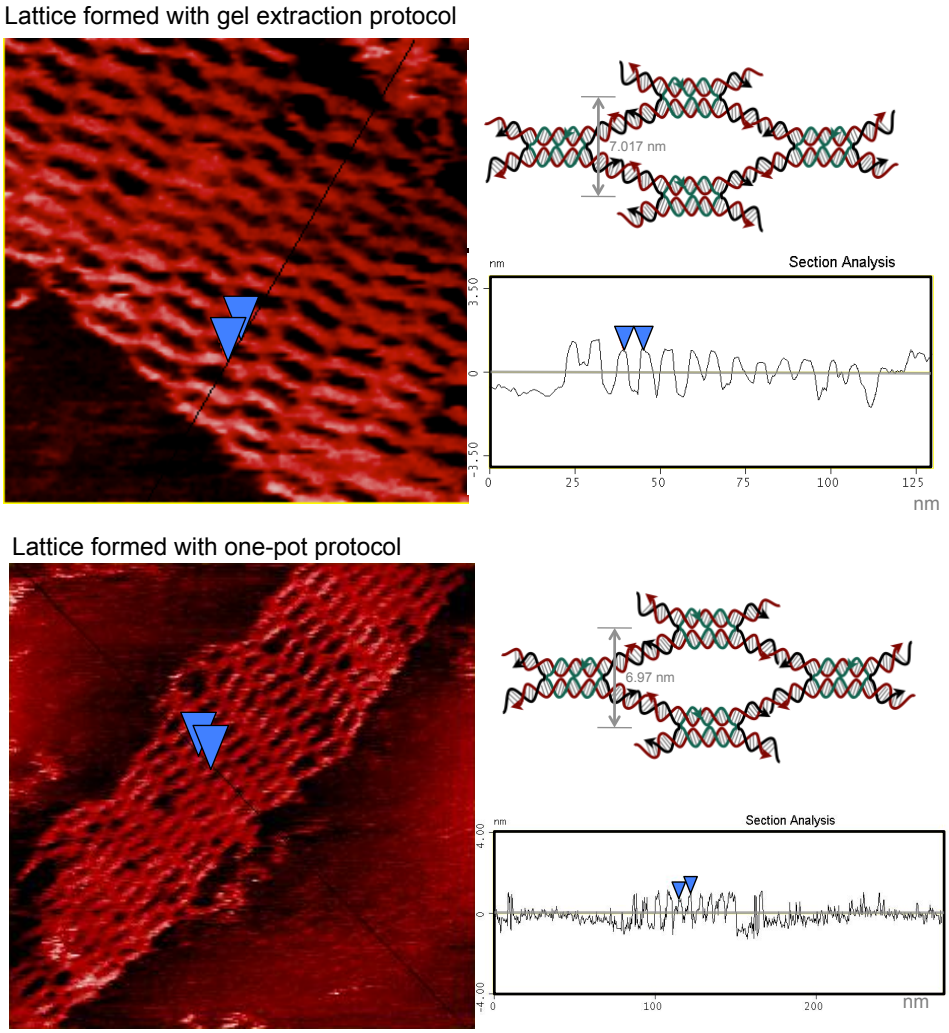

Figure 6.2: **Quantitative analysis of tiles and lattices** Tile analysis and measurements of extracted and purified annealed structures and one pot assembled structures, tile design D1R. The average distance between tiles (perpendicular to helical axis) is 7.017 nm $\pm$ 0.598.

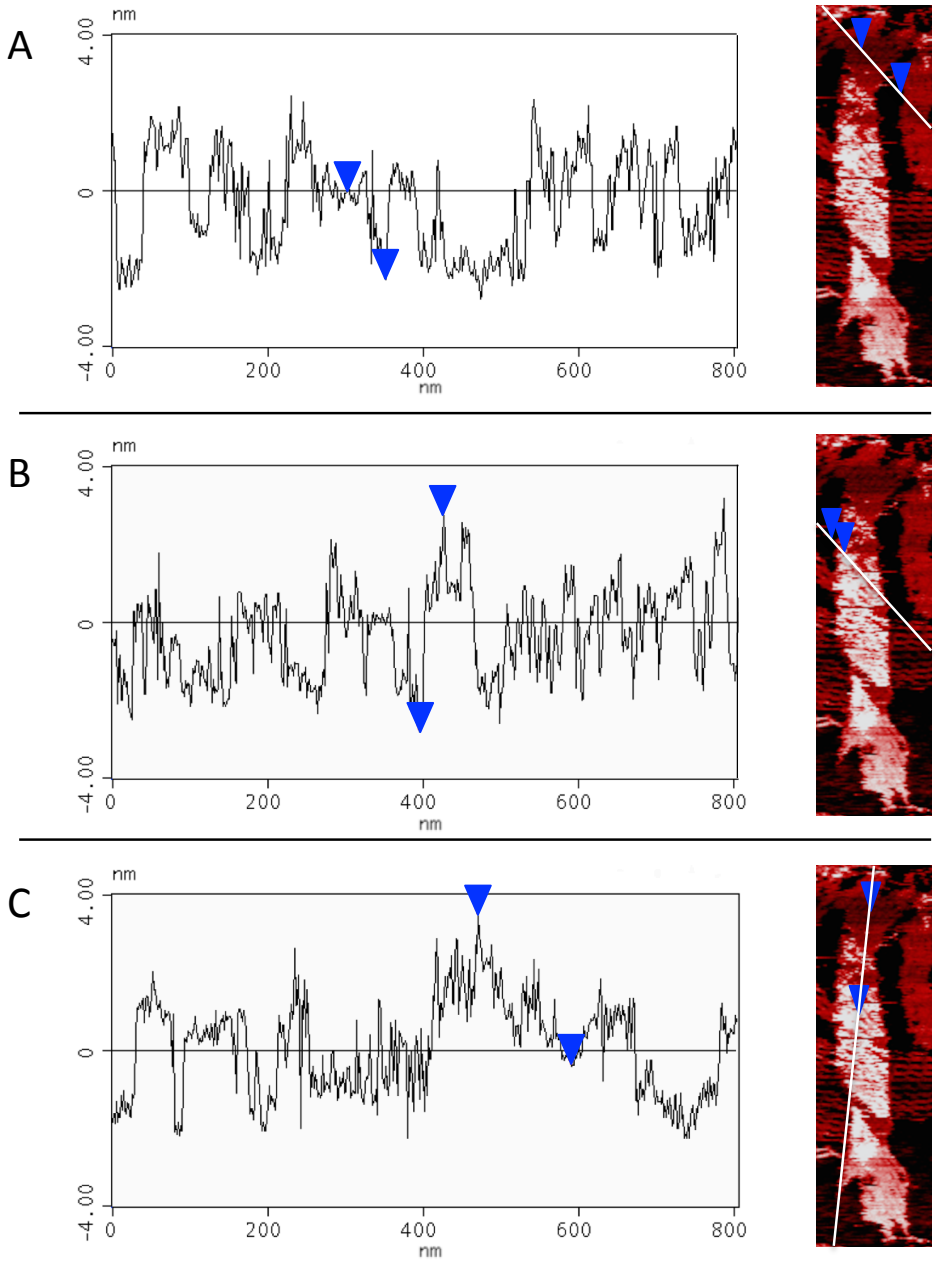

Figure 6.3: **Tube analysis and measurements, tile design D1R** A: Section analysis of single layer lattice height. B: Section analysis of double layer lattice height. C: Section analysis of difference between single layer lattice and double layer lattice height. The average height difference between single layer to double layer is 2.049 nm ± 0.269, which is consistent with the expected 2.3 nm diameter of an RNA double helix

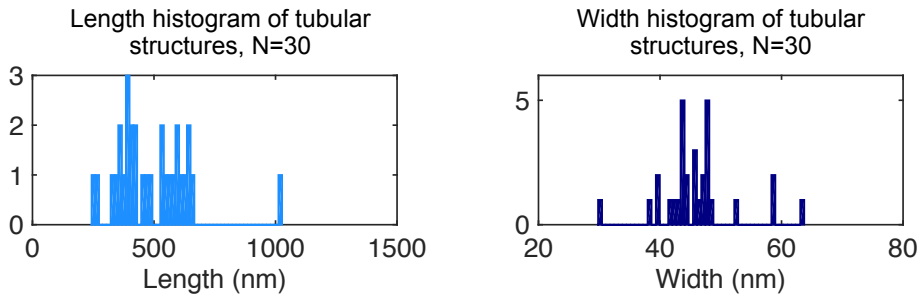

Figure 6.4: **Histograms of length and width of non-overlapping D1R tubular structures produced with the gel extraction and anneal protocol** Length and width were measured from AFM images. The length histogram is not meant to be a quantitative representation of our samples, because only few tubular structures are isolated on the mica surface.

ple gel electrophoresis images of transcription samples for each RNA strand tile component of design D1R. RNA transcription was performed using the AmpliScribe-T7-Flash Transcription Kit. 1 g of template was allowed to transcribe for 4 hours, with a sample taken at 30 minute intervals and immediately frozen at -20°C. RNA transcription samples were examined with denaturing polyacrylamide gel electrophoresis as shown in Fig. 6.5, using the protocol described in Section 6.4.4.

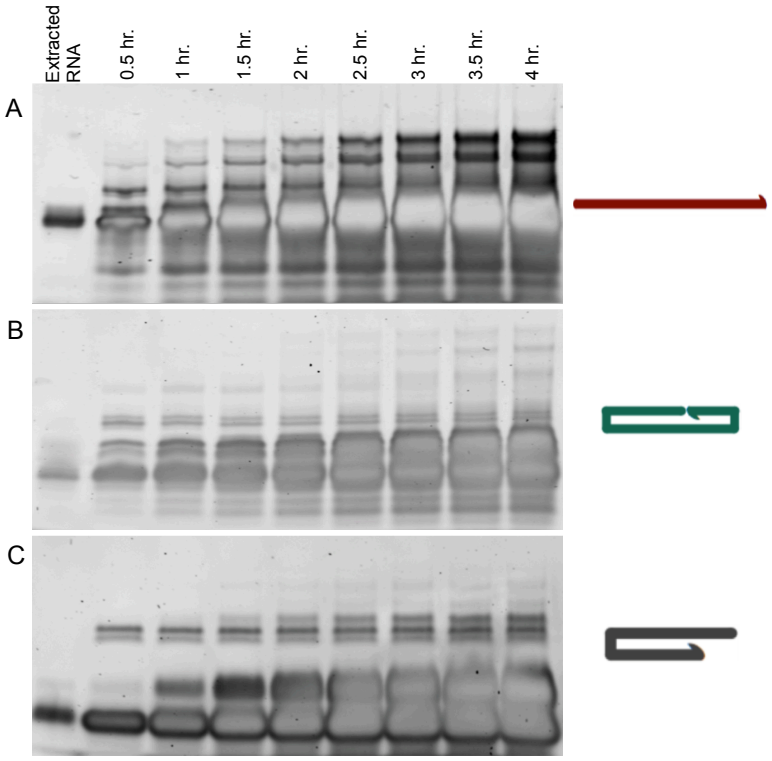

Figure 6.5: **Transcription over time** 10% denaturing PAGE showing transcription over time for D1R tile strands (with sticky ends). A-C: the first well to the left is a control sample of extracted and purified RNA. The presence of a significant amount of elongated and abortive transcripts is apparent in this example. A: Gel for strand Sa1, B: Strand SbR1, C: Strand Sc1.

6.7 Effects of thermal treatment on self-assembly

6.7.1 Maximum annealing temperature

Our RNA tiles do not form lattices when the maximum annealing temperature is below 70°C. To look for lower bounds on the maximum annealing temperature, we considered structures produced with the gel-extraction protocol. Fig. 6.7.1 compares example AFM images of D1R structures annealed with maximum annealing temperature of 65°C (Figure 6.7.1 A and B), where no structures are visible, and 70°C (Figure 6.7.1 C and D), where many lattices and tubular structures form. We conclude that structures do not form with a maximum annealing temperature below 70°C. For this experiment, extracted and purified RNA strands were added in a 2:1:2 (Sa:Sb:Sc) ratio to a solution of 1X TAE and 12.5 mM Magnesium Chloride.

We ran a similar experiment for structures produced with the one-pot protocol, where all three templates coding for the RNA strands were added in a 2:1:2 ratio to a solution of 1X TAE, 22.5 mM Magnesium Chloride, 2.25 mM of each NTP, 10 mM DTT, and 1/6 volume dilution of AmpliScribe T7-Flash Enzyme Solution. The solution was then allowed to incubate at 37°C for 15 minutes, then immediately slowly annealed from a given temperature to 22°C over 24 hours. We tested maximum heating temperatures of 45°C and 50°C, and neither resulted in assembly formation. Results are shown in Fig. 6.7.

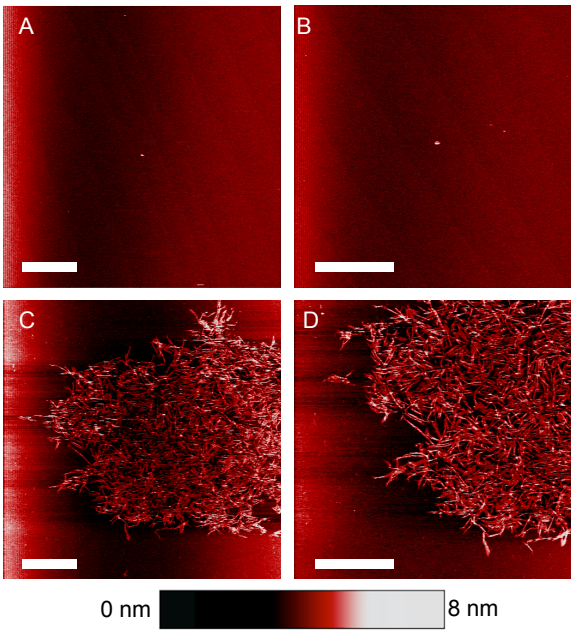

Figure 6.6: **AFM images of gel extracted, purified, and annealed D1R tiles, where the maximum heating temperature is varied** A: 24 hour anneal starting at 65°C, B: zoom of A, C: 24 hour anneal starting at 70°C, D: Zoom of C, scale bar 2 μm.

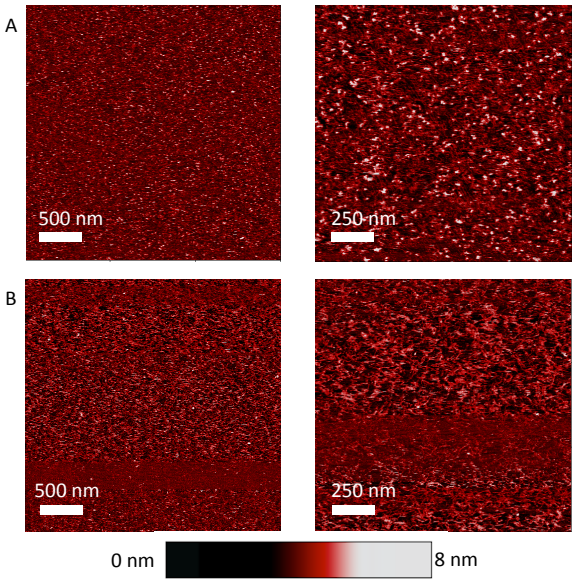

Figure 6.7: **AFM images of one pot co-transcribed and annealed D1R tiles** A. AFM images of samples co-transcribed at 37°C, then immediately annealed from 45°C to room temperature over 24 hours B. AFM images of samples co-transcribed at 37°C, then immediately annealed from 50°C to room temperature over 24 hours

6.7.2 Isothermal one pot assembly

Experiments for one-pot isothermal assembly were performed by adding all three templates transcribing RNA tile strands in a 2:1:2 ratio to a solution of 1X TAE, 12.5 mM Magnesium Chloride, 2.25 mM of each NTP, 10 mM DTT, and 1/6 volume dilution of AmpliScribe T7-Flash Enzyme Solution. The solution was incubated at 37°C for 4 hours, then AFM images of the samples were taken. Only tangled filaments are observed, as shown in Fig. 6.8.

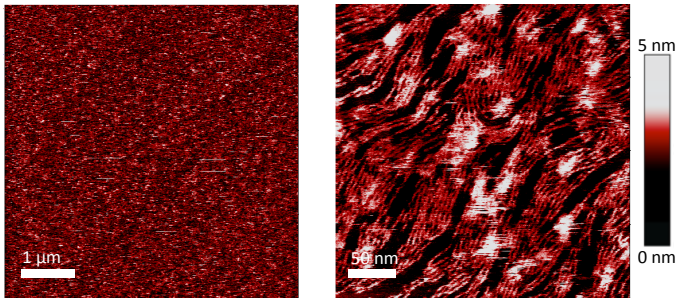

Figure 6.8: **AFM images of one-pot isothermally assembled D1R**

.

6.7.3 Nanostructure dynamics

To control assembly and disassembly of our structures, we modified our tiles to have binding domains or "toeholds," which can affect the strength of the inter-tile bonds or sticky ends. This idea has been successfully used to direct assembly in DNA nanotubes in the Franco Lab (unpublished data). We designed a toeholded tile with single-stranded overhangs or toeholds located on the 5' end of the tile's brown strands as illustrated in Fig. 6.9. These toeholded regions are complementary to an RNA input that interacts with the toeholded and sticky end regions to disassemble the RNA structures.

We found that the toeholded structures form better via co-transcription then anneal, so we assembled structures using this method, then transcribed the RNA input in a solution of 1X TAE, 12.5 mM magnesium chloride, 2.25 mM of each NTP, 10 mM DTT, and 0.5 units of AmpliScribe T7-Flash Enzyme Solution for 15 minutes, then incubated the sample for 5 minutes at 70°C to inactivate the RNA polymerase. We then added the transcribed RNA input to the co-transcribed structures and let the interactions occur for 30

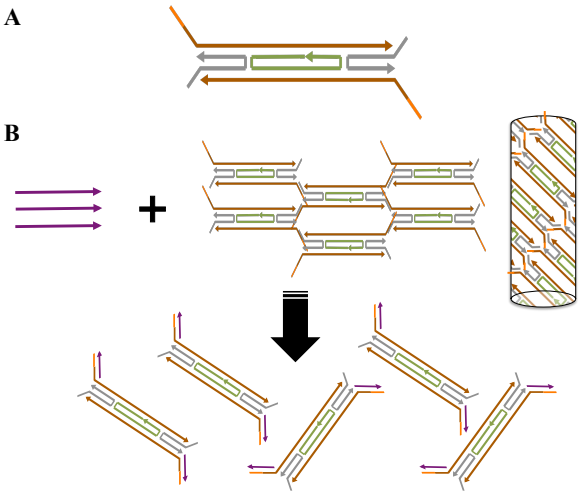

Figure 6.9: **Scheme of toehold mediated branch migration for the disassembly of RNA nanostructures** A. RNA tile with toeholds shown in orange B. Disassembly of RNA lattice and structure by RNA input in purple

minutes at room temperature, then imaged using AFM. These samples were compared to a control sample of co-transcribed and annealed structures where buffer at the same volume was added as the transcribed RNA input to the experimental sample. Fig. 6.10 shows AFM images of the structures pre and post transcriptionally triggered disassembly. We aim to reverse this process and implement a reassembly method where another RNA input will interact with the disassembly RNA input to allow the structure to reform again.

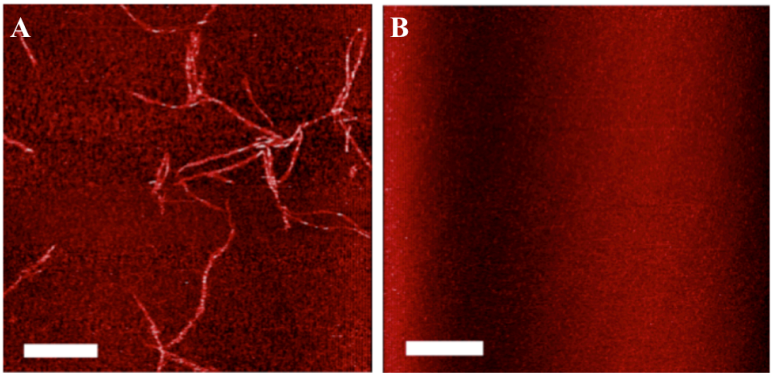

Figure 6.10: **Triggered disassembly of RNA nanostructures** A. AFM image of co-transcriptionally annealed RNA nanostructures B. AFM image of disassembled of RNA nanostructures, scale bar 2 μm

6.8 Role of Magnesium cation concentration

We investigated the influence of Magnesium Chloride concentration in 1X TAE buffer on structure assembly yield. We produced assemblies using our gel extraction protocol (sample preparation section 6.4.1) with varying $MgCl_2$ concentration. We observed that the Magnesium concentration in 1X TAE buffer dramatically influences structure formation (Fig. 6.11). We observed no structure formation in 1X TAE/ 2 mM Magnesium, because the presence of 2 mM EDTA is expected to titrate all Mg cations. At 1X TAE/ 4 mM Magnesium and 1X TAE/ 6 mM Magnesium we observed lattices and formation of some tubular structures. At 1X TAE/ 8 mM Magnesium we observed formation of lattices and of several tubular structures.

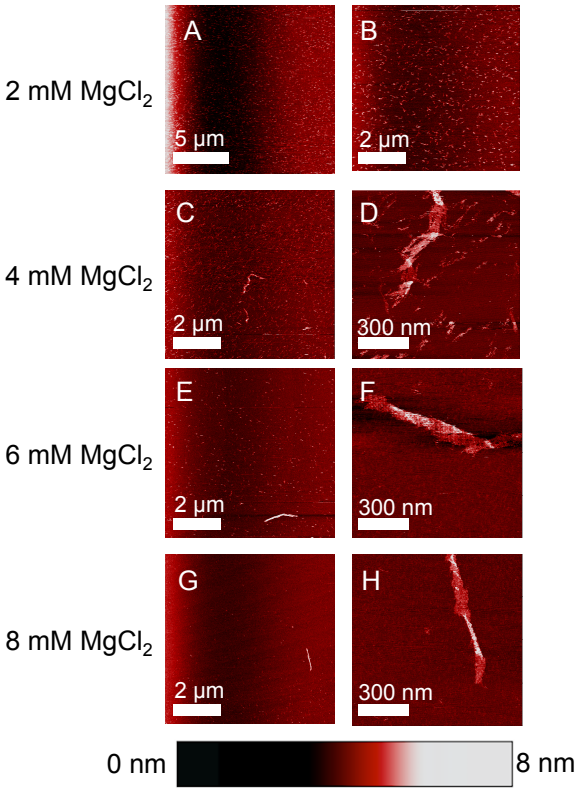

Figure 6.11: **AFM images of RNA nanostructures self-assembled from extracted and purified anneal of RNA strands in the presence of varying Magnesium concentrations** A-B. 2 mM Mg++ concentration C-D. 4 mM Mg++ concentration E-F 6 mM Mg++ concentration G-H. 8 mM Mg++ concentration

6.9 Role of RNA concentration

We investigated the effect of varying the tile component concentration on aggregation and yield. We mixed gel extracted RNA strands at different concentrations and we annealed them according to the details provided in the sample preparation section 6.4.1. We found that in the range considered (50 nM– 0.5 μM tile concentration), the concentration of extracted and purified RNA strands does not affect aggregation, as shown in Fig. 6.12. Unsurprisingly, the size of the aggregates is affected by the total RNA concentration: the greater the concentration of RNA used, the larger the aggregates.

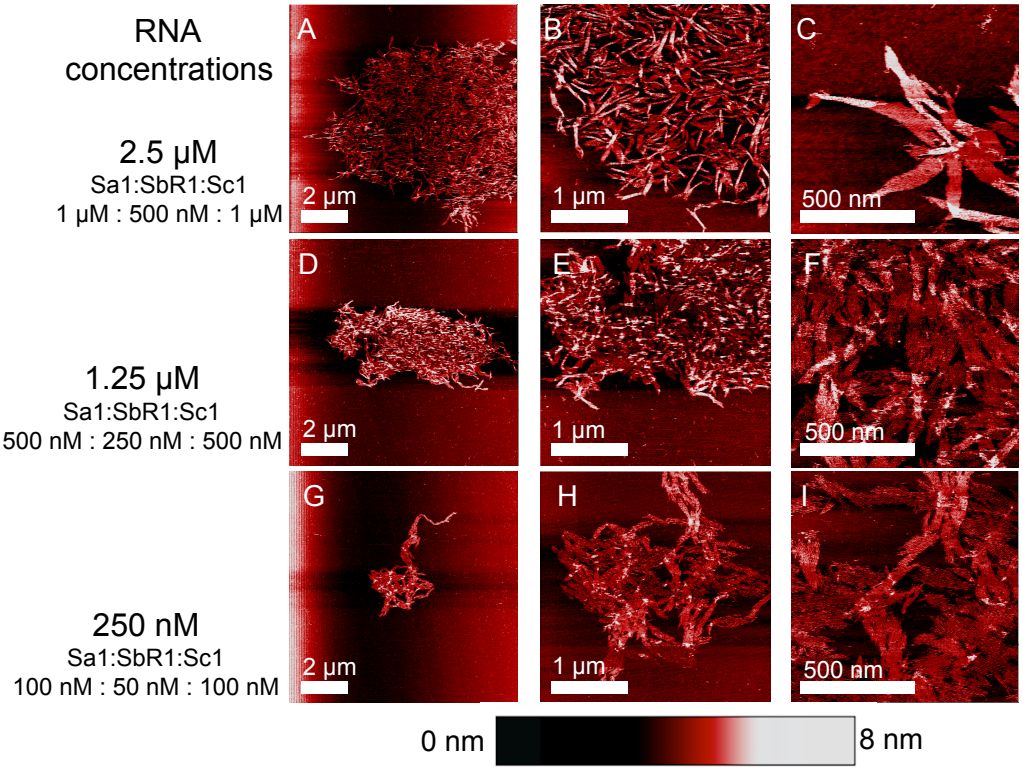

Figure 6.12: **AFM images of RNA nanostructures self-assembled from extracted and purified anneal of RNA strands** A-C: annealing concentrations 1 μM:500 nM:1 μM. D-E: annealing concentrations 250 nM: 125 nM: 250 nM. G-I: annealing concentrations 100 nM:50 nM:100 nM.

6.10 Strand interaction characterization via non-denaturing gel electrophoresis

We used non-denaturing gel electrophoresis to analyze the secondary structure of individual strands, two-species complexes, and full tiles. Samples were prepared as described in Section 6.4.1, Method 1. Individual RNA strands analyzed in lanes 1, 2, and 3 in each gel were not annealed. Gels were ran according to the protocol in Section 6.4.4; the concentration of RNA strands in each lane is annotated at the bottom of the lane.

6.10.1 Full tiles

Gels in Figs. 6.13 and 6.14 show the results of non-denaturing gel electrophoresis for all tile variants of design D1 and D2.

In Fig. 6.13 a thick band at the top of lane 7 in each gel for design D1 suggests that assemblies form in each design. High molecular weight polymers do not travel down the gels and are seen closer to the well. Tile D1C however did not produce any visible lattice in AFM or TEM experiments; qualitatively, the most prominent band in lane 7 of D1C runs lower than the corresponding lanes for tiles D1R and D1L, suggesting that individual strands interact but tiles may not properly fold. Strands Sa and Sb are designed to bind at a 2:1 stoichiometry: lanes 4 and 5 in each gel shows the complex forming when Sa and Sb are mixed and annealed respectively at a 1:1 (lane 4) or 2:1 (lane 5). While in designs D1R and D1L the product formed in lane 5 (correct stoichiometry) runs significantly higher than in lane 4, this difference is not observed in D1C. This suggests that the relevant strand complexes are not properly formed in D1C.

Fig. 6.14 shows that degradation of annealed species is very significant in design D2; this is particularly evident when comparing lanes 4 and 5. This is consistent with the fact that very few lattices were observed in AFM experiments for gel-extracted and annealed D2R and D2L tiles. Degradation occurs during the annealing process, and its rate depends both on the sequence content and the secondary structure of the strands [58]. Thus, electrophoresis experiments on annealed strands do not yield useful information on how strands in different variants interact. However, we point out that several large lattices were measured in one-pot annealed D2R tiles: thus, degradation rates may be reduced in transcription buffer, and perhaps enhanced by the gel-extraction process and combined with annealing in TAE 12.5 mM $MgCl_2$ buffer. (Unfortunately, gels on one-pot annealed samples would not be informative due to the large amount of short and elongated transcripts.)

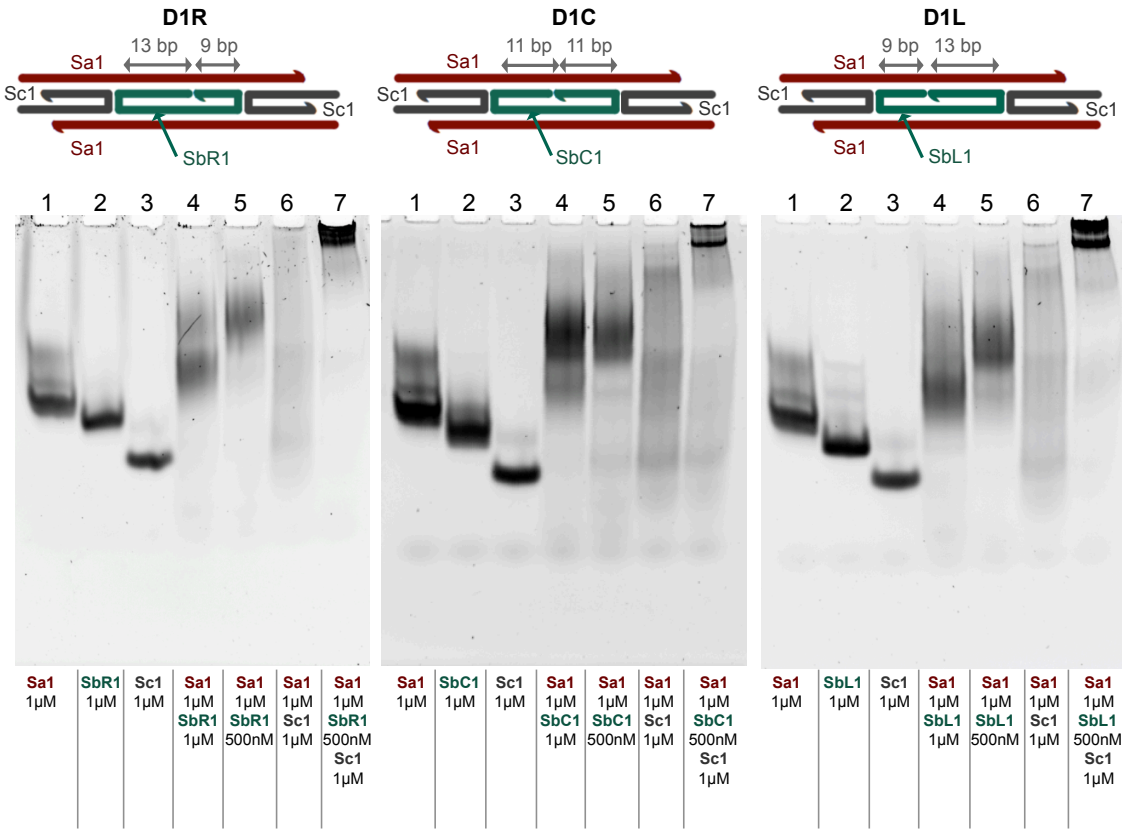

Figure 6.13: **12% non-denaturing gels of gel-extracted D1 full tile RNA strands**

6.10.2 Tiles with blunt ends

To examine more closely the bands corresponding to formation of individual tiles, we cropped the sticky end sequence from each tile design variant in design D1. Similar experiments were performed for design D2, but our results are inconclusive due to high degradation rate during annealing and are therefore not shown.

Lane 7 of gel D1R* and Lane 6 of gels D1C* and D1L* of Fig. 6.15 shows that products of similar size form in each variant when all strands are mixed and annealed in the appropriate stoichiometry. Two distinct bands form in lane 6 of the central nick design

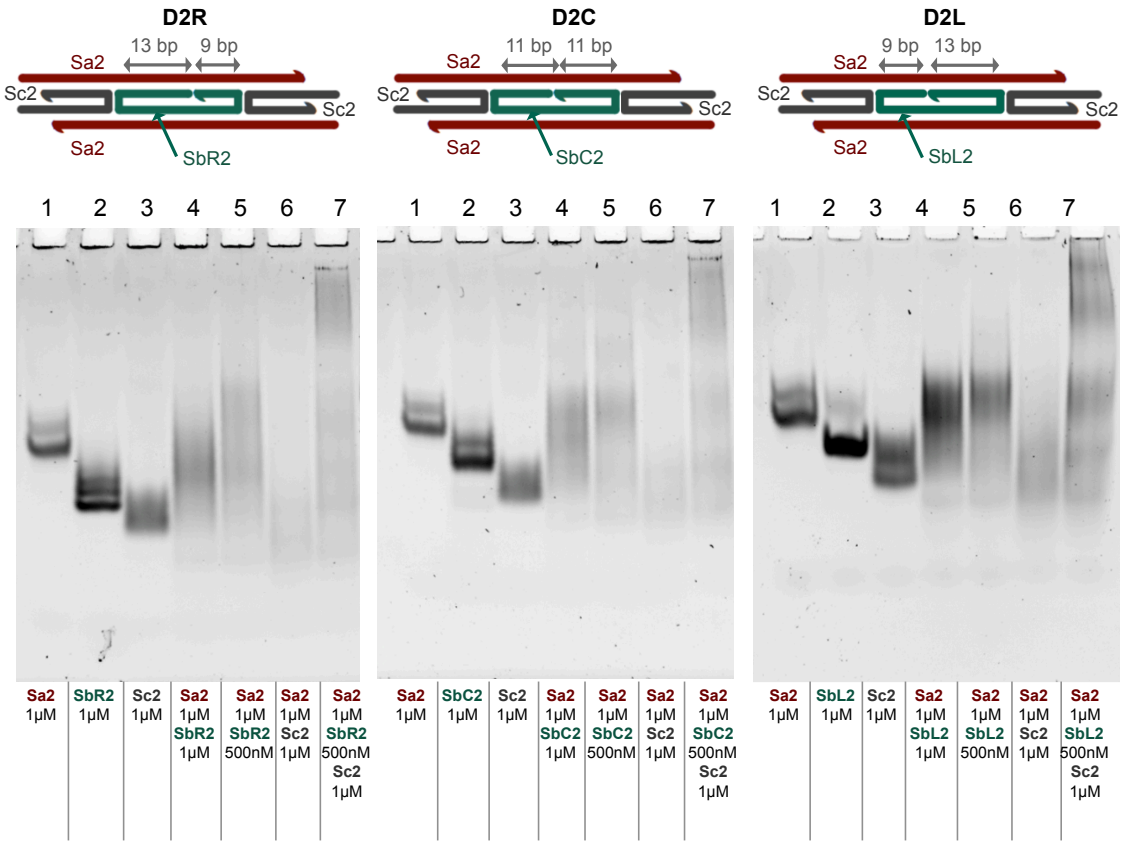

Figure 6.14: **12% non-denaturing gels of gel-extracted D2 full tile RNA strands**

D1C*; the lower band appears to be complex Sa1-SbC1, present (in isolation) in lanes 4 and 5. This complex seems to form a band that is sharper in D1C than in D1R and D1L, and may hinder proper formation of tiles and lattices. Lane 4 of D1R* and D1L* (where Sa and Sb are mixed with the wrong stoichiometry), shows the formation of complexes that appear to have smaller size than the desired three-strand complex, consistently with the D1R and D1L gels in Fig. 6.13.

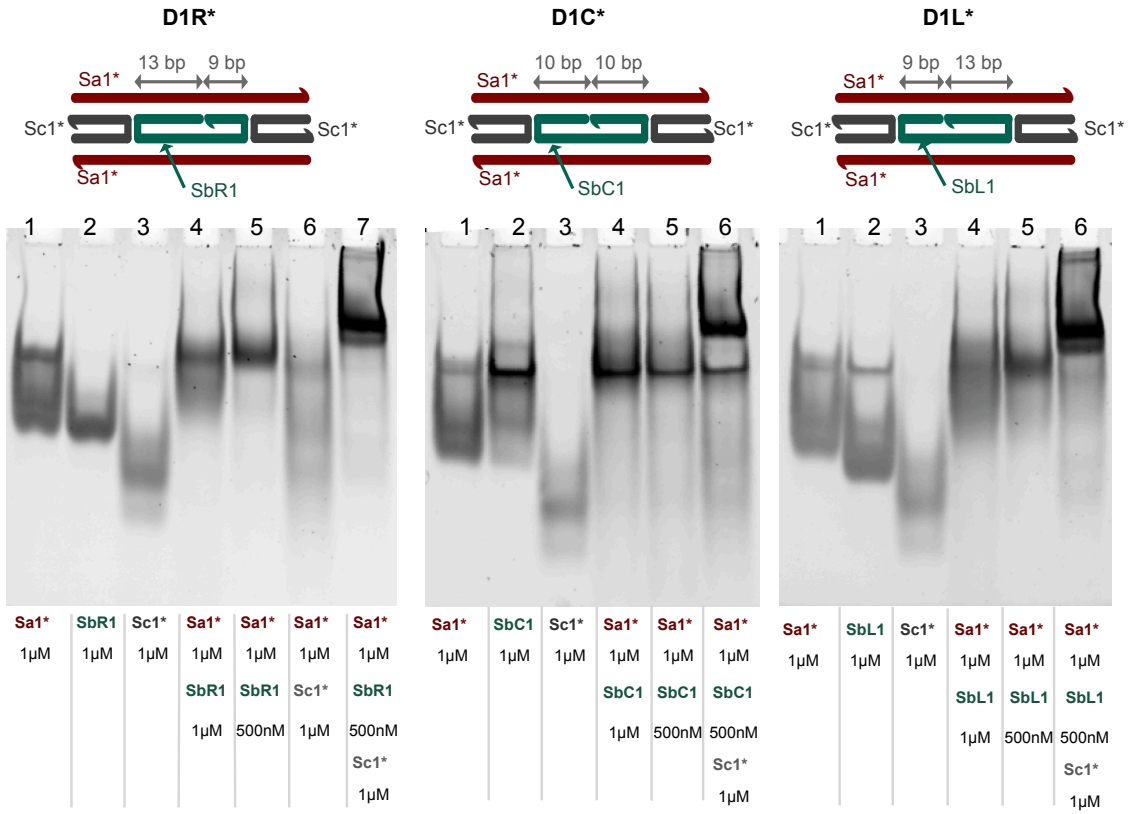

Figure 6.15: **12% non-denaturing gels on (gel-extracted) D1 RNA strands for blunt ended tiles**

6.11 TEM images

Fig. 6.16 shows example TEM images of assemblies from tile design 1 and 2, for all nick positions, produced with the gel extraction protocol.

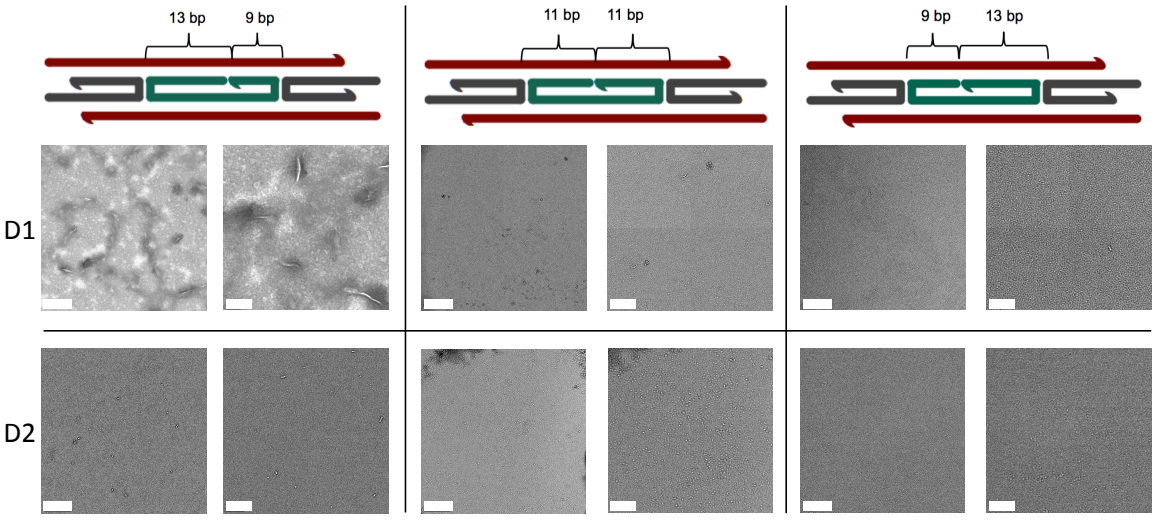

Figure 6.16: **TEM images of extracted and purified assemblies from all tile designs** leftmost image: scale bar: 500 nm, rightmost image: Zoom of leftmost image, scale bar: 250 nm.

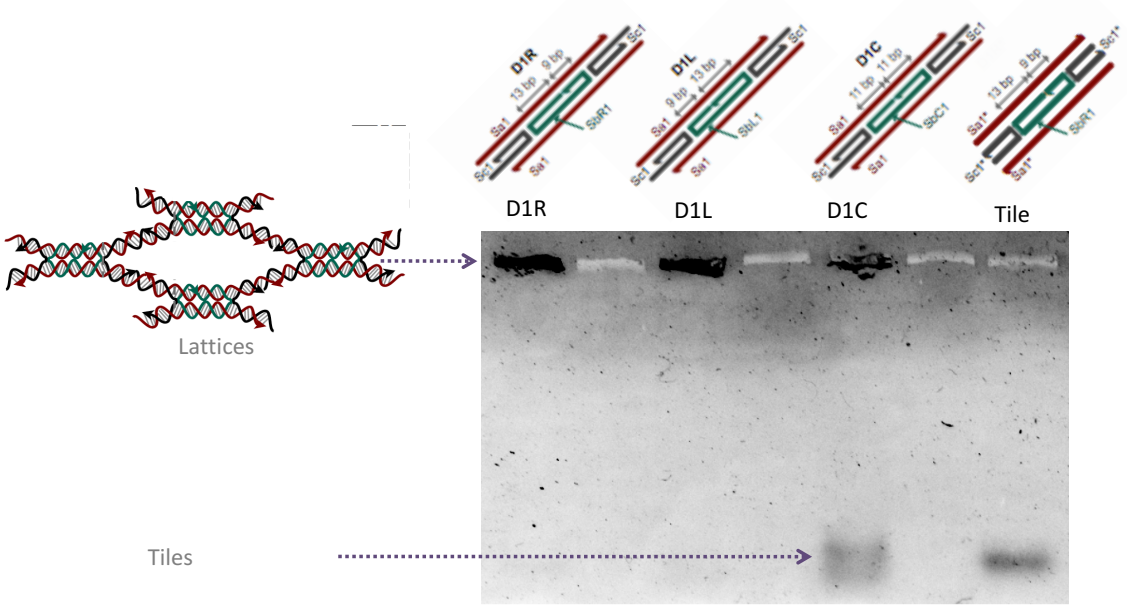

Figure 6.17: **Agarose gels of RNA tiles and lattices** Each type of tile was annealed and ran separately for comparison. The wells were sealed using agarose films in order to be able to visualize higher order structures that do not enter the gel. As a control for the monomer, D1R without sticky-ends was run.

6.12 Agarose gel of RNA tiles and lattices

To compare the size of products formed by different tile systems, we ran a 0.5% agarose gel (Fig. 6.17.). After loading the sample inside the wells of the gel, we sealed the well with a thin film of agarose and some molten agarose. This allowed us to visualize the higher order structures that do not enter the gel. As a control for the monomer tile, we ran a tile without sticky end in the right-most lane. In the gel the tiles with nick on the left and the right (D1R and D1L) do not have products short enough to enter the gel. But the tile with a central nick (D1C) has a significant amount of products that run similar to

a monomer tile on the gel. The quantity RNA in the well for D1C is also significantly less than D1R and D1L. This result is consistent with our AFM observations which show no lattices for the D1C sample. The results, shown in Fig. 4 of the manuscript, are reported here as well for the readers' convenience in Fig. 6.17.

6.13 Degradation studies

We performed degradation studies using denaturing gel electrophoresis. We tested the degradation of full tiles for both design 1 and design 2 for all nick positions. (Fig 6.18). For gels in Fig 6.18, we first annealed all the six tile variants using the gel extracted RNA strands with same protocol described in 6.4.1. Then we ran each of the tiles on a denaturing gel (protocol given in 6.4.4). We also had control lanes with unannealed, individual RNA strands and 10bp DNA ladders. The gel on the left shows the D1 design and the gel on the right shows D2 design. We can clearly see in the gel with D2 design that most of the RNA strands get degraded. In comparison, in the gel with D1 tiles, we see RNA bands and smears that run at or above the position of the individual strands on the control lanes. Despite the presence of denaturing agents, some secondary structure still survives in D1 designs, resulting in multimers and bands that run much higher than the individual strands in the control lanes. This would not be possible if strands in the D1 tiles are also degraded completely. Hence we show that the RNA strands of the D2 tiles degrade a lot more than those of D1 tile, upon annealing.

Interestingly, We found that when each strand is individually annealed from 70°C

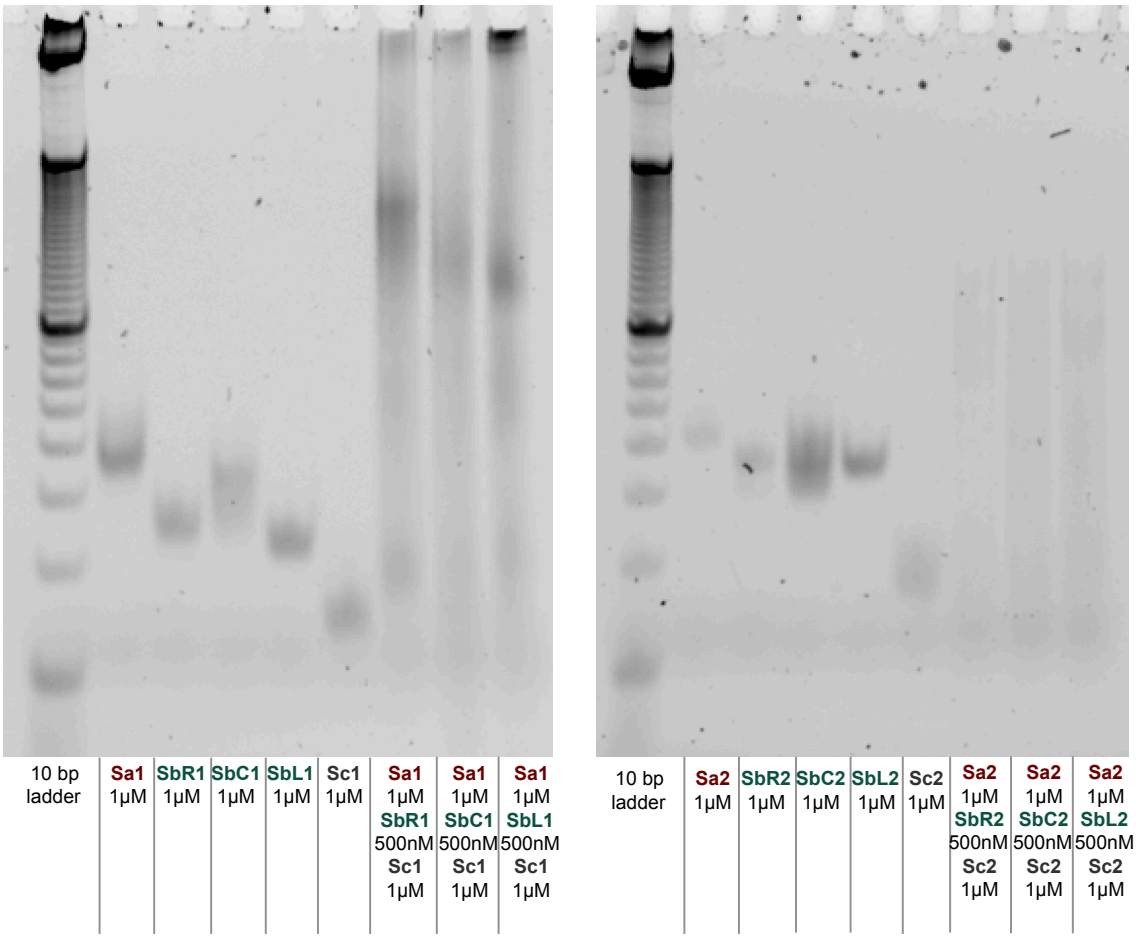

Figure 6.18: **Denaturing gel electrophoresis of full tiles** 10% Denaturing gel of design 1 and design 2 comparing the degradation that occurs when tiles are annealed. The gel on the left shows results for the D1 tile design variants D1R = (Sa1+SbR1+Sc1); D1C = (Sa1+SbC1+Sc1); D1C = (Sa1+SbL1+Sc1). The gel on the right shows results for D2 tile design variants, D2R = (Sa2+SbR2+Sc2); D2C = (Sa2+SbC2+Sc2); D1C = (Sa2+SbL2+Sc2). Each gel has unannealed individual strands as controls. As can be clearly seen, the strands for the D2 tile design degrade a lot more than the strands for D1 tile design. This gel was stained with SYBR®Safe DNA Gel Stain (Thermo Scientific, # S33102) for 15 minutes.

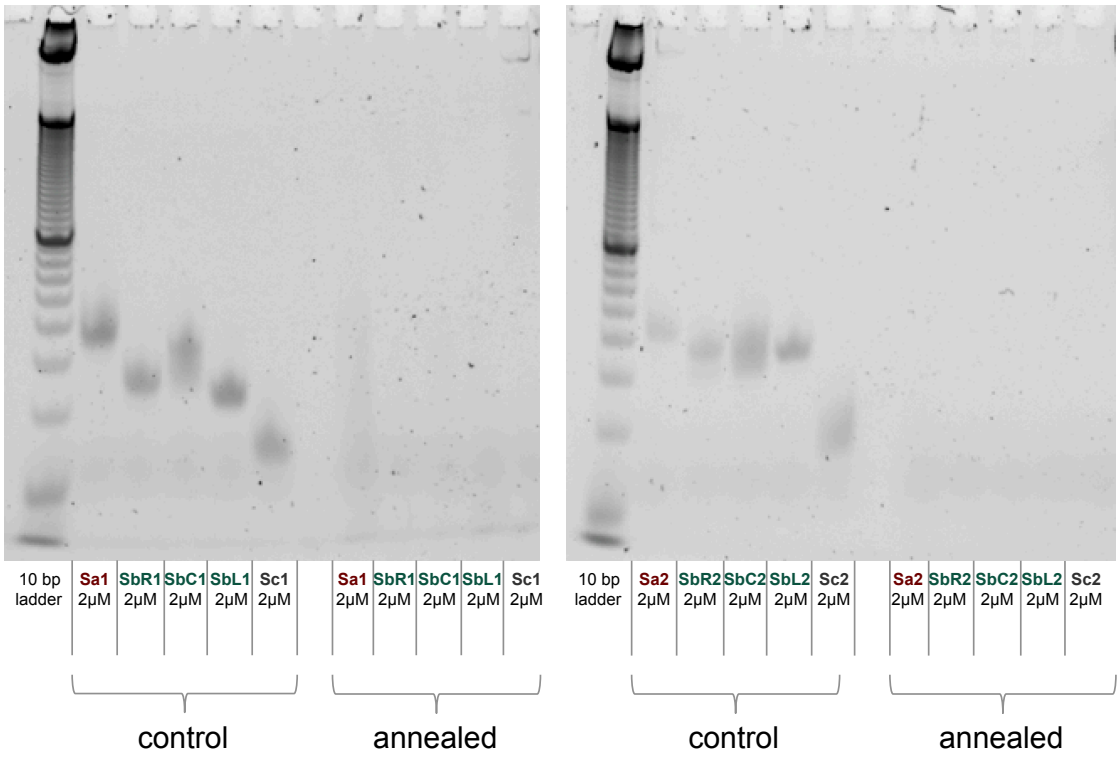

Figure 6.19: **Denaturing gel electrophoresis of individual strands** 10% Denaturing gel of design 1 (left) and design 2 (right) comparing the degradation that occurs when strands are individually annealed. The controls are strands that were not annealed. This gel was stained with SYBR®Safe DNA Gel Stain for 15 minutes.

to 22°C over 24 hours in TAE and magnesium buffer for both design 1 and design 2 strands degrade (Fig 6.19). This suggests that in case of D1 design, the presence and stability of the secondary structure (which, in turn, is sequence-dependent) protects the strands from degradation to some extent as seen in Fig. 6.19.

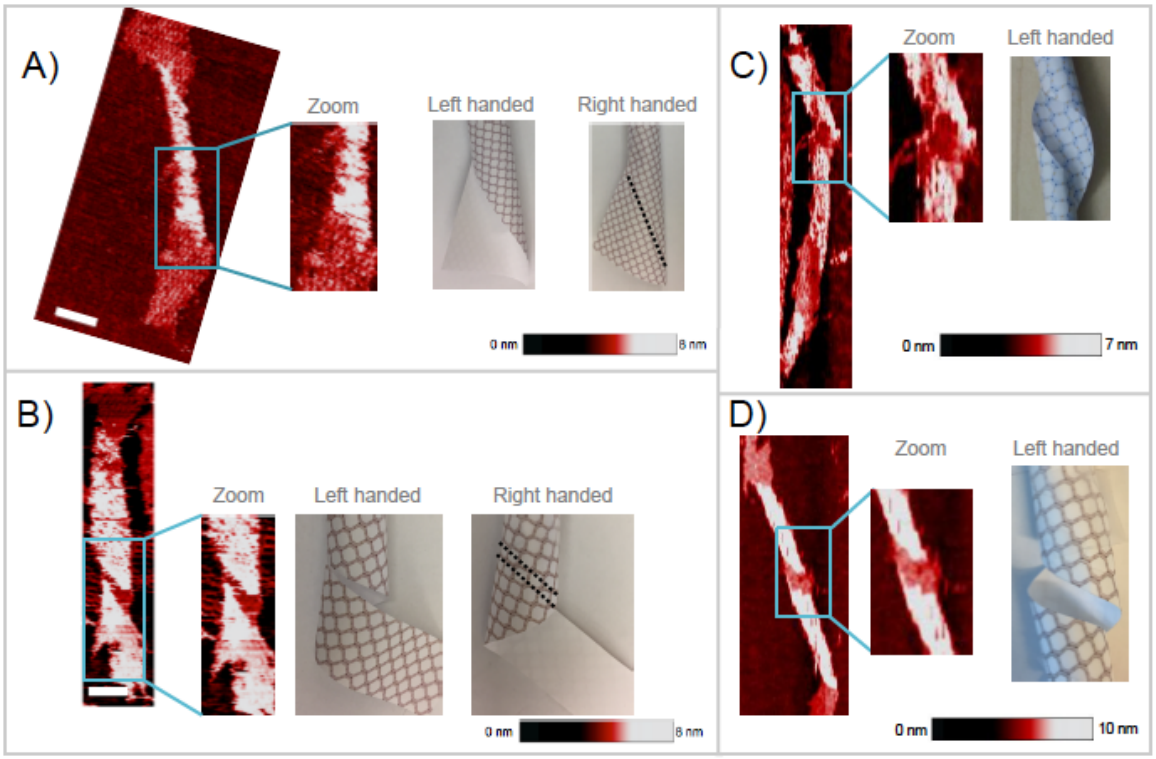

Figure 6.20: **AFM images of chiral tubes and paper models with possible interpretations about their handedness** The black dotted line in the right-handed interpretations represent the edge of the lattice underneath the top layer of lattice. In the paper models, the patterned surface represents the outer surface and the plain surface represents the inner surface.

6.14 Handedness of nanotubes

Since AFM images mainly convey the difference in height between the background, single, and double layers of RNA nanotubes, it is not always possible to interpret the handedness of a nanotube. But in some cases it is possible to interpret the AFM images as left-handed by observing the nature of the edges of the nanotube coil. Fig. 6.13 A shows an AFM image with transitions from single to double layer at the tube extrema. The two possible interpretations of this AFM image are shown as paper models. For the right-handed interpretation to be true, we will have to be able to see the edge of the tube (marked in black dotted lines in the figure) that lies beneath the first layer. This case is genuinely ambiguous and both interpretations (left and right-handed chirality) are valid.

Transitions from single-to double layer lattice in the middle of the tube are easier to interpret. Fig. 6.13 B shows an AFM image with such a transition. Unlike transition from single to double layer at the extrema, here we have the single layer bridged between two double layers. So, even though we are looking at a single layer in the middle, it is bridged between two double layers. And such a layer will be imaged at the same height as the double layer, unless there is a break in the lattice and the single layer gets deposited in the mica. We do not see any such abrupt break in the lattice at the edge and hence the left-handed interpretation is more likely. Also if we look at the bottom right corner of the AFM image, the single layer of lattice that appear to come out of the tube is imaged at same height as the double layer. This provides additional evidence for the left-handed interpretation. Fig. 6.13 C and Fig. 6.13 D also show a transition in the middle, and can be interpreted as left-handed using the same arguments made for Fig. 6.13 B.

Nanotube edges almost always go from bottom-right to top-left (if the tube is aligned to the vertical axis). If we indeed have a mixture of both right-handed and left-handed structures, we would also expect to see edges that go from bottom-left to top-right. Assuming one type of handedness shows up with edges going from bottom-right to top-left, we could conclude that we have a much higher population of one handedness over other. Given that some of the structures can be interpreted as left-handed and none so far can be interpreted as right-handed, can conclude that there is a higher likelihood of most structures being left-handed.

6.15 Overview of AFM images for each tile design

Fig. 6.21 compares AFM representative AFM images of RNA nanostructures produced from all our tile designs with both assembly protocols (gel extraction and one-pot).

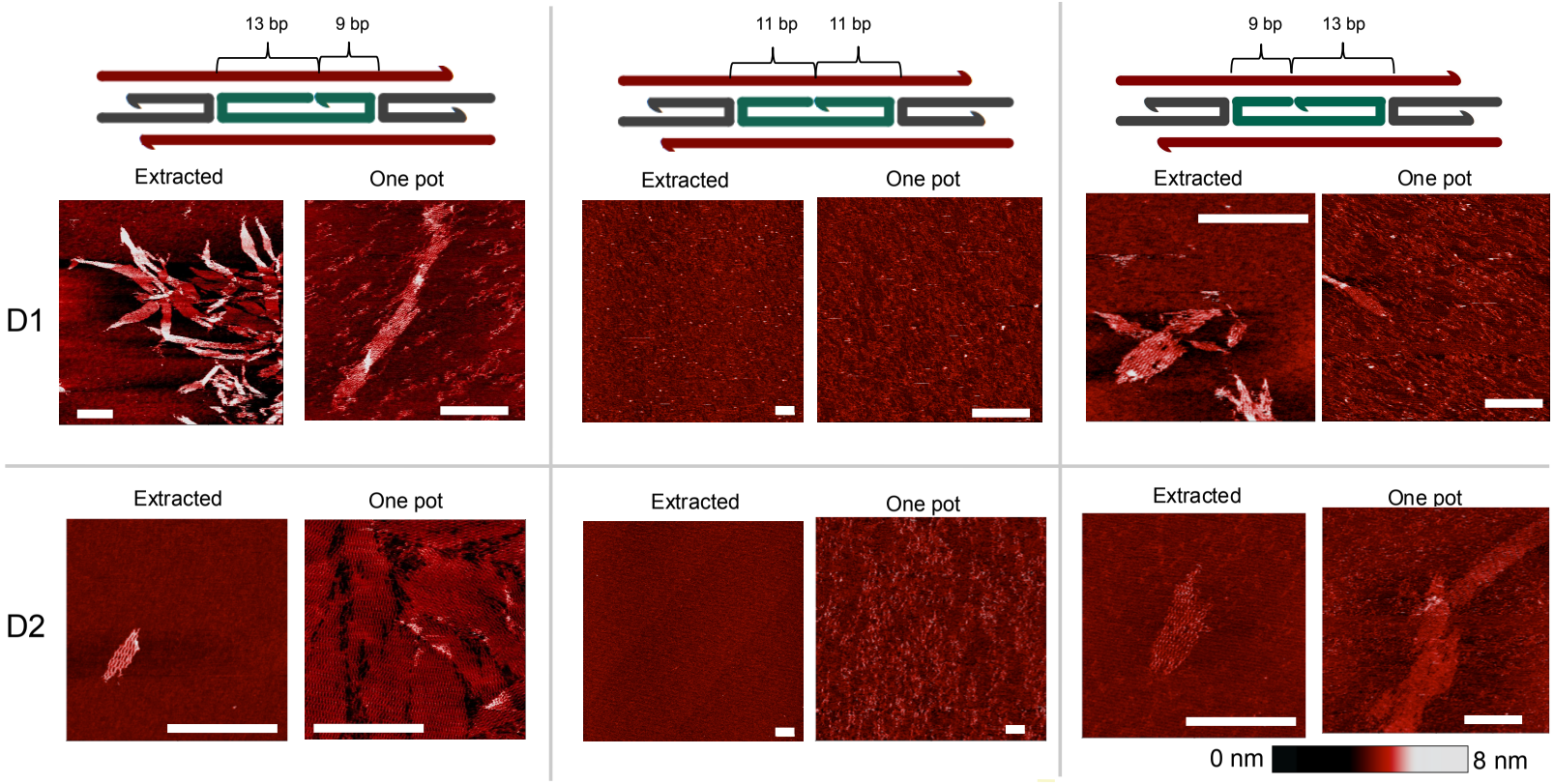

Figure 6.21: **Representative AFM images of nanostructures (or lack thereof) produced from all tile designs assembled from both protocols** scale bar is 250 nm.

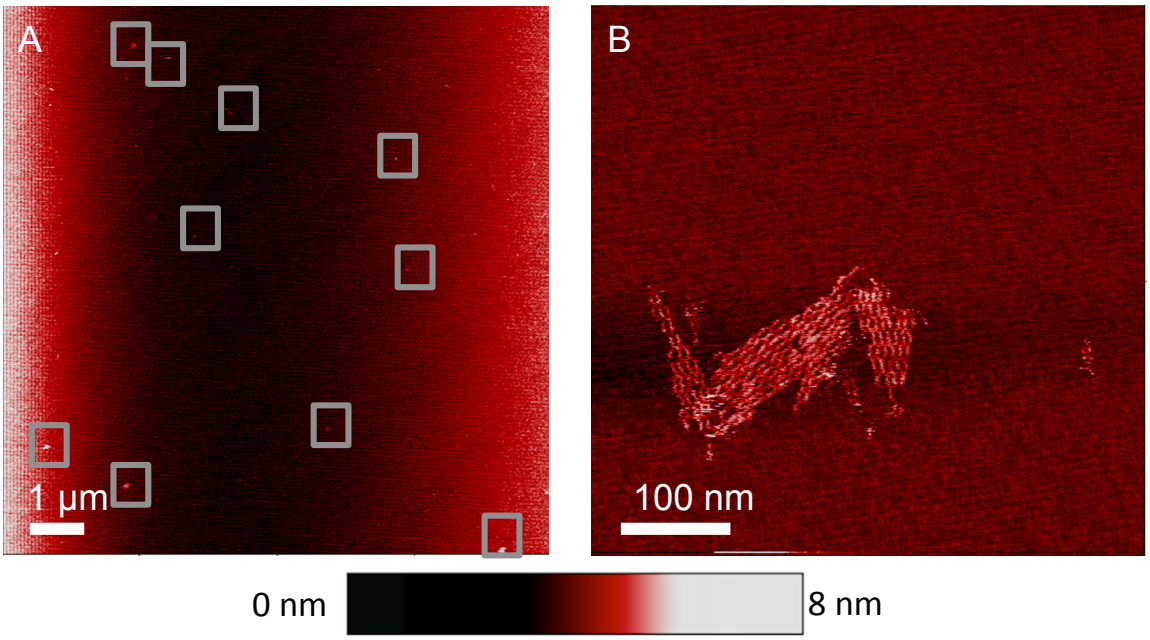

Figure 6.22: **AFM images of D2R tiles annealed from gel-extracted and purified RNA** A. AFM image with small lattices highlighted in the grey squares B. Zoomed AFM image of one of the grey squares in A showing a small lattice.

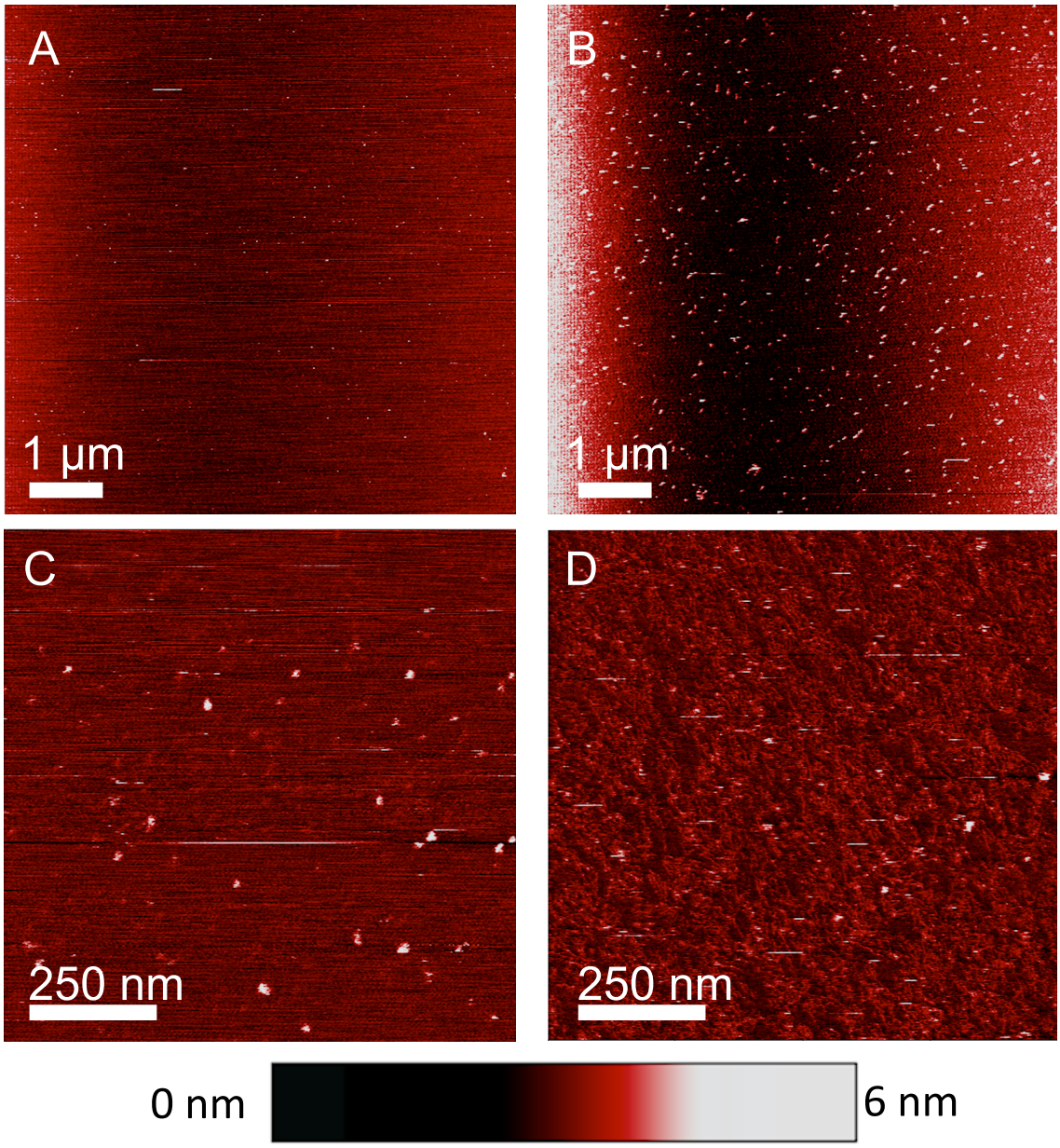

Figure 6.23: **AFM images showing of small filaments present on mica surface after annealing D1C** A. AFM image of only imaging buffer B. AFM image of D1C C. Zoom of A. D. Zoom of B.

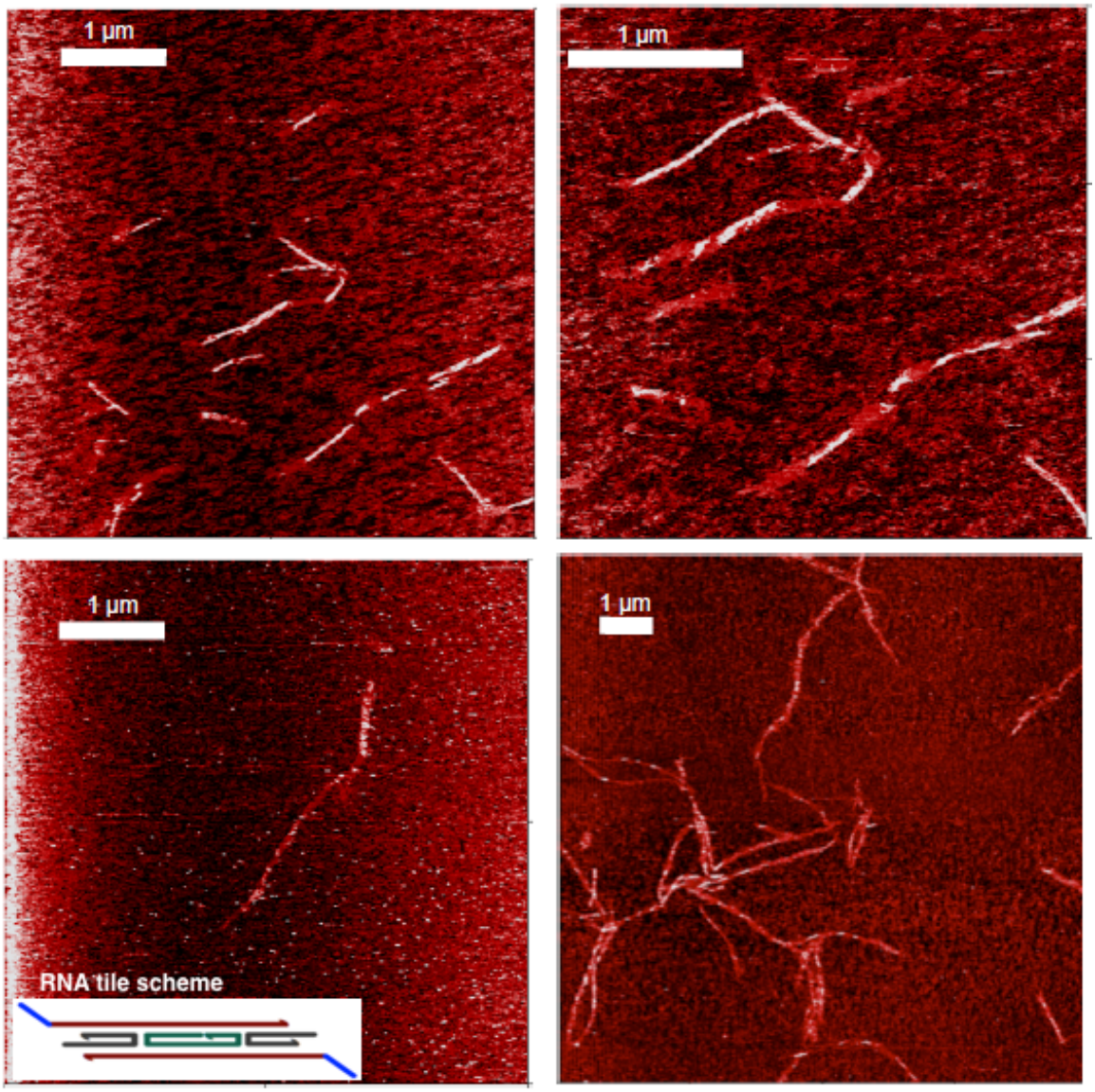

Figure 6.24: **AFM images showing tubes measuring close to 1 micron or more** These are tubes annealed using the one pot protocol with a variant of the D1R tile scheme (shown in the inset). This design has an extra overhang of 5 bases at the 5' end of the red strand, other than than that it is identical to the D1R tile. The general purpose of adding the 5 nt overhang was to its potential use as a domain for ligand attachment. We observed that the structures formed by this tile is are less aggregating than the standard D1R tile which makes it easier to quantify nanotube length.

Chapter 7

Supplementary Information for Programmable RNA microstructures for coordinated delivery of siRNAs

7.1 Sequences

RNA sequences for tile without siRNA were identified by converting to RNA the (44+6) tile design from . [65], as described by Stewart et al. [114]. PAGE purified DNA sequences were ordered from IDT DNA (Coralville, IA, USA). Genes include 3 base sealing domains (5' end of non-template strand) to prevent breathing at the 5' end of the promoter site. All genes include the T7 promoter sequence. The +1 to +6 promoter re-

gion (transcription start site) was modified relative to the generally recommended sequence (GGGAGA) [84], to avoid altering or constraining the sequence content of RNA tiles.

7.1.1 DNA templates

Sa

5'- TTC TAA TAC GAC TCA CTA TAG GTG CGA CTA TGC AAC CTG CCT GGC AAG ACC TAC GAT GGA CAC GGT AAC G -3' / 5'- CGT TAC CGT GTC CAT CGT AGG TCT TGC CAG GCA GGT TGC ATA GTC GCA CCT ATA GTG AGT CGT ATT AGA A -3'

Sb

5'- TTC TAA TAC GAC TCA CTA TAG TCT TGC CAG GCA CCA TCG TAG GTC TTG CCA GGC ACC ATC GTA G -3' / 5'- CTA CGA TGG TGC CTG GCA AGA CCT ACG ATG GTG CCT GGC AAG ACT ATA GTG AGT CGT ATT AGA A -3'

Sc

5'- TTC TAA TAC GAC TCA CTA TA GCA CCC GTT ACC GTG TGG TTG CAT AGT C -3' / 5'- GAC TAT GCA ACC ACA CGG TAA CGG GTG CTA TAG TGA GTC GTA TTA GAA -3'

Sc-GFP

5'- TTC TAA TAC GAC TCA CTA TAG CAC CCG TTA CCG TGT GGT TGC ATA GTC TTC GGT GGT GCA GAT GAA CTT CAG GGT CA -3' / 5'- TGA CCC TGA AGT TCA TCT GCA CCA CCG AAG ACT ATG CAA CCA CAC GGT AAC GGG TGC TAT AGT GAG TCG TAT TAG A -3'

Sc-PLK1

5’- TTC TAA TAC GAC TCA CTA TAG CAC CCG TTA CCG TGT GGT TGC ATA GTC TTC GTC ATT AAG CAG CTC GTT AAT GGT T -3’ / 5’- AAC CAT TAA CGA GCT GCT TAA TGA CGA AGA CTA TGC AAC CAC ACG GTA ACG GGT GCT ATA GTG AGT CGT ATT AGA A -3’

7.1.2 DNA templates for tiles with blunt ends

Sa

5’- TTC TAA TAC GAC TCA CTA TAG ACT ATG CAA CCT GCC TGG CAA GAC CTA CGA TGG ACA CGG TAA CG -3’ / 5’- CGT TAC CGT GTC CAT CGT AGG TCT TGC CAG GCA GGT TGC ATA GTC TAT AGT GAG TCG TAT TAG AA -3’

Sb

5’- TTC TAA TAC GAC TCA CTA TAG TCT TGC CAG GCA CCA TCG TAG GTC TTG CCA GGC ACC ATC GTA G -3’ / 5’- CTA CGA TGG TGC CTG GCA AGA CCT ACG ATG GTG CCT GGC AAG ACT ATA GTG AGT CGT ATT AGA A -3’

Sc

5’- TTC TAA TAC GAC TCA CTA TAC GTT ACC GTG TGG TTG CAT AGT C -3’ / 5’- GAC TAT GCA ACC ACA CGG TAA CGT ATA GTG AGT CGT ATT AGA A -3’

Sc-GFP

5’- TTC TAA TAC GAC TCA CTA TAC GTT ACC GTG TGG TTG CAT AGT CTT CGG TGG TGC AGA TGA ACT TCA GGG TCA -3’ / 5’- TGA CCC TGA AGT TCA TCT GCA CCA CCG AAG ACT ATG CAA CCA CAC GGT AAC GTA TAG TGA GTC GTA TTA GAA -3’

Sc-PLK1

5'- TTC TAA TAC GAC TCA CTA TAC GTT ACC GTG TGG TTG CAT AGT CTT CGT CAT TAA GCA GCT CGT TAA TGG TT -3' / 5'- AAC CAT TAA CGA GCT GCT TAA TGA CGA AGA CTA TGC AAC CAC ACG GTA ACG TAT AGT GAG TCG TAT TAG AA -3'

7.1.3 RNA sequences

Sa

5'- GGU GCG ACU AUG CAA CCU GC CUG GCA AGA CCU ACG AUG GAC ACG GUA ACG -3'

Sb

5'- GUC UUG CCA GGC ACC AUC GUA GGU CUU GCC AGG CAC CAU CGU AG -3'

Sc

5'- GCA CCC GUU ACC GUG UGG UUG CAU AGU C -3'

Sc-GFP

5'- GCA CCC GUU ACC GUG UGG UUG CAU AGU Cuu CGG UGG UGC AGA UGA ACU UCA GGG UCA -3'

Sc-PLK1

5'- GCA CCC GUU ACC GUG UGG UUG CAU AGU Cuu CGU CAU UAA GCA GCU CGU UAA UGG UU -3'

GFP sense

5'- pACC CUG AAG UUC AUC UGC ACC ACC G -3'

PLK1 sense

5'- pAAC CAU UAA CGA GCU GCU UAA UGA CG -3'

GFP sense labeled with Alexa488

5'- /5AlexF488N/ACC CUG AAG UUC AUC UGC ACC ACC G -3'

PLK1 sense labeled with Alexa546

5'- /5AlexF546N/CCA TTA ACG TGC TTA ATG ACG -3'

7.2 Methods

7.2.1 Sample preparation

We prepared RNA nanostructures by slowly annealing extracted and purified RNA. RNA strands were transcribed; gel extracted and purified using the RNA extraction protocol. Strands were added in a 2:1:2:2 ratio (Sa:Sb:Sc-antisense:Sense) Fig. **??** to a solution of 1X tris-acetate-EDTA (TAE) and 12.5 mM $MgCl_2$. The solution was then annealed from 70°C to 22°C over 24 hours.

7.2.2 Atomic force microscopy

AFM images were obtained in tapping mode using 1X TAE/12.5 mM Magnesium Chloride as imaging buffer with a Digital Instruments Multimode AFM, equipped with a Nanoscope III controller. Sharp Nitride Lever (SNL) tips from Bruker with a nominal spring constant of 0.24 N/m were used for imaging, with a drive frequency of 9-10 kHz. After annealing 5 μL of sample was taken directly from the test tube and was added to a freshly cleaved mica surface, it was allowed to adsorb for 30 seconds, then 25 μL of AFM

buffer was added onto the sample on the mica surface and 25 μL of AFM buffer was added to the AFM tip.

Fluorescence Microscopy

Images were obtained with a NIKON TI-E inverted fluorescence microscope. Cy3 filter was used to image all tiles with Cy3 labeled S3 strand 60x oil immersion objective was used to collect all images, with a standard exposure time of 600 ms.

7.2.3 Denaturing polyacrylamide gel electrophoresis

Pre-mix was prepared by adding 42 g of urea to 25 mL of nanopure water (for a final volume of 100 mL), the mixture was then heated until the urea completely dissolved. This mixture was allowed to cool to room temperature, then a 40% (v/v) 19:1 acrylamide/bis-acrylamide solution was added in the appropriate volume for the desired percentage. The pre-mix was added in appropriate ratios with TBE and nanopure water, ammonium persulfate (APS), and tetramethylethylenediamine (TEMED) to start polymerization. Gels were cast in 1010 cm, 1 mm thick disposable mini gel cassettes (Thermo Scientific, #NC2010) and allowed to polymerize for at least 2 hours before electrophoresis. Gels were run at room temperature at 100 V in 1X TBE unless otherwise noted. After electrophoresis the gels were stained in SYBR®Gold Nucleic Acid Gel Stain or ethidium bromide and then imaged using the Bio-Rad ChemiDoc MP system.

7.2.4 Non-denaturing polyacrylamide gel electrophoresis

40% solution of 19:1 acrylamide/bis-acrylamide, TAE, $MgCl_2$, APS, and TEMED were added together at appropriate concentrations for the desired polyacrylamide percentage, then cast in 1010 cm, 1 mm thick disposable mini gel cassettes (Thermo Scientific, #NC2010) and allowed to polymerize for at least 2 hours before electrophoresis. Gels were run at 4°C at 150 V in 1X TBE buffer. After electrophoresis gels were stained in SYBR®Gold Nucleic Acid Gel Stain or ethidium bromide and then imaged using the Bio-Rad ChemiDoc MP system.

7.2.5 RNA extraction

Using the AmpliScribe-T7-Flash Transcription Kit the following components were mixed at room temperature: RNase-free water, 1-1.5 μg gene, AmpliScribe T7-Flash 1X Reaction Buffer (Epicentre, #ASF3507), 9 mM NTPs, 40 U/μL RiboGuard RNase Inhibitor (Epicentre, #RG90925), and 1 unit of AmpliScribe T7-Flash Enzyme Solution (Epicentre, ASF3507). This mix was incubated at 37°C for 4 hours. After incubation, 20 μL of loading dye was added to the 20 μL transcription solution, and 8 μL of the transcription/dye mix was added to each of the middle 5 lanes of the gel. The gel was run at 100 V at room temperature in 1X TBE.

After electrophoresis the gel was stained in 80 mL 1X TBE and 1 μL SYBR®Gold Nucleic Acid Gel Stain (Thermo Scientific, # S-11494) for 20-30 minutes. The gel was then placed on a TLC silica gel 60 W F254S aluminum sheet (EMD Millipore, #1055590001) covered in plastic wrap. The gel was illuminated with UV light and the desired RNA band

was cut out and chopped into equal amounts and placed into 0.5 mL DNA Lobind tubes (Eppendorf, #022431005), then 200 μL of 0.3 M sodium acetate at pH 5.3 was added to the Lobind tubes. The samples were then incubated at 42°C for 20 hours. After incubation, the sodium acetate was removed and placed into 1.7 mL RNase/DNase free tubes. The old Lobind tubes were rinsed with 100 μl of 0.3 M sodium acetate pH 5.3, which was added to the new samples. Then 1 mL of freezer cold 100% ETOH and 1 μL of glycogen were added into each tube and the sample was incubated at -20°C for 20 hours.

Next, the samples were spun at 13,500 rpm at 4°C for 15 minutes. The white precipitate pellet (RNA) at the bottom of the tube was located and the supernatant was carefully pipetted out of the tubes avoiding removal of the pellet. Then, 500 μl of 70% freezer cold ETOH was added to the tubes and spun at 13,500 rpm at 4°C for 5 minutes. The supernatant was carefully decanted again with a pipette. This washing procedure was repeated a third time. After the last wash, as much supernatant was removed as possible, then the samples were opened and placed in the vacuum concentrator and allowed to spin at room temperature for 15 minutes. The samples were then re-suspended in 10-15 μL of Ambion nuclease free water (Ambion, #AM9932).

7.2.6 Tile and lattice purification

Structures were annealed in 1X TAE / 12.5 mM $MgCl_2$ by adding strands in proper stoichiometry from 70°C to room temperature over 24 hours. Structures were then electrophoresed through 15% non-denaturing PAGE ran at 150 V, at 4°C in 1X TBE. For each sample the correct bands, which incorporated the sense strand into the tile or lattice was extracted. 3-4 bands were placed into one tube and covered in 90 μl of 1X TAE / 12.5

mM $MgCl_2$ and allowed to incubate at 4°C for 24-48 hours.

7.3 Structural analysis of tile and lattice assembly

To verify the sense strand attachment to the tile, the sense strand for both GFP and PLK1 were labeled with Alexa 488 and Alexa 546, respectively at the 5' ends. We annealed individual tiles without sticky ends and lattices and tubular structures with fluorescently labeled sense strands. The sense strand targeted against GFP was labeled with Alexa 488 and the sense strand targeted against PLK1 was labeled with Alexa 546. We performed non-denaturing PAGE studies on these structures and tracked the labeled sense strand to determine its location in the tile and lattice Fig. 7.1. Interestingly, for the individual tiles we observed three prominent bands, which incorporated all of the tile strands Fig. 7.1 A, B. We hypothesize that the upper band has two sense strands attached, the next lower band has only one sense attached, and the third lowest band has no sense strands attached. For individual tile assembly with no sticky ends, there appears to be a small amount of tiles that polymerize at the top of the well, this could be due to the anti-sense strands interacting. For the lanes including annealed tiles, we observe a fairly prominent band at the bottom of the wells, which we expect is composed by tiles polymerized into lattices.

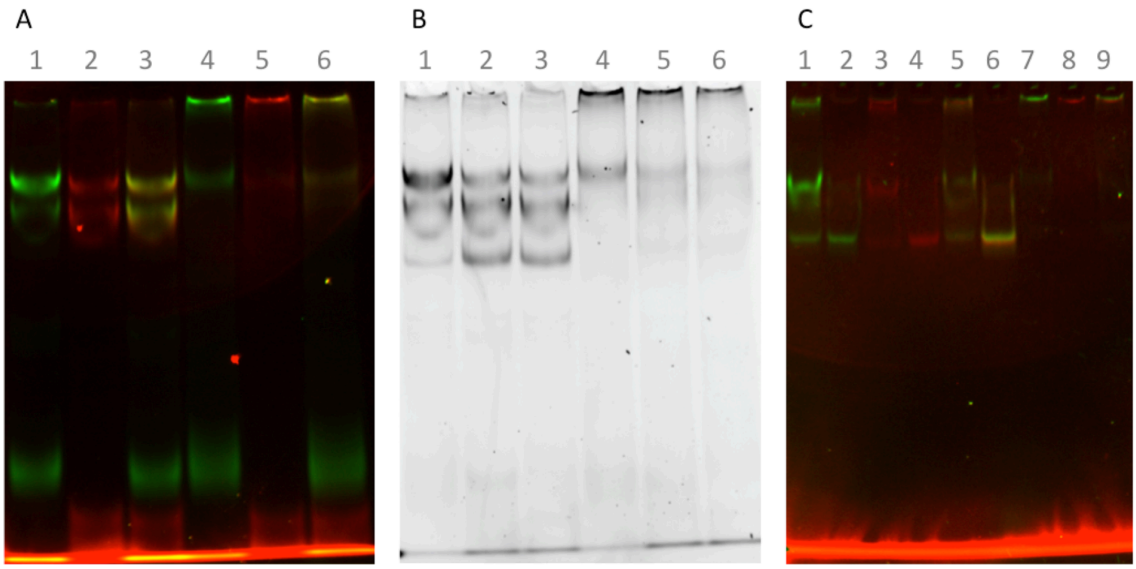

Figure 7.1: **10% non-denaturing PAGE analysis of tiles** A. Unpurified samples: (1) Tile with GFP (labeled) and PLK1 (unlabeled) senses. (2) Tile with GFP (unlabeled) and PLK1 (labeled) senses. (3) Tile with GFP (labeled) and PLK1 (labeled) senses (4) Lattice with GFP (labeled) and PLK1 (unlabeled) senses (5) Lattice with GFP (unlabeled) and PLK1 (labeled) senses (6) Lattice with GFP (labeled) and PLK1 (labeled) senses. B. SYBR gold stain of A. C. Purified samples: (1) Tile with GFP (labeled) and PLK1 (unlabeled) senses (upper band) (2) Tile with GFP (labeled) and PLK1 (unlabeled) senses (lower band) (3) Tile with GFP (unlabeled) and PLK1 (labeled) senses (upper band) (4) Tile with GFP (unlabeled) and PLK1 (labeled) senses (lower band) (5) Tile with GFP (labeled) and PLK1 (labeled) senses (upper band) (6) Tile with GFP (labeled) and PLK1 (labeled) senses (lower band) (7) Lattices with GFP (labeled) and PLK1 (unlabeled) senses (8) Lattices with GFP (unlabeled) and PLK1 (labeled) senses (9) Lattices with GFP (labeled) and PLK1 (labeled) senses.

7.4 Analysis of structural integrity with Lipofectamine®2000

To ensure that our structures remain intact during transfection, we performed experiments to determine the integrity of our RNA structures in the presence of Lipofectamine®2000 (L2K, Thermo Scientific #11668030) Fig. 7.2. Four samples were prepared: Sa+Sb (1:1), Sa+Sb (2:1), and Sa+Sb+Sc (2:1:2) were slowly annealed from 70°C to 22°C over 24 hr in 1X TAE and 12.5 mM $MgCl_2$ 10 μL of sample was added to 1 μL of L2K and allowed to incubate at room temperature for 30 minutes, then non-denaturing PAGE was performed with 10% gel at 150 V at 4°C in 1X TBE Fig. 7.1 B. Next 1 μL of Triton X100 (Sigma Aldrich #X100) was added to the sample to remove L2K, and allowed to incubate at room temperature for 30 minutes. Then, non- denaturing PAGE was performed with 10% gel at 150 V at 4°C in 1X TBE Fig. 7.2 C.

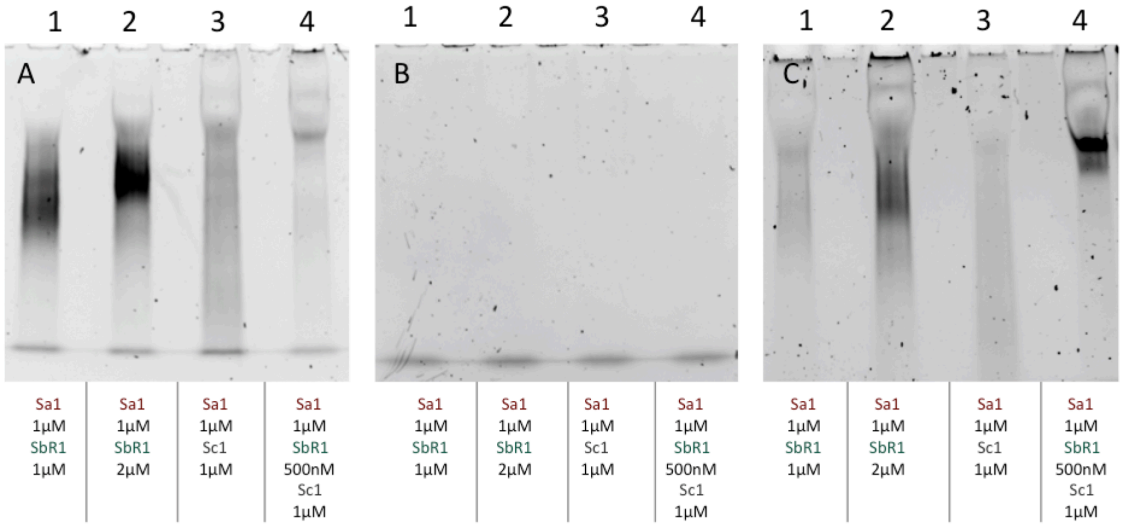

Figure 7.2: **10% non-denaturing PAGE** A. Assembled structures. B. Assembled structures associated with Lipofectamine 2000. C. Assembled structures associated with Lipofectamine 2000 and subsequently washed, with Trition X100.

Because L2K is positively charged, DNA associated with is unable to travel through the electrophoresis gel properly. However, when the detergent is introduced and L2K is removed, structures can migrate through the gel. Based on the consistent height of the band in lane 4 of the gels in Fig. 7.1 A, C, we conclude that minimum to no damage occurs to our structures when associated to L2K.

7.5 Dynamic Light Scattering (DLS) experiments

For DLS experiments, 100 μL of sample solutions (prepared in 0.2 μm filtered buffer) of assembled 1 μM tiles and lattices were used. The samples were measured at 25°C with a Nano-series Zetasizer ZS (Malvern Instruments Ltd) equipped with a red (633 nm) laser. Readings with polydispersity index (PdI) below 0.2 were used. Results are shown in Fig. 7.3.

7.6 Human blood serum stability assays

Freshly drawn human whole blood was spun down and serum was collected, aliquoted, frozen -80°C and later used for blood serum degradation experiments. Alexa-488 labeled tiles and lattices (1 μM final) were incubated with 10% (v/v) human blood serum at 37°C for various time points. Degradation time courses were quenched on dry ice and analyzed on non-denaturing PAGE, loaded in reverse order. The disappearance of fluorescent bands corresponding to the labeled tiles and lattices were quantified and analyzed. Results are shown in Fig. 7.4.

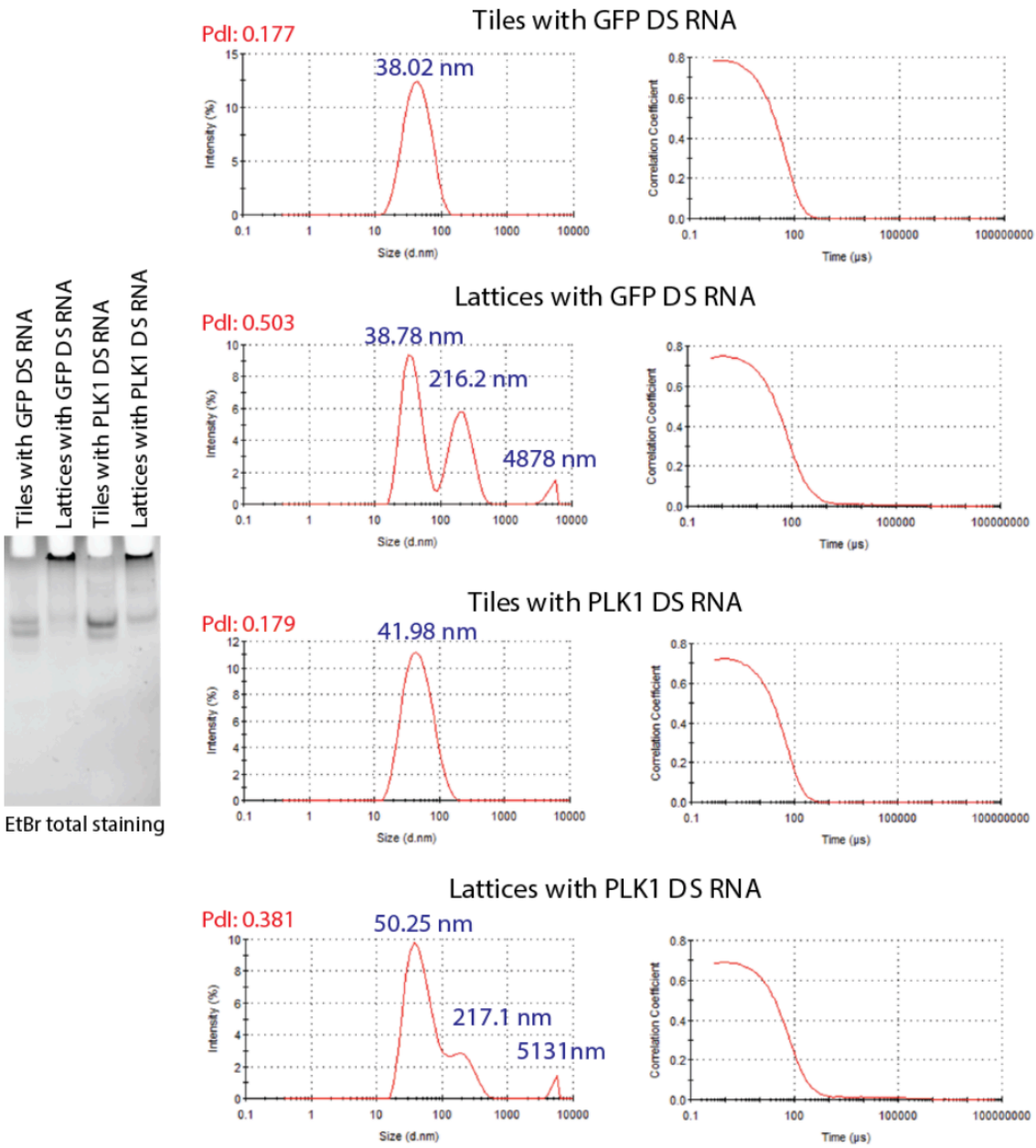

Figure 7.3: **Dynamic light scattering (DLS) experiment** The formation of RNA tiles and corresponding lattices functionalized with DS RNAs against GFP and PLK1 were confirmed by ethidium bromine total staining native-PAGE (37.5:1) and further analyzed by DLS. Size distribution by intensity and raw correlation data are shown for each sample. Note that the size distribution and the polydispersity index (PdI) increases dramatically for functionalized lattices.

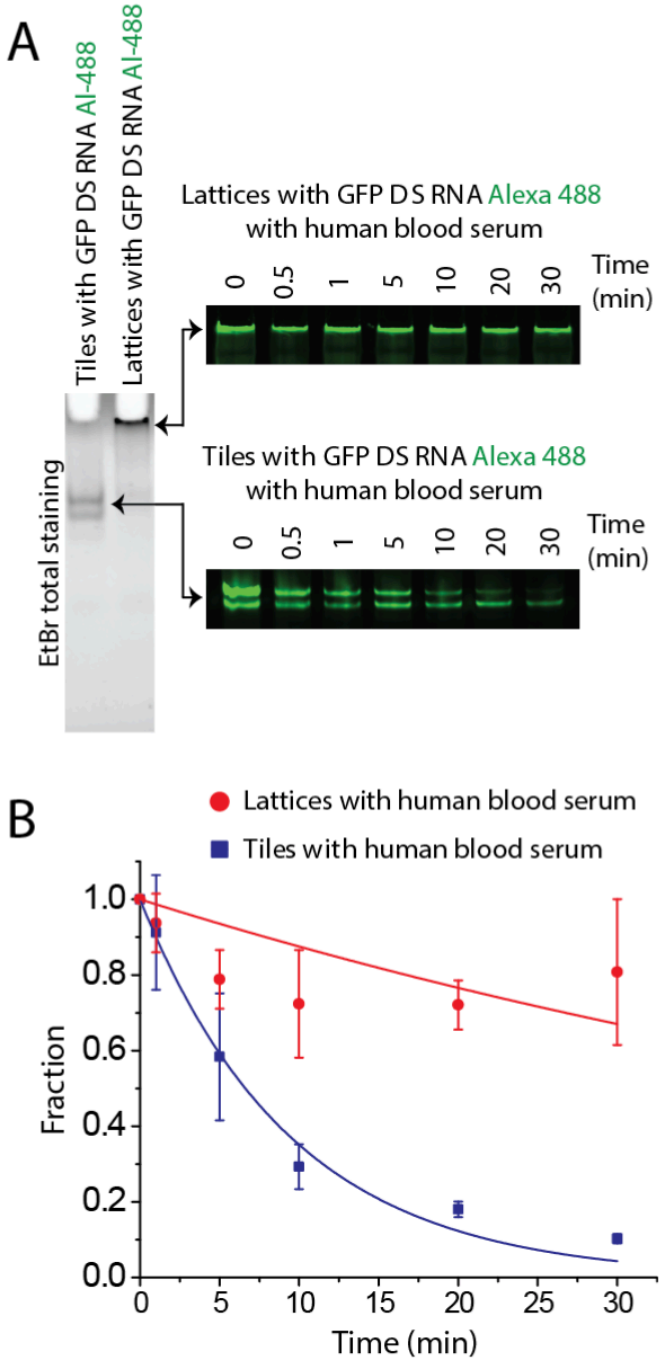

Figure 7.4: **Relative stabilities of functionalized tiles and lattices in human blood serum** A. Fluorescently labeled tiles and lattices treated with 10% (v/v) serum for different amounts of time were visualized on native-PAGE (37.5:1). B. Relative stabilities were estimated based on the quantification of the fluorescent bands. Error bars denote SD, N=3.

7.7 UV-melting experiments

Experiments were carried out at 260 nm on an Agilent 8453 spectrophotometer coupled with the Agilent 89090 Peltier Temperature Controller. The temperature was gradually increased and the absorbance was recorded every 1°C with 10 seconds equilibration time. The assembled RNA tiles and lattices (70 μL of 250 nM) were analyzed using Starna Cells sub-micro quartz fluorometer cell cuvette. The data was processed by a Boltzmann sigmoidal curve fit using Origin Pro 2016 Graphing and Analysis software. Results are shown in Fig. 7.5.

7.8 Transfection experiments

To evaluate the delivery of functionalized RNA tiles and lattices, the human breast cancer cell line MDA-MB-231 (with or without GFP) was grown in D-MEM medium (Gibco BRL) supplemented with 10% FBS and penicillin-streptomycin (pen-strep) in a 5% CO2 incubator. All transfections were performed using Lipofectamine®2000 (L2K) purchased from Invitrogen. 100X transfection solutions were pre-incubated at room temperature with L2K. Prior to each transfection, the cell media was replaced with OPTI-MEM with added RNA/L2K complexes at a final concentration of 1X. The cells were incubated for 4 hours followed by the media change (D-MEM, 10%FCS, 1% pen-strep). Results are shown in Fig. 7.6.

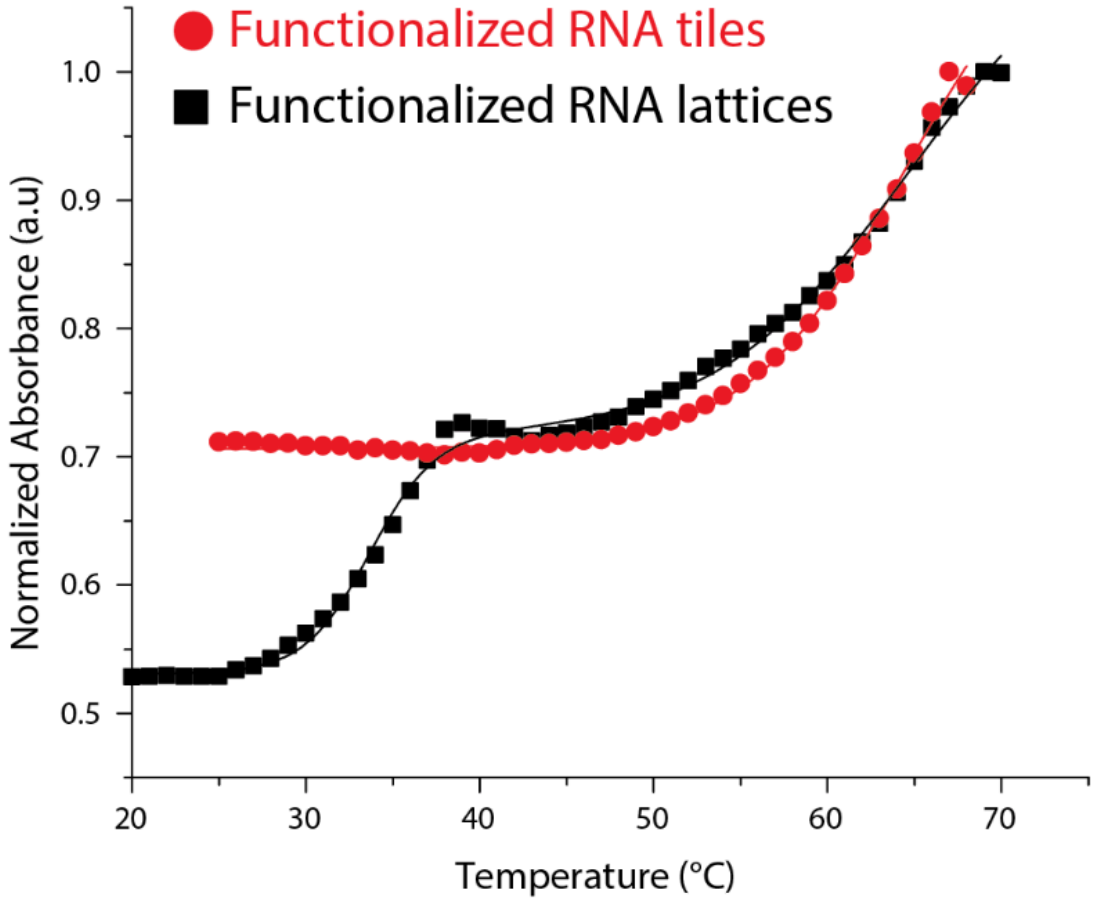

Figure 7.5: **UV melting of DS RNA functionalized tiles and lattices** Melting profiles measured by UV-melt for tiles and lattices functionalized with DS RNAs.

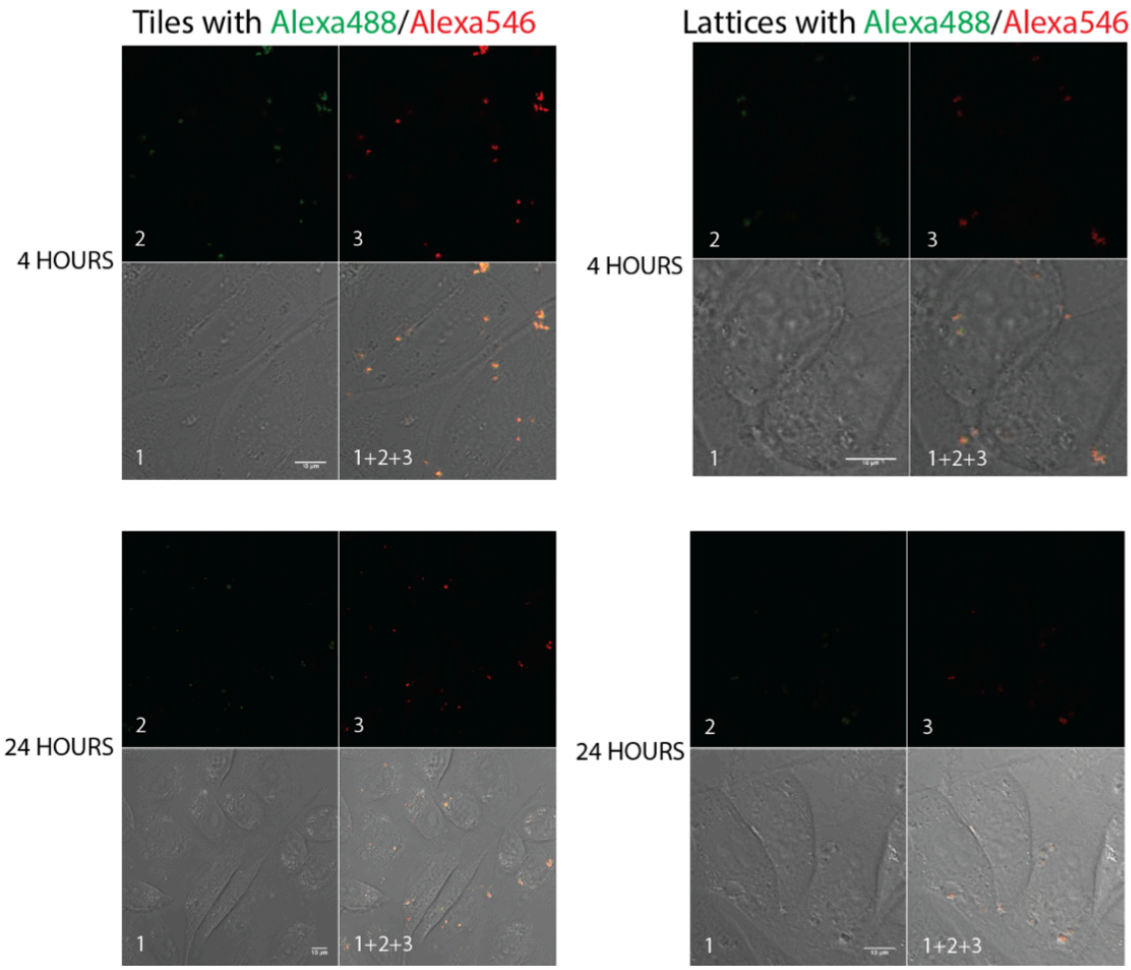

Figure 7.6: **Co-localization experiments for RNA tiles and lattices** Human breast cancer cells (MDA-MB-231) were transfected with gel purified tiles and lattices labeled with two different dyes (Alexa 488 and Alexa 546). Image numbers correspond to: differential interference contrast (DIC) images (1), Alexa 488 emission (2), and Alexa 546 emission (3). Images (1+2+3) are superposition of three different images.

7.9 Flow cytometry

For flow cytometry experiments, MDA-MB-231 cells (with or without GFP) grown in 24- well plates were transfected. The cells were lifted with cell dissociation buffer 24h later to assess their level of Alexa 488 (Alexa 546) fluorescence or 72h later to assess their GFP signal for uptake and silencing experiments respectively. The measurements were performed through fluorescence activated cell sorting on a FACSCalibur instrument (BD Biosciences, San Jose). At least 20,000 events were collected and analyzed with the CellQuest software to retrieve the geometric mean fluorescence intensity (gMFI) and the standard error of the mean.

7.10 Confocal microscopy of transfected cells

All experiments were performed using a LSM 710 confocal microscope (Carl Zeiss, Oberkochen) and a Plan-Apochromat 63x/1.40 Oil lens. MDA-MB-231 cells plated in glass bottom dishes (Ibidi, Madison) were transfected with fluorescently labeled nanoconstructs. Upon 4 hour incubation at 37°C, the cells were washed three times with PBS and fixed with 4% paraformaldehyde for 20 minutes at room temperature. For Alexa 488 imaging, the 488 nm line of an argon laser was used as excitation and the emission was collected between 493 and 557 nm. For Alexa 546 imaging, a DPSS 561 laser was used for excitation and emission was collected between 566 and 680 nm. For silencing experiments, MDA-MB-231 eGFP cells were used and visualized 72 hours post transfection upon fixation. For GFP imaging, the 488 nm line of an argon laser was used as excitation and the emission was collected between 499 and 644 nm.

7.11 Gene silencing experiments

To assess the function of siRNAs, we performed specific gene silencing experiments. GFP expressing breast cancer cells (MDA-MB-231/GFP) were transfected as mentioned in the Transfection experiments section with constructs carrying anti-GFP siRNAs and free DS RNAs. The GFP silencing was observed for 10 days with a faster fluorescence recovery for cells treated with functionalized lattices Fig. 7.7.

7.12 Viability assay

The viability of cells upon transfection was assessed through the CellTiter Blue assay (Promega, Madison) following manufacturers protocol. Briefly, upon addition of the CellTiter blue reagents to the cells at a 1 to 6 ratio in DMEM, the fluorescence of the resorufin forming compound was measured (560 ex/590 em) after 1-2 hour incubation at 37°C.

7.13 Effects of the presence of functional domains on assembly

In regards to structure formation we found that depending on the linked anti-sense and attached sense strand that the structures that form may either be lattices or tubular structures Fig. 7.8. We observed that when both Dicer substrate (DS) RNAs attached are targeted against GFP, tubular structures form. When both DS RNAs attached are targeted against PLK1, only lattices are observed. When DS RNAs attached are targeted against

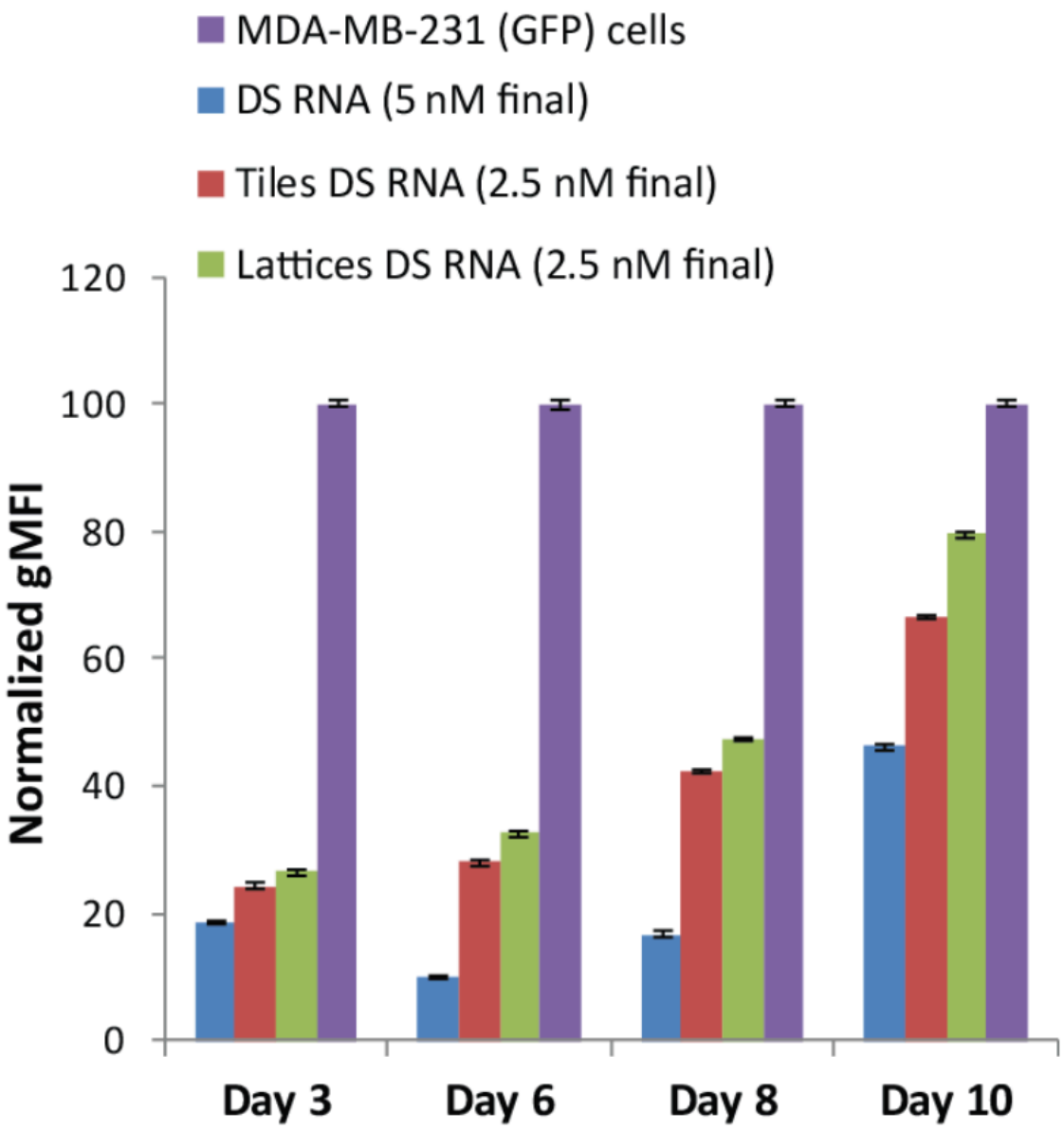

Figure 7.7: **Specific gene silencing triggered by functionalized RNA tiles and lattices** Silencing was observed for 10 days. Error bars denote S.E.M.

GFP and PLK1, lattices form. Tubular structures exhibit a left-handed chirality; however, the cause of this chirality is unknown.

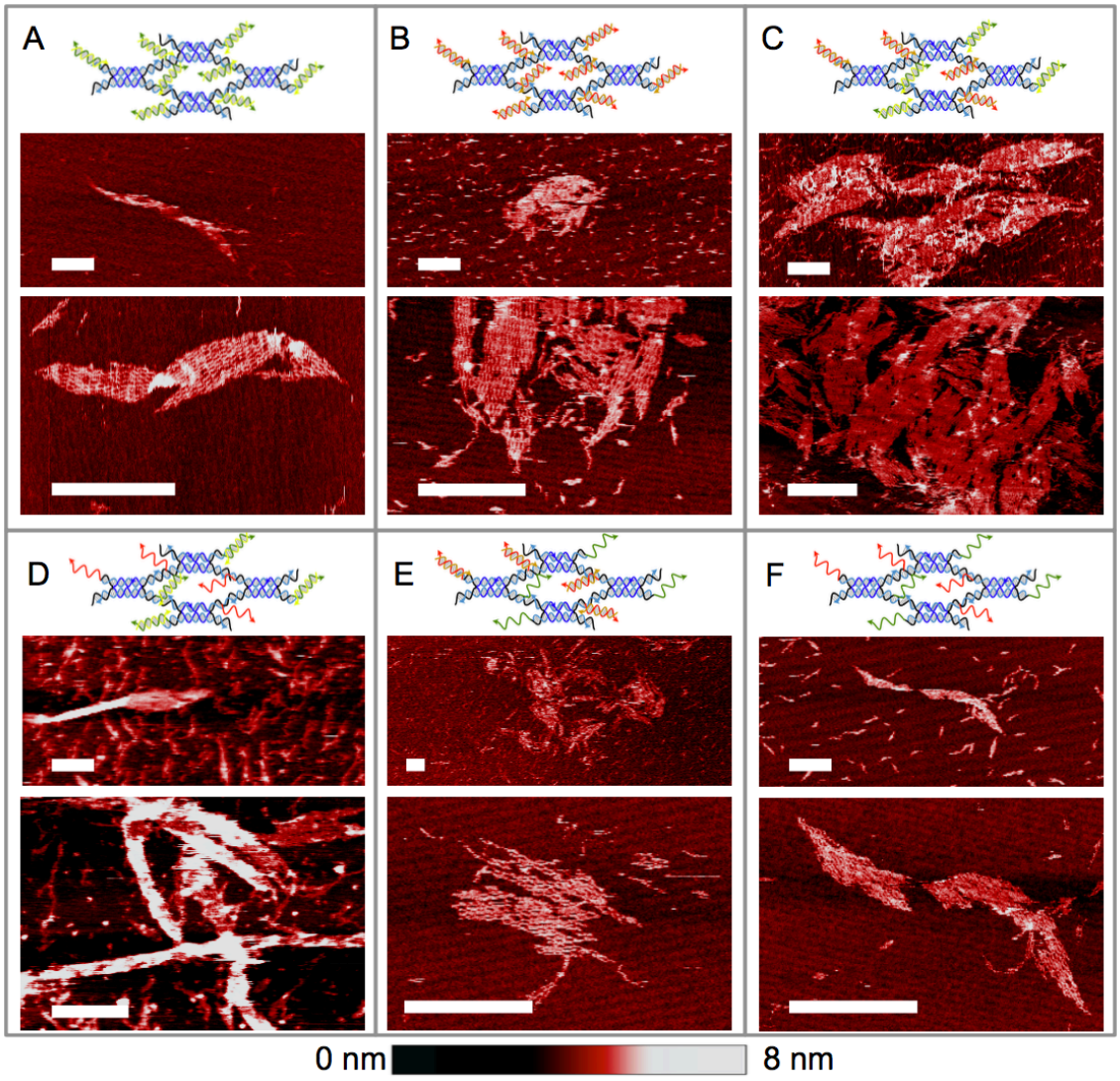

Figure 7.8: **Overview of AFM images of assembled structures** A. RNA DX tile with 2 DS RNAs targeted against green fluorescent protein (GFP). B. RNA DX tile with 2 DS RNAs targeted against PLK1. C. RNA DX tile with 2 DS RNAs targeted against GFP and PLK1. D. RNA DX tile with 1 DS RNA targeted against GFP and anti-sense PLK1. E. RNA DX tile with 1 DS RNA targeted against PLK1 and anti-sense GFP. F. RNA DX tile with GFP anti-sense and PLK1 anti-sense. Scale bar: 200 nm.

Chapter 8

A more robust RNA tile design for nanotube assembly

8.1 Sequences

RNA sequences for tile without siRNA were identified by converting to RNA the (44+6) tile design from . [65], as described by Stewart et al. [114]. PAGE purified DNA sequences were ordered from IDT DNA (Coralville, IA, USA). Genes include 3 base sealing domains (5' end of non-template strand) to prevent breathing at the 5' end of the promoter site. All genes include the T7 promoter sequence. The +1 to +6 promoter region (transcription start site) was modified relative to the generally recommended sequence (GGGAGA) [84], to avoid altering or constraining the sequence content of RNA tiles.

8.1.1 DNA templates

22-6 tile

S1 5'- TTC TAA TAC GAC TCA CTA TAG TCA GTG GAC AGC CGT TCT GGC AGC GTT GGA CGA AAC T -3' / 5'- AGT TTC GTC CAA CGC TGC CAG AAC GGC TGT CCA CTG ACT ATA GTG AGT CGT ATT AGA A -3'

S2 5'- TTC TAA TAC GAC TCA CTA TAG TCT GCG TAG AGC ACC ACT GAC AAG GTA -3' / 5'- TAC CTT GTC AGT GGT GCT CTA CGC AGA CTA TAG TGA GTC GTA TTA GAA -3'

S3 5'- TTC TAA TAC GAC TCA CTA TAG CCA GAA CGG CTG TGG GCT AAA CAG TAA CCG AAG CAC CAA CGC T -3' / 5'- AGC GTT GGT GCT TCG GTT ACT GTT TAG CCC ACA GCC GTT CTG GCT ATA GTG AGT CGT ATT AGA A -3'

S4 5'- TTC TAA TAC GAC TCA CTA TAG CAG ACA GTT TCG UGG TCA TCC TAC CTT -3' / 5'- AAG GTA GGA TGA CCA CGA AAC TGT CTG CTA TAG TGA GTC GTA TTA GAA -3'

S5 5'- TTC TAA TAC GAC TCA CTA TAG GAT GAC CTG CTT CGG TTA CTG TTT AGC CCT GCT CTA C -3' / 5'- GTA GAG CAG GGC TAA ACA GTA ACC GAA GCA GGT CAT CCT ATA GTG AGT CGT ATT AGA A -3'

23-7 tile

S1 5'- TTC TAA TAC GAC TCA CTA TAG TCA GTG GAC AGC CGT TCT GGC AGC GTT GGA CGA AAC T -3' / 5'- AGT TTC GTC CAA CGC TGC CAG AAC GGC TGT CCA CTG ACT ATA GTG AGT CGT ATT AGA A -3'

S2-2b 5'- TTC TAA TAC GAC TCA CTA TAG TCT GCC GTA GAG CAC CAC TGA CCA AGG TA -3' / 5'- TAC CTT GGT CAG TGG TGC TCT ACG GCA GAC TAT AGT GAG TCG TAT TAG AA -3'

S3 5'- TTC TAA TAC GAC TCA CTA TAG CCA GAA CGG CTG TGG GCT AAA CAG TAA CCG AAG CAC CAA CGC T -3' / 5'- AGC GTT GGT GCT TCG GTT ACT GTT TAG CCC ACA GCC GTT CTG GCT ATA GTG AGT CGT ATT AGA A -3'

S4-2b 5'- TTC TAA TAC GAC TCA CTA TAG GCA GAC AGT TTC GUG GTC ATC CTA CCT TG -3' / 5'- CAA GGT AGG ATG ACC ACG AAA CTG TCT GCC TAT AGT GAG TCG TAT TAG AA -3'

S5 5'- TTC TAA TAC GAC TCA CTA TAG GAT GAC CTG CTT CGG TTA CTG TTT AGC CCT GCT CTA C -3' / 5'- GTA GAG CAG GGC TAA ACA GTA ACC GAA GCA GGT CAT CCT ATA GTG AGT CGT ATT AGA A -3'

24-8 tile

S1 5'- TTC TAA TAC GAC TCA CTA TAG TCA GTG GAC AGC CGT TCT GGC AGC GTT GGA CGA AAC T -3' / 5'- AGT TTC GTC CAA CGC TGC CAG AAC GGC TGT CCA CTG ACT ATA GTG AGT CGT ATT AGA A -3'

S2-4b TTC TAA TAC GAC TCA CTA TAG GTC TGC CGT AGA GCA CCA CTG ACA CAA GGT A -3' / 5'- TAC CTT GTG TCA GTG GTG CTC TAC GGC AGA CCT ATA GTG AGT CGT ATT AGA A -3'

S3 5'- TTC TAA TAC GAC TCA CTA TAG CCA GAA CGG CTG TGG GCT AAA CAG TAA CCG AAG CAC CAA CGC T -3' / 5'- AGC GTT GGT GCT TCG GTT ACT GTT TAG CCC ACA GCC GTT CTG GCT ATA GTG AGT CGT ATT AGA A -3'

S4-4b 5'- TTC TAA TAC GAC TCA CTA TAG GCA GAC CAG TTT CGT GGT CAT CCU ACC TTG T -3' / 5'- ACA AGG TAG GAT GAC CAC GAA ACT GGT CTG CCT ATA GTG AGT CGT ATT AGA A -3'

S5 5'- TTC TAA TAC GAC TCA CTA TAG GAT GAC CTG CTT CGG TTA CTG TTT AGC CCT GCT CTA C -3' / 5'- GTA GAG CAG GGC TAA ACA GTA ACC GAA GCA GGT CAT CCT ATA GTG AGT CGT ATT AGA A -3'

25-9 tile

S1 5'- TTC TAA TAC GAC TCA CTA TAG TCA GTG GAC AGC CGT TCT GGC AGC GTT GGA CGA AAC T -3' / 5'- AGT TTC GTC CAA CGC TGC CAG AAC GGC TGT CCA CTG ACT ATA GTG AGT CGT ATT AGA A -3'

S2-6b 5'- TTC TAA TAC GAC TCA CTA TAG TCT GCA TCG TAG AGC ACC ACT GAC AGG AAG GTA -3' / 5'- TAC CTT CCT GTC AGT GGT GCT CTA CGA TGC AGA CTA TAG TGA GTC GTA TTA GAA -3'

S3 5'- TTC TAA TAC GAC TCA CTA TAG CCA GAA CGG CTG TGG GCT AAA CAG TAA CCG AAG CAC CAA CGC T -3' / 5'- AGC GTT GGT GCT TCG GTT ACT GTT TAG CCC ACA GCC GTT CTG GCT ATA GTG AGT CGT ATT AGA A -3'

S4-6b 5'- TTC TAA TAC GAC TCA CTA TAG ATG CAG ACA GTT TCG UGG TCA TCC TAC CTT CCT -3' / 5'- AGG AAG GTA GGA TGA CCA CGA AAC TGT CTG CAT CTA TAG TGA GTC GTA TTA GAA -3'

S5 5'- TTC TAA TAC GAC TCA CTA TAG GAT GAC CTG CTT CGG TTA CTG TTT AGC CCT GCT CTA C -3' / 5'- GTA GAG CAG GGC TAA ACA GTA ACC GAA GCA GGT CAT CCT ATA GTG AGT CGT ATT AGA A -3'

26-10 tile

S1 5'- TTC TAA TAC GAC TCA CTA TAG TCA GTG GAC AGC CGT TCT GGC AGC GTT GGA CGA AAC T -3' / 5'- AGT TTC GTC CAA CGC TGC CAG AAC

GGC TGT CCA CTG ACT ATA GTG AGT CGT ATT AGA A -3'

S2-8b 5'- TTC TAA TAC GAC TCA CTA TAG TCT GCT ATC GTA GAG CAC CAC TGA CAA GGA AGG TA -3' / 5'- TAC CTT CCT TGT CAG TGG TGC TCT ACG ATA GCA GAC TAT AGT GAG TCG TAT TAG AA -3'

S3 5'- TTC TAA TAC GAC TCA CTA TAG CCA GAA CGG CTG TGG GCT AAA CAG TAA CCG AAG CAC CAA CGC T -3' / 5'- AGC GTT GGT GCT TCG GTT ACT GTT TAG CCC ACA GCC GTT CTG GCT ATA GTG AGT CGT ATT AGA A -3'

S4-8b 5'- TTC TAA TAC GAC TCA CTA TAG ATA GCA GAC AGT TTC GTG GTC ATC CTA CCT TCC TT -3' / 5'- AAG GAA GGT AGG ATG ACC ACG AAA CTG TCT GCT ATC TAT AGT GAG TCG TAT TAG AA -3'

S5 5'- TTC TAA TAC GAC TCA CTA TAG GAT GAC CTG CTT CGG TTA CTG TTT AGC CCT GCT CTA C -3' / 5'- GTA GAG CAG GGC TAA ACA GTA ACC GAA GCA GGT CAT CCT ATA GTG AGT CGT ATT AGA A -3'

23-7 two tile system

S1 5'- TTC TAA TAC GAC TCA CTA TAG TCA GTG GAC AGC CGT TCT GGC AGC GTT GGA CGA AAC T -3' / 5'- AGT TTC GTC CAA CGC TGC CAG AAC GGC TGT CCA CTG ACT ATA GTG AGT CGT ATT AGA A -3'

S2-2b-T1 5'- TTC TAA TAC GAC TCA CTA TAG AAC GAC GTA GAG CAC CAC TGA CCA AGG TA -3' / 5'- TAC CTT GGT CAG TGG TGC TCT ACG TCG TTC TAT AGT GAG TCG TAT TAG AA -3'

S2-2b-T2 5'- TTC TAA TAC GAC TCA CTA TAG TCT GCC GTA GAG CAC CAC TGA CTG AAT GA -3' / 5'- TCA TTC AGT CAG TGG TGC TCT ACG GCA GAC

TAT AGT GAG TCG TAT TAG AA -3’

S3 5’- TTC TAA TAC GAC TCA CTA TAG CCA GAA CGG CTG TGG GCT AAA CAG TAA CCG AAG CAC CAA CGC T -3’ / 5’- AGC GTT GGT GCT TCG GTT ACT GTT TAG CCC ACA GCC GTT CTG GCT ATA GTG AGT CGT ATT AGA A -3’

S4-2b-T1 5’- TTC TAA TAC GAC TCA CTA TAG GCA GAC AGT TTC GTG GTC ATC CTC ATT CA -3’ / 5’- TGA ATG AGG ATG ACC ACG AAA CTG TCT GCC TAT AGT GAG TCG TAT TAG AA -3’

S4-2b-T2 5’- TTC TAA TAC GAC TCA CTA TAG TCG TTC AGT TTC GTG GTC ATC CTA CCT TG -3’ / 5’- CAA GGT AGG ATG ACC ACG AAA CTG AAC GAC TAT AGT GAG TCG TAT TAG AA -3’

S5 5’- TTC TAA TAC GAC TCA CTA TAG GAT GAC CTG CTT CGG TTA CTG TTT AGC CCT GCT CTA C -3’ / 5’- GTA GAG CAG GGC TAA ACA GTA ACC GAA GCA GGT CAT CCT ATA GTG AGT CGT ATT AGA A -3’

23-7 toeholded tile

S1 5’- TTC TAA TAC GAC TCA CTA TAG TCA GTG GAC AGC CGT TCT GGC AGC GTT GGA CGA AAC T -3’ / 5’- AGT TTC GTC CAA CGC TGC CAG AAC GGC TGT CCA CTG ACT ATA GTG AGT CGT ATT AGA A -3’

S2-2b 5’- TTC TAA TAC GAC TCA CTA TAG TCT GCC GTA GAG CAC CAC TGA CCA AGG TA -3’ / 5’- TAC CTT GGT CAG TGG TGC TCT ACG GCA GAC TAT AGT GAG TCG TAT TAG AA -3’

S3 5’- TTC TAA TAC GAC TCA CTA TAG CCA GAA CGG CTG TGG GCT AAA CAG TAA CCG AAG CAC CAA CGC T -3’ / 5’- AGC GTT GGT GCT TCG GTT ACT

GTT TAG CCC ACA GCC GTT CTG GCT ATA GTG AGT CGT ATT AGA A -3'

S4-2b-TH 5'- TTC TAA TAC GAC TCA CTA TAG AAT AGG CAG ACA GTT TCG TGG TCA TCC TAC CTT G -3' / 5'- CAA GGT AGG ATG ACC ACG AAA CTG TCT GCC TAT TCT ATA GTG AGT CGT ATT AGA A -3'

S5 5'- TTC TAA TAC GAC TCA CTA TAG GAT GAC CTG CTT CGG TTA CTG TTT AGC CCT GCT CTA C -3' / 5'- GTA GAG CAG GGC TAA ACA GTA ACC GAA GCA GGT CAT CCT ATA GTG AGT CGT ATT AGA A -3'

8.1.2 RNA sequences

22-6 tile

S1 5'- GUCAGUGG ACAGCCGUUCUGGCAGCGUUGG ACGAAACU -3'

S2 5'- GUCUGCGUAGAGCACCACUGACAAGGUA -3'

S3 5'- GCCAGAACGGCUGU GGGCUAAACAGUAACCGAAGCA CCAACGCU -3'

S4 5'- GCAGACAGUUUCGUGGUCAUCCUACCUU -3'

S5 5'- GGAUGACC UGCUUCGGUUACUGUUUAGCCC UGCUCUAC -3'

23-7 tile

S1 5'- GUCAGUGG ACAGCCGUUCUGGCAGCGUUGG ACGAAACU -3'

S2-2b 5'- GUCUGCC GUAGAGCACCACUGAC CAAGGUA -3'

S3 5'- GCCAGAACGGCUGU GGGCUAAACAGUAACCGAAGCA CCAACGCU -3'

S4-2b 5'- GGCAGAC AGUUUCGUGGUCAUCC UACCUUG -3'

S5 5'- GGAUGACC UGCUUCGGUUACUGUUUAGCCC UGCUCUAC -3'

24-8 tile

S1 5'- GUCAGUGG ACAGCCGUUCUGGCAGCGUUGG ACGAAACU -3'

S2-4b 5'- GGUCUGCC GUAGAGCACCACUGAC ACAAGGUA -3'

S3 5'- GCCAGAACGGCUGU GGGCUAAACAGUAACCGAAGCA CCAACGCU -3'

S4-4b 5'- GGCAGACC AGUUUCGUGGUCAUCC UACCUUGU -3'

S5 5'- GGAUGACC UGCUUCGGUUACUGUUUAGCCC UGCUCUAC -3'

25-9 tile

S1 5'- GUCAGUGG ACAGCCGUUCUGGCAGCGUUGG ACGAAACU -3'

S2-6b 5'- GUCUGCAUC GUAGAGCACCACUG ACAGGAAGGUA -3'

S3 5'- GCCAGAACGGCUGU GGGCUAAACAGUAACCGAAGCA CCAACGCU -3'

S4-6b 5'- GAUGCAGAC AGUUUCGUGGUCAUCC UACCUUCCU -3'

S5 5'- GGAUGACC UGCUUCGGUUACUGUUUAGCCC UGCUCUAC -3'

26-10 tile

S1 5'- GUCAGUGG ACAGCCGUUCUGGCAGCGUUGG ACGAAACU -3'

S2-8b 5'- GUCUGCUAUC GUAGAGCACCACUGAC AAGGAAGGUA -3'

S3 5'- GCCAGAACGGCUGU GGGCUAAACAGUAACCGAAGCA CCAACGCU -3'

S4-8b 5'- GAUAGCAGAC AGUUUCGUGGUCAUCC UACCUUCCUU -3'

S5 5'- GGAUGACC UGCUUCGGUUACUGUUUAGCCC UGCUCUAC -3'

23-7 two tile system

S1 5'- GUCAGUGG ACAGCCGUUCUGGCAGCGUUGG ACGAAACU -3'

S2-2b-T1 5'- GAACGAC GUAGAGCACCACUGAC CAAGGUA -3'

S2-2b-T2 5'- GUCUGCC GUAGAGCACCACUGAC UGAAUGA -3'

S3 5'- GCCAGAACGGCUGU GGGCUAAACAGUAACCGAAGCA CCAACGCU -3'

S4-2b-T1 5'- GGCAGAC AGUUUCGUGGUCAUCC UCAUUCA -3'

S4-2b-T2 5'- GUCGUUC AGUUUCGUGGUCAUCC UACCUUG -3'

S5 5'- GGAUGACC UGCUUCGGUUACUGUUUAGCCC UGCUCUAC -3'

23-7 toeholded tile

S1 5'- GUCAGUGG ACAGCCGUUCUGGCAGCGUUGG ACGAAACU -3'

S2-2b 5'- GUCUGCC GUAGAGCACCACUGAC CAAGGUA -3'

S3 5'- GCCAGAACGGCUGU GGGCUAAACAGUAACCGAAGCA CCAACGCU -3'

S4-2b-TH 5'- GAAUA GGCAGAC AGUUUCGUGGUCAUCC UACCUUG -3'

S5 5'- GGAUGACC UGCUUCGGUUACUGUUUAGCCC UGCUCUAC -3'

8.2 Methods

8.2.1 Atomic force microscopy

AFM images were obtained in tapping mode under buffer using a Digital Instruments Multimode AFM with a Nanoscope®III controller. Either a Bruker SNL-10 silicon tip on a nitride lever with a spring constant of ≈ 0.24 N/m and a drive frequency of ≈9-10 kHz or an Olympus BL-AC40TS-C2 with a spring constant of ≈ 0.09 N/m and a drive frequency of ≈27-28 kHz were used for imaging. AFM buffer consisted of the same buffer used for annealing unless otherwise noted.

Fluorescence Microscopy

Images were obtained with a NIKON TI-E inverted fluorescence microscope. Cy3 filter was used to image all tiles with Cy3 labeled S3 strand 60x oil immersion objective was used to collect all images, with a standard exposure time of 600 ms.

8.2.2 Denaturing polyacrylamide gel electrophoresis

Pre-mix was prepared by adding 42 g of urea to 25 mL of nanopure water (for a final volume of 100 mL), the mixture was then heated until the urea completely dissolved. This mixture was allowed to cool to room temperature, then a 40% (v/v) 19:1 acrylamide/bis-acrylamide solution was added in the appropriate volume for the desired percentage. The pre-mix was added in appropriate ratios with TBE and nanopure water, ammonium persulfate (APS), and tetramethylethylenediamine (TEMED) to start polymerization. Gels were cast in 1010 cm, 1 mm thick disposable mini gel cassettes (Thermo Scientific, #NC2010) and allowed to polymerize for at least 2 hours before electrophoresis. Gels were run at room temperature at 100 V in 1X TBE unless otherwise noted. After electrophoresis the gels were stained in SYBR®Gold Nucleic Acid Gel Stain or ethidium bromide and then imaged using the Bio-Rad ChemiDoc MP system.

8.2.3 Non-denaturing polyacrylamide gel electrophoresis

40% solution of 19:1 acrylamide/bis-acrylamide, TAE, $MgCl_2$, APS, and TEMED were added together at appropriate concentrations for the desired polyacrylamide percentage, then cast in 1010 cm, 1 mm thick disposable mini gel cassettes (Thermo Scientific, #NC2010) and allowed to polymerize for at least 2 hours before electrophoresis. Gels were run at 4°C at 150 V in 1X TBE buffer. After electrophoresis gels were stained in SYBR®Gold Nucleic Acid Gel Stain or ethidium bromide and then imaged using the Bio-Rad ChemiDoc MP system.

8.2.4 RNA extraction

Using the AmpliScribe-T7-Flash Transcription Kit the following components were mixed at room temperature: RNase-free water, 1-1.5 μg gene, AmpliScribe T7-Flash 1X Reaction Buffer (Epicentre, #ASF3507), 9 mM NTPs, 40 U/μL RiboGuard RNase Inhibitor (Epicentre, #RG90925), and 1 unit of AmpliScribe T7-Flash Enzyme Solution (Epicentre, ASF3507). This mix was incubated at 37°C for 4 hours. After incubation, 20 μL of loading dye was added to the 20 μL transcription solution, and 8 μL of the transcription/dye mix was added to each of the middle 5 lanes of the gel. The gel was run at 100 V at room temperature in 1X TBE.

After electrophoresis the gel was stained in 80 mL 1X TBE and 1 μL SYBR®Gold Nucleic Acid Gel Stain (Thermo Scientific, # S-11494) for 20-30 minutes. The gel was then placed on a TLC silica gel 60 W F254S aluminum sheet (EMD Millipore, #1055590001) covered in plastic wrap. The gel was illuminated with UV light and the desired RNA band was cut out and chopped into equal amounts and placed into 0.5 mL DNA Lobind tubes (Eppendorf, #022431005), then 200 μL of 0.3 M sodium acetate at pH 5.3 was added to the Lobind tubes. The samples were then incubated at 42°C for 20 hours. After incubation, the sodium acetate was removed and placed into 1.7 mL RNase/DNase free tubes. The old Lobind tubes were rinsed with 100 μl of 0.3 M sodium acetate pH 5.3, which was added to the new samples. Then 1 mL of freezer cold 100% ETOH and 1 μL of glycogen were added into each tube and the sample was incubated at -20°C for 20 hours.

Next, the samples were spun at 13,500 rpm at 4°C for 15 minutes. The white precipitate pellet (RNA) at the bottom of the tube was located and the supernatant was

carefully pipetted out of the tubes avoiding removal of the pellet. Then, 500 μl of 70% freezer cold ETOH was added to the tubes and spun at 13,500 rpm at 4°C for 5 minutes. The supernatant was carefully decanted again with a pipette. This washing procedure was repeated a third time. After the last wash, as much supernatant was removed as possible, then the samples were opened and placed in the vacuum concentrator and allowed to spin at room temperature for 15 minutes. The samples were then re-suspended in 10-15 μL of Ambion nuclease free water (Ambion, #AM9932).

8.3 Formation of DNA/RNA hybrid structures

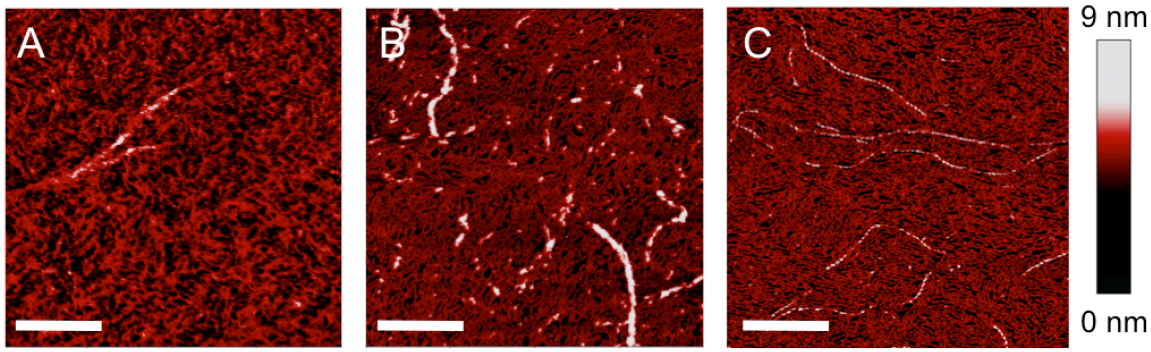

Figure 8.1: **AFM of DNA/RNA hybrid structures** A. 24-8 tile with S2 as DNA B. 24-8 tile with S4 as DNA C. 24-8 tile with S2 and S4 as DNA scale bar 250 nm

8.4 Characterization structures using non-denaturing PAGE

Interestingly, the tile designs can assemble as a hybrid structure. Using the 24-8 tile variant, we replaced S2 and S4 with the DNA variants (Fig. 8.1). We found that tubular assemblies form whether one or both of the sticky ends are DNA. In terms of yield, when

S4 is replaced with DNA and S2 is RNA or when both S2 and S4 are replaced with DNA, the yield of tubular formation is more robust rather than when S2 is replaces with DNA and S4 is RNA. When the sticky ends are DNA there is a considerable difference in tube length, these hybrid structures are too small to be seen via fluorescence microscopy (¡ 1000 nm in length).

In theory, it makes sense that tubular structures form when only one sticky end is DNA and the other complementary sticky end is RNA, as the A-form helicity is maintained throughout the hybrid tile as a it would be in a pure RNA tile. However, when both sticky end strands are DNA the helical geometry at the sticky ends should be B-form as this is a DNA-DNA interaction and the rest of the tile should be A-form as this is either RNA-RNA interaction or RNA-DNA interaction. It is possible that the sticky ends are adopting geometry between A-form and B-form, which would also account for tubes that are shorter in length in comparison to pure RNA structures.

We used non-denaturing PAGE to characterize individual strand secondary structure as well as full structure assembly (in supplement). For tile variants 22-5, 25-9, 26-10 the strands with the sticky ends tend to form secondary structures visible by the excess of bands, where as for tile variants 23-7 and 24-8 the strands with the sticky ends run as a single clean band. For the assembly of the complete tile as it seems that nothing large forms with the 22-5 tile variant as there is nothing present in the well of the gel and there is a migration of a smeared band. It appears for 23-7 and 24-8 tile variants something larger is in fact forming as we observe a prominent band in the well for both tile variants. For 23-7 we also notice the presence of lower bands, which we believe may be properly folded monomer

tiles and misfolded tiles. We believe the higher band is the properly folded monomer tile.

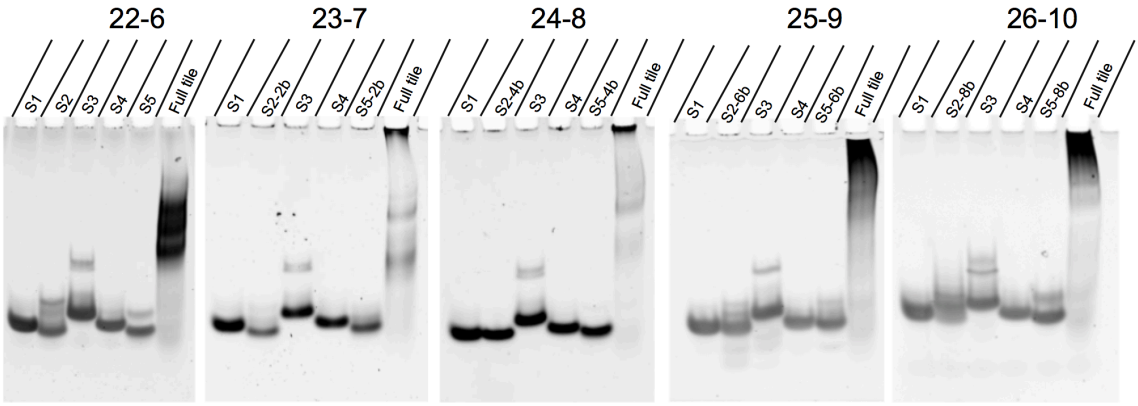

Figure 8.2: **10 % non-denaturing PAGE** characterization of tile variants: 22-6, 23-7, 24-8, 25-9, and 26-10

8.5 Nanotube nucleation requires high tile concentration

For all of the previous studies tiles were annealed at 1 μM concentration. To investigate the correlation between nucleation and the tile concentration the 23-7 and 24-8 tile variants were annealed at different tile concentrations of 1000 nM, 500 nM, 250 nM, and 100 nM (Fig. 8.3). Tube formation was observed at tile concentrations from 1000 nM - 250 nM. This range is much higher in comparison to DNA DX tile based tubes as well as previous RNA tile based tubes, where we were able to observe the formation of tubes at 50 nM annealed tile concentration [115]. Obviously, there are distinct geometrical differences between the DNA DAE tiles and the RNA DAE tiles, in the case of comparing the RNA tiles, certain tile features such as symmetry, center strand nick position, and inter-tile crossover length may play a role in determining minimum tile concentration required for nucleation.

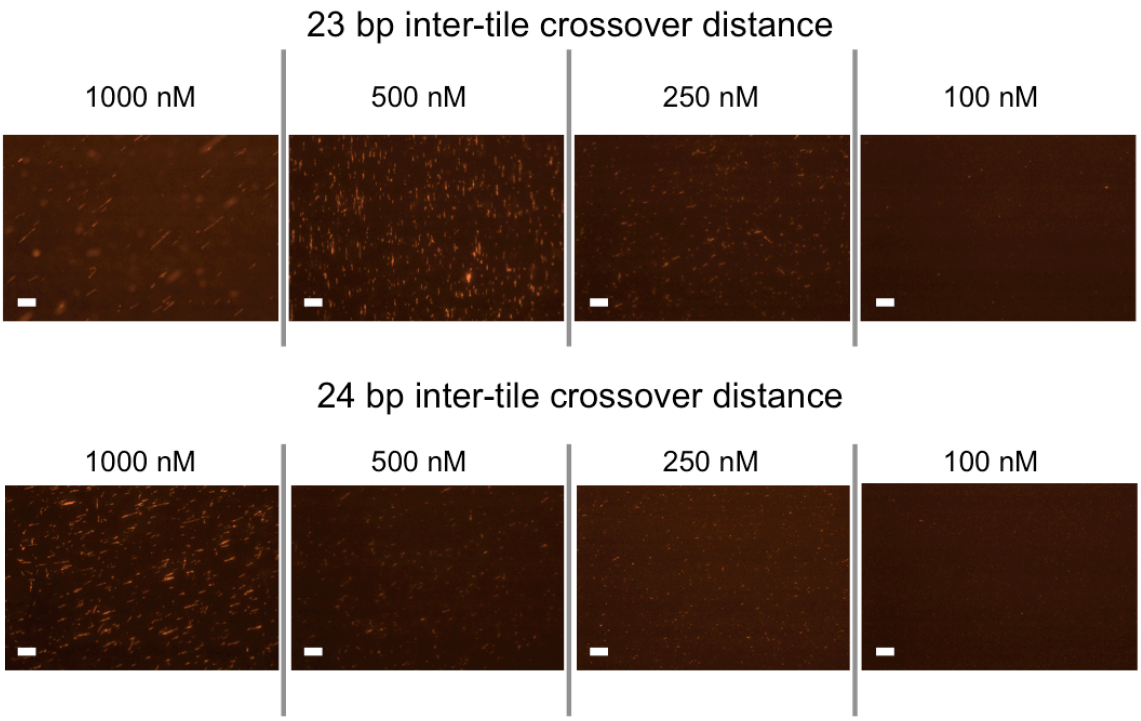

Figure 8.3: **Fluorescence microscopy of varying anneal concentrations** scale bar: 10 μm

AFM was used as a second check to validate assemblies at these concentrations Fig. 8.4. As the annealed tile concentration decreases we also notice a qualitative decrease in the lengths of the tubes that form.

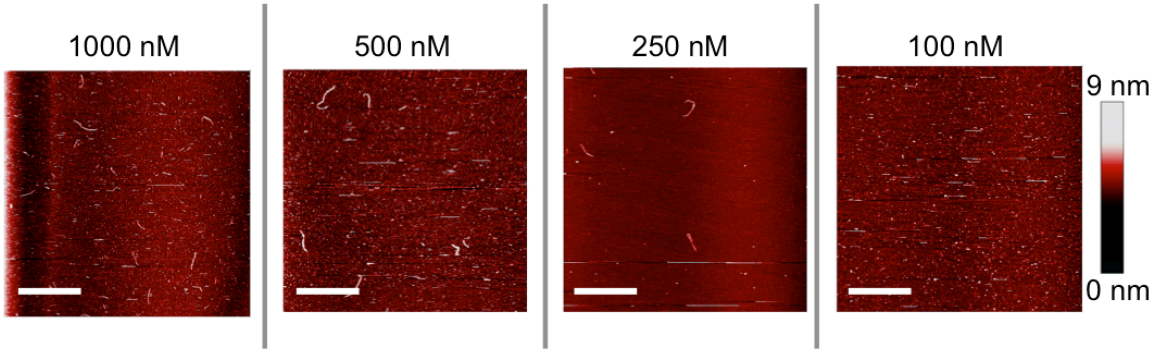

Figure 8.4: **AFM of varying anneal concentrations for the 23-7 tile variant** scale bar: 5μm

8.6 Formation of nanotubes is influenced by sticky end length

Using the 24-8 tile variant we modified the tile to shorten the sticky end length from 8 bases to 5 bases to observe the effect on assembly. We increased the length of the S1 and S5 strands by 6 bases each and tested two different sequence variations for the S2 and S4 strands (24-5v1 and 24-5v2) as well as testing the effect on assembly whether the S2 and S4 strands were RNA or DNA. We visualized the assemblies using AFM (Fig. 8.5). For the 24-5v1 pure RNA tile variant we observe no formation of tubular structures, rather flat lattices in comparison to the 24-5v2 pure RNA tile variant where we observe the assembly of neither tubular structures nor flat lattices. For the 24-5v1 hybrid DNA/RNA tile variant, where S2 and S4 are DNA strands, we observe long and thin lattice formation, and no

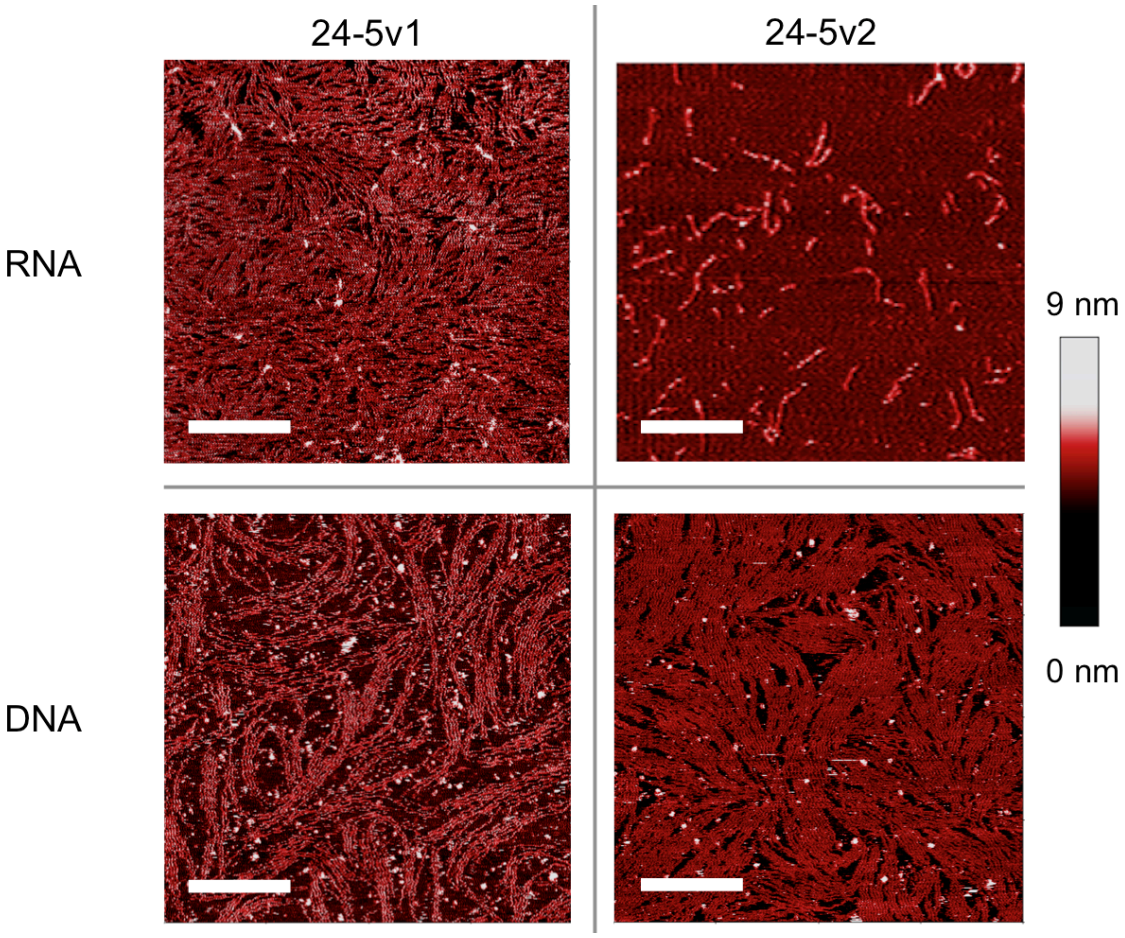

Figure 8.5: **AFM of of 24-5v1 and 24-5v2 tile variants** assembly of structures with either DNA or RNA sticky end strands scale bar: 250 nm

formation of tubes. The 24-5v2 hybrid DNA/RNA tile variant yields wide flat lattices and no formation of tubes.We believe that reducing the sticky end length of the 24-8 tile variant effects the geometry of individual tiles. This effect on geometry creates a steric hindrance that effects individual tiles as well as causing strain on the inter-tile interactions preventing tubular assemblies.